Chapter 1.

INTRODUCTION TO PHOTOVOLTAIC SOLAR ENERGY

Miro Zeman
Delft University of Technology

1.1 Introduction to energy consumption and production

Any change that takes place in the universe is accompanied by a change in a quantity that we name ***energy***. We do not know what energy exactly is, we use this term to describe a capacity of a physical or biological system for movement or change. Energy comes in many forms, such as electrical energy, chemical energy, or mechanical energy, and it can be used to realize many forms of change, such as movement, heating, or chemical change. Any activity, and human activity as well, requires energy. Human beings need it to move their bodies, to cook, to heat and light houses, or to drive vehicles. Human being is a greedy consumer of energy. An active young man needs about 2500 kcal (2.9 kWh) per day to fulfil his daily energy requirements. This means the energy of about 1060 kWh per year. The present global energy consumption is around 19 000 kWh per inhabitant per year. It means that on average a man consumes about 19 times more energy than is needed for his survival and satisfactory health.

The mankind has witnessed an enormous increase in energy consumption during last 100 years. While in 1890 the energy use per inhabitant per year was around 5800 kWh it reached 20200 kWh in 1970. Since 1970 the energy use has dropped to the present level of 19000 kWh per inhabitant per year. The increase in energy use in the 20th century can be

related to an evolution process that has started about five centuries ago. The underlying motivation of this process was formulated during the Enlightenment period in the 18th century as the philosophy of human progress. The aim of the process was an examination of the surrounding world and its adaptation to the needs of people whose life would become more secure and comfortable. This process was accompanied by growing industrialization and mass production, which were demanding more and more energy. At the end of the 19th century coal was the main source of energy. In this period electricity was introduced in the industrialized countries as a new and elegant form of energy. This form of energy was quickly applied on a large scale. The widespread growth of electricity use led to construction of hydroelectric plants and hydropower became an important source of energy in the first half of the 20th century.

In the period after the World War II much effort was put into the reconstruction of the society. The emphasis was directed on the growth and efficiency of the mass production. New technologies and new materials, such as plastic, were applied in the production. The energy demand was tremendously growing in this period. Oil and gas started to play an important role as energy sources in the second half of the 20th century. Coal, oil, and gas form today dominant sources of energy. These three energy sources, also known as ***fossil fuels***, are called the ***traditional energy sources***. In this period nuclear energy was introduced as a new source of energy. Increasing and more efficient mass production resulted in the low price of many household products. The consumption of the products grew enormously and therefore it is not surprising that we characterise today society as a consumption society.

Nevertheless, it has become evident at the end of the 20th century that the philosophy of human progress that has manifested itself in a huge production and consumption of goods has a negative side too. It has been recognized that a massive consumption of fossil fuels in order to fulfil the present energy demands has a negative impact on the environment. The deterioration of environment is a clear warning that the present realization of human progress has its limitations. The emerging international environmental consciousness was formulated in a concept of a ***sustainable human progress***. The sustainable human progress is defined as: "… to ensure that it (sustainable development) meets the needs of the present without compromising the ability of future generations to meet their own needs"[1]. A new challenge has emerged at the end of the 20th century that represents a search for and a utilization of new and sustainable energy sources. The urge of this challenge is underlined by limited resources of the fossil fuels on the Earth and increasing demand for energy production. This is the reason why the attention is turning to the ***renewable energy sources***.

Energy is an essence of any human activity. When we are interested in how the human civilization has been producing and using energy, we can describe it in terms of an ***energy system***. The main characteristics of the energy system are: the population, the total consumption of energy, and the sources and forms of energy that people use. The energy system at the beginning of the 21st century is characterised by six billion people that live on the Earth and the total energy consumption of approximately 1.3×10^{10} kW.

[1] World Commission on Environment and Development (WCED), *Our Common Future*, Oxford/New York: Oxford University Press (1987).

1.2 Primary energy sources

Figure 1.1 presents an overview of the present ***primary energy sources*** [2]. The primary energy sources can be divided in two groups. The first group includes those energy sources that will be exhausted by exploiting them. These energy sources are called the ***depleting energy sources*** and they are the fossil fuels and nuclear energy. The fossil fuels and nuclear power are the main source of energy in today's energy system and they supply 78% of the energy demand. Under the assumption that the population of mankind does not change drastically and it consumes energy at the current level, the fossil fuel reserves will be exhausted within 320 years and the nuclear energy within 260 years. This can seem a very long time for us. However, when we compare this period of time to the time span of existence of the Earth or the human civilisation, it is a negligible fraction of time. We have to be aware that the reserves of fossil fuels on the Earth are limited and will be exhausted.

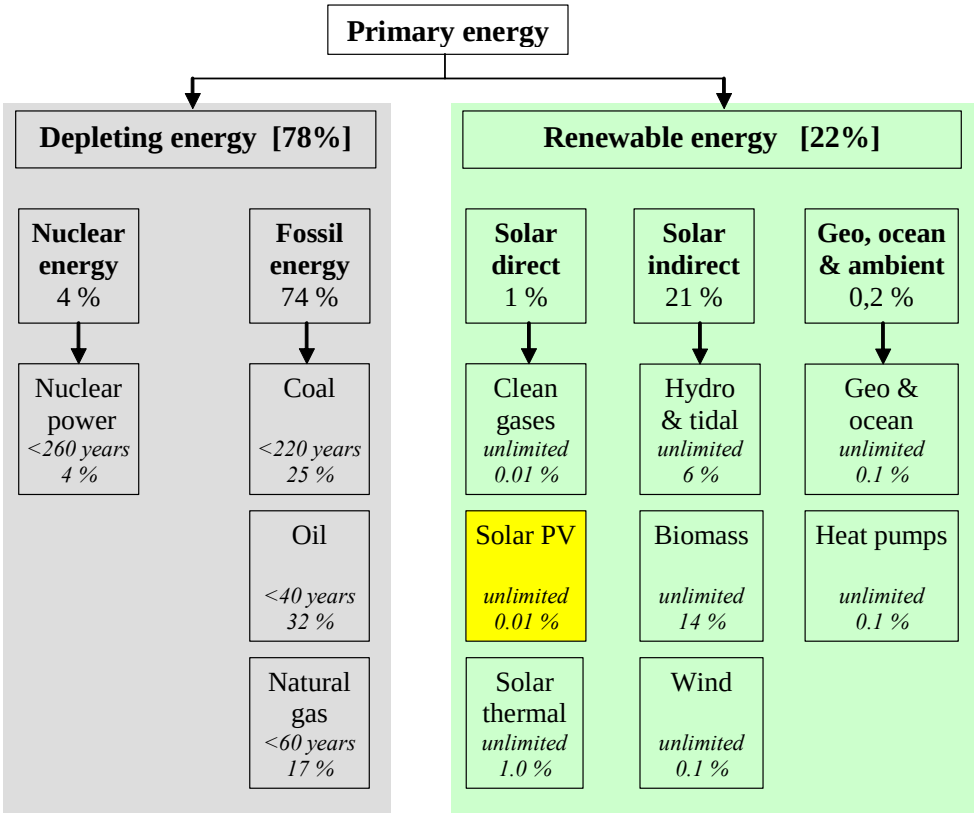

Figure 1.1. An overview of today's energy sources.

[2] D.A. Horazak and J.S. Brushwood, Renewables prospects in today's conventional power generation market, Renewable Energy World, Vol. 2, No. 4, July 1999, p.36.

It is expected that the world population will grow and will reach 10 billion in 2050. In order to provide the growing population with high living standards, further economic development is essential. The further economic development requires more energy than we use today. The extra energy has to come from additional sources than only the traditional ones. Furthermore when we want to take the concept of sustainable development into account, we have to look for environmentally friendly energy sources. These sources are known as ***renewable*** or ***sustainable energy*** sources. The renewable energy sources form the second group of the primary energy sources and today they contribute with 22% to the total energy production. By renewable energy we understand energy that is obtained from the continuing flows of energy occurring in the natural environment, such as solar energy, hydropower and energy from biomass.

About one third of the primary energy is used to generate electric power. This form of energy has become very popular and is widely used for industrial and household applications. The electrical energy represents about 12% of all energy consumed worldwide. Figure 1.2 shows the present distribution of primary energy sources, their contribution to the production of electricity, and the use of electricity.

Since most of the energy production is based on the fossil fuels, these have become a global strategic material. Fossil fuels are not equally distributed over the world and the countries that enjoy huge reserves of fossil fuels can influence the world's economy. The decisions of these countries concerning production levels and price of the fuels have strong effects on the energy production and can result in social tensions. Further, the energy consumption of primary energy is not equal per inhabitant in the world. About ¼ of the world population uses ¾ of the primary energy. For comparison: an inhabitant of the U.S.A. uses on

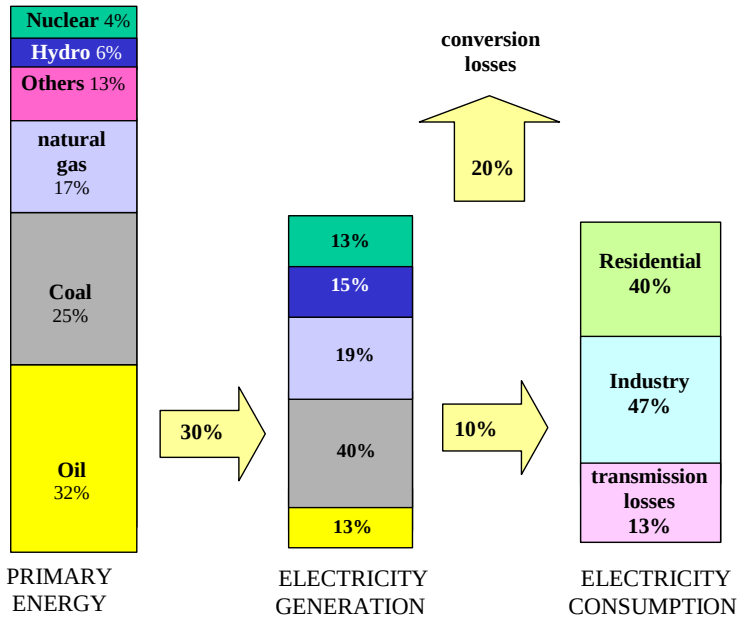

Figure 1.2. Electricity generation and consumption in today's energy system.

average 10 kW of power produced from fossil fuels, while an inhabitant of the Central Africa uses 0.1 kW of power produced from wood. This discrepancy is even more pronounced in the use of electricity. There is no electricity available in most of the rural areas in the developing countries. It is estimated that about 2 billion people have no access to electricity.

It has been recognized that a massive consumption of fossil fuels has a negative impact on the environment. Gases such as CO_2 and SO_X and NO_X are produced as the by-products during burning of the fossil fuels. Enormous quantities of these gases are emitted into the atmosphere, where they change the natural concentrations. The ecological problems, such as the greenhouse effect and acid rains, are caused by the increase of these gases in the atmosphere. The greenhouse effect is linked to the increase of CO_2 in the atmosphere. The CO_2 molecules are transparent to solar radiation but are opaque to heat, which is the radiation in the infrared wavelength region. The concentration of CO_2 in the atmosphere has increased in the 20^{th} century from 280 ppm to 350 ppm. Scientists expect that when this trend continues, the temperature will rise from 3 ºC to 5 ºC in 2030-2050. In order to avoid this situation, in which the climate change, known also as the global warning, can lead to undesired ecological changes a reduction in CO_2 emission is essential.

1.3 Renewable energy sources

The negative aspects of today's energy system have led to the formulation of sustainable human development. The realization of the sustainable development requires an alternative energy system that is based on:

i) policies for efficient energy use and

ii) renewable energy sources.

The world's largest oil company Shell has published recently a vision on future energy consumption and potential energy sources[3]. One of the largest energy producers in the world expects that the restructuring of power industry will take place in near future. The Shell's scenario that is called the "Sustained Growth" is presented in Figure 1.3. The company has concluded that the fossil fuels are still important, but they reach a plateau by 2020. At this time, renewable energy will become a significant source of energy. At first, renewable energy will grow in niche markets rather than compete with traditional sources of energy. The market will decide a share of different forms of renewable energy. In future, the energy supply will become more diversified and hence more robust. It is interesting to notice that Shell expects the photovoltaic (PV) solar energy to become a major energy source within fifty years.

Renewable energy sources are based on the continuing flows of energy that is considered inexhaustible from the point of view of human civilisation. Solar radiation represents such an infinite source of energy for the Earth. The sun delivers 1.2×10^{14} kW energy on the Earth, which is about 10.000 times more than the present energy consumption. The energy that the Earth receives from the sun in just one hour is equal to the total amount of energy consumed by humans in one year.

[3] J. van der Veer and J. Dawson. Shell International Renewables. Web page: http:/www.shell.com, 1997, Transcript of a Press conference in London, 6 October 1997.

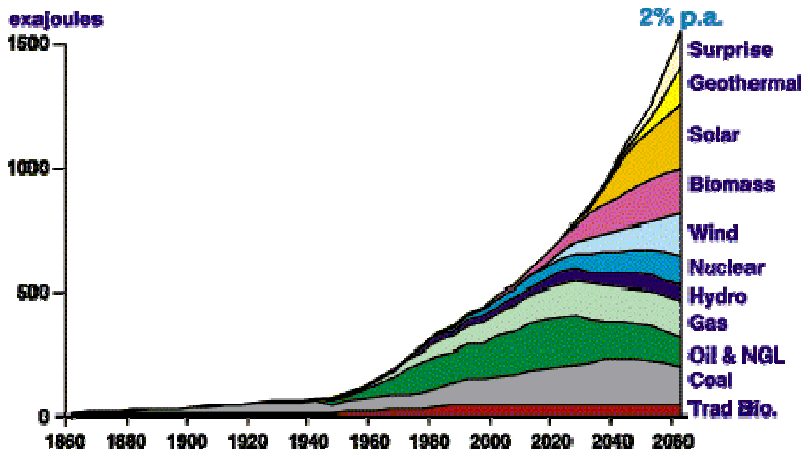

Figure 1.3. Shell's scenario of diversification of energy sources in the 21st century[3].

As illustrated in Figure 1.1 solar radiation can be utilised in various forms. The ***direct utilisation*** of solar radiation uses the energy of light (mostly in the visible wavelength region) or heat (infra-red wavelength region). Light is used for the photovoltaic solar power generation, which means the direct conversion of light into electricity in devices called ***solar cells***, or production of photochemical hydrogen. Heat is used mostly as a water heater in ***solar collectors***. Wind, hydroelectric and wave power generation can be considered examples of the ***indirect utilisation*** of solar radiation. For example, mills for grinding grain, water pumping or electricity generation use energy of the wind. The energy carried by the flow of rivers, by water from reservoirs, or by tidal and wave motion is converted into the hydroelectric power using the turbines. The photosynthesis process creates biomass, which is used for the production of ethanol in case of sugar cane or maize, or for the production of biogas in case of organic household waste. The examples of the geothermal energy sources are geysers or terrestrial heat surfaces, such as steam and hot water, for heating applications.

The major advantages of using renewable energy sources over the traditional energy sources are reflected in a cleaner environment, creating employment opportunities, and security of energy supply. The use of renewable energy can reduce the emission of greenhouse gases and other pollutants. The expanded use of renewable sources of energy can have a positive impact on job creation in the technology manufacturing industries and also the agricultural sector, which supplies biomass fuel. Renewable energy can play an important role in increasing security of energy supply by providing domestic resources of energy and avoiding dependence on imported supplies of fossil fuels.

Today, the renewable energy sources contribute around 22% to energy production, with traditional biomass and hydroelectric power as the main contributors. In Europe, the renewable energy's contribution to the primary energy is 5.3% (1994) in the European Union and 1.7% in Eastern Europe. Since 1989, the use of renewable energy in Europe has been growing at a rate of 2.7% per year, 50% faster than the 1.8% annual growth of the overall

energy market over the same period. It is likely that renewable energy will, by 2020, be one of the three largest sources of energy in Europe, along with gas and nuclear. At present, the level of renewable energy market penetration strongly depends on policies, particularly policies for environment, research and development (R&D), and market support policies. Europe's renewable energy industry is already leading the world in some areas, notably in wind and PV, and is a world pioneer in advanced biomass.

Electricity from renewable sources is today still more expensive than electricity produced from traditional sources. Therefore, a large-scale application of renewable energy sources as electricity power sources is not yet economically attractive in the industrialised countries. The comparison of electricity generating and investment costs for various energy technologies is presented in Table 1[4]. The environmental benefits of renewable technologies are probably the strongest factor for growing market and national policies to encourage renewable energy sources. However, electricity from renewable energy sources is already today the most effective cost solution for two billion people in many parts of the world who have no access to electricity grid.

Table 1.1 Comparison of investment and electricity generating costs for various energy technologies[4].

Technology	**Generating costs** (US cents/kWh)		**Investment costs** (US $/W)	
	Mean	**Range**	**Mean**	**Range**
Gas combined cycle	3.5	3.0-4.0	0.6	0.5-0.7
Coal	4.8	4.0-5.5	1.2	1.0-1.3
Nuclear	6.0	3.3-8.0	1.6	1.2
Wind	5.5	3.0-8.0	1.4	2.0
Biomass 25 MWe combustion	6.5	4.0-9.0	2.0	1.5-2.5
Small hydro	7.5	5.0-10.0	1.0	0.8-1.2
Solar thermal	15.0	12.0-18.0	5.0	4.0-6.0
Solar PV	55.0	30.0-80.0	7.0	6.0-8.0

[4] P. Langcake, Getting a clear view Strategic perspective for renewable energy companies, Renewable Energy World, Vol. 6, No. 2, Mar-Apr 2003.

1.4 Photovoltaic solar energy (solar electricity)

1.4.1 Introduction to photovoltaic solar energy

The energy of solar radiation is directly utilised in mainly two forms:
i) direct conversion into electricity that takes place in semiconductor devices called ***solar cells***
ii) accumulation of heat in ***solar collectors***.

Therefore, do not confuse solar cells with solar collectors. The direct conversion of solar radiation into electricity is often described as a ***photovoltaic*** (PV) energy conversion because it is based on the ***photovoltaic effect***. In general, the photovoltaic effect means the generation of a potential difference at the junction of two different materials in response to visible or other radiation. The whole field of solar energy conversion into electricity is therefore denoted as the "***photovoltaics***". Photovoltaics literally means "light-electricity", because "photo" is a stem from the Greek word "phõs" meaning light and "Volt" is an abbreviation of Alessandro Volta's (1745-1827) name who was a pioneer in the study of electricity. Since a layman often does not know the meaning of the word photovoltaics, a popular and common term to refer to PV solar energy is ***solar electricity***.

The oil company Shell expects that PV solar energy will become the main energy source for the "post-fossil-era"[3]. Developing the PV solar energy as a clean and environmentally friendly energy source is considered at present noble mission. In this mission, the sun is consciously given an additional function to the one that it has had: to provide energy for life on the Earth. The sun's additional function will be to provide the Earth with energy for people's comfort and well being by producing the solar electricity.

The motifs that were behind the development and application of the PV solar energy were in general the same as for all renewable energy sources. The motifs were based on the prevention of climate and environment and providing clean energy for all people. The current motifs can be divided into three categories: energy, ecology and economy.

Energy
There is a growing need for energy in the world and since the traditional energy sources based on the fossil fuels are limited and will be exhausted in future, PV solar energy is considered a promising energy source candidate. Large-scale application of PV solar energy will also contribute to the diversification of energy sources resulting in more equal distribution of energy sources in the world.

Ecology
Large-scale use of PV solar energy, which is considered environmentally friendly source of energy, can lead to a substantial decrease in the emission of gases such as CO_2 and SO_X and NO_X that pollute the atmosphere during burning of the fossil fuels. When we closely look at the contribution of the PV solar energy to the total energy production in the world we see that the PV solar energy contribution is only a tiny part of the total energy production. At present, the total energy production is estimated to be 1.6×10^{10} kW compared to 1.0×10^{6} kW_p that can be delivered by all solar cells installed worldwide. By W_p (Watt peak) we understand a

unit of power that is delivered by a solar cell under a standard illumination. When PV starts to make a substantial contribution to the energy production and consequently to the decrease in the gas emissions depends on the growth rate of the PV solar energy production. When the annual growth of PV solar energy production is 15% then in year 2050 solar cells will produce 2.0×10^8 kW_p. The annual growth of 25% will result in the solar electricity power production of 7.5×10^9 kW_p in 2040 and the annual growth of 40% will lead to power production of 2.4×10^{10} kW_p in 2030. This demonstrates that there must be a steady growth in solar cells production so that PV solar energy becomes a significant energy source after a period of 30 years.

Economy

The solar cells and solar panels are already on the market. An advantage of the PV solar energy is that the solar panels are modular and can be combined and connected together in such a way that they deliver exactly the required power. We refer to this feature as "***custom-made***" energy. The reliability and very small operations and maintenance costs, as well as modularity and expandability, are enormous advantages of PV solar energy in many rural applications. There are two billion people in mostly rural parts of the world who have no access to electricity and solar electricity is already today the most cost effective solution. Bringing solar electricity to these people represents an enormous market. Some companies and people have realised that solar electricity can make money already now and this fact is probably the real ***driving force*** to a widespread development and deployment of the PV solar energy. We can roughly estimate how much money is already involved in the production of solar cells. The total production of solar cells has achieved more than 1200 MW_p. An average cost-prize of 1 W_p. was approximately 3.5 €. This means that the money involved in production of solar cells reached 4.2 milliard €. Assuming that a complete PV system is roughly two times the cost of the cells, a total money involved PV in 2004 can be estimated to 10 milliard €.

The advantages and drawbacks of the PV solar energy, as seen today, are summarized:

Advantages:

- environmentally friendly
- no noise, no moving parts
- no emissions
- no use of fuels and water
- minimal maintenance requirements
- long lifetime, up to 30 years
- electricity is generated wherever there is light, solar or artificial
- PV operates even in cloudy weather conditions
- modular or "custom-made" energy, can be designed for any application from watch to a multi-megawatt power plant

Drawbacks:

- PV cannot operate without light
- high initial costs that overshadow the low maintenance costs and lack of fuel costs
- large area needed for large scale applications
- PV generates direct current: special DC appliances or inverters are neededin *off-grid* applications energy storage is needed, such as batteries

1.4.2 Photovoltaic (PV) system

The solar energy conversion into electricity takes place in a semiconductor device that is called a solar cell. A solar cell is a unit that delivers a certain amount of electrical power that is characterised by an output voltage and current. In order to use solar electricity for practical devices, which require a particular voltage or current for their operation, a number of solar cells are connected together to form a ***solar panel***, also called a ***PV module***. For large-scale generation of solar electricity the solar panels are connected together into a ***solar array***.

The solar panels are part of a complete ***PV solar system***, which, depending on the application, comprises batteries for electricity storage, dc/ac inverters that connect a PV solar system to the electrical grid, and other miscellaneous electrical components or mounting elements. These additional parts of the PV solar system form a second part of the system that is called ***balance of system*** (BOS). Finally, the solar system includes products such as household appliances; radio or TV set that use the solar electricity for their operation. We refer to these products as a load.

In summary, the PV solar system consists of three parts:
i) solar panels or solar arrays,
ii) balance of system,
iii) load.

1.4.3 Photovoltaic technologies

The first practical use of solar cells was the generation of electricity on the orbiting satellite Vanguard 1 in 1958. These first solar cells were made from single crystal silicon wafers and had efficiency of 6 %. The space application was for some time the only application of solar cells. The energy crisis in the seventies of the 20th century accelerated a search of new energy sources for terrestrial applications. This search resulted in a growing interest for PV solar energy. The major obstacle of using solar cells for terrestrial electricity generation has been a much higher price of the solar electricity when compared to the price of electricity generated from the traditional sources. Therefore, there has been much effort in the field of solar cells to reduce the price of solar electricity to a level that is comparable to the conventional electricity. The single crystal silicon wafer-based solar cells that had been used in space became also the first solar cells to be used for terrestrial generation of electricity. In order to increase the efficiency of single crystal silicon solar cells and to lower their price, the crystalline silicon solar cell technology has improved dramatically in the past twenty years and today it is the dominant solar cell technology. Crystalline silicon solar cell technology represents today not only single crystal silicon wafer-based solar cells, but also multi-crystalline silicon solar cells. Both technologies that deal with " bulk" crystalline silicon are considered the ***first generation solar cells*** for terrestrial applications. As this technology has matured, costs have become increasingly dominated by material costs, namely those of the silicon wafer, the glass cover sheet, and encapsulants.

In order to decrease the material costs of crystalline silicon solar cells, research has been directed to develop ***low cost thin-film solar cells***, which represent a ***second generation solar cells*** for terrestrial application. There are several semiconductor materials that are potential candidates for thin-film solar cells, namely copper indium gallium diselenide ($CuInGaSe_2$=CIGS), cadmium telluride (CdTe), hydrogenated amorphous silicon (*a*-Si:H),

thin-film polycrystalline silicon (*f*-Si). The titanium oxide nanocrystals covered with organic molecules represent so called dye-sensitized nano-structred solar cells. It is expected that the efficiency of commercial second generation solar modules is likely to reach 15%.

Conversion efficiency has to be increased substantially in order to progress further. Calculations based on thermodynamics demonstrate that the limit on the conversion efficiency of sunlight to electricity is 93% as opposed to the upper limit of 33% for a single junction solar cell, such as a silicon wafer and most present thin-film solar cells. This suggests that the performance of solar cells could be improved 2-3 times when different concepts were used to produce a ***third generation*** of high efficiency, thin-film solar cells.

1.4.4 Photovoltaic applications and market

Figure 1.4 presents an overview of the different solar cell technologies that are used or being developed for two main solar cell applications, namely space and terrestrial applications. The conversion efficiency of solar cells used in space applications is the initial efficiency measured before the solar cells are launched into the space. This conversion efficiency is also referred to as the begin-of-life efficiency. Today's commercial PV systems in terrestrial applications convert sunlight into electricity with efficiency ranging from 7% to 17%. They are highly reliable and most producers give at least 20 years guarantee on module performance. In case of the thin-film solar cells the best conversion efficiency that has been achieved in laboratory is shown together with the conversion efficiency that is typical for commercial solar cells.

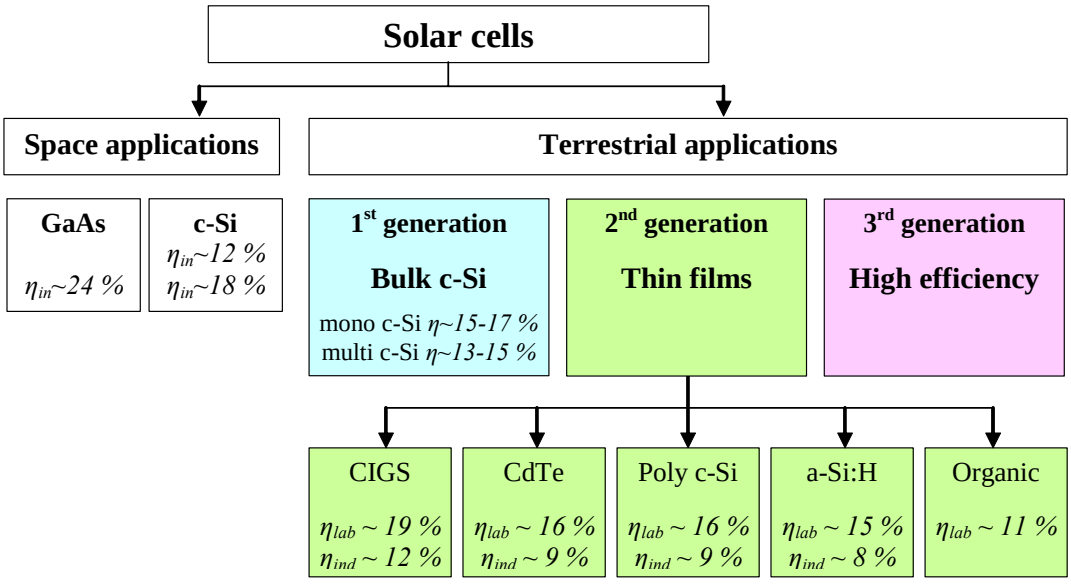

Figure 1.4. Overview of solar cell applications and of several types of solar cells used in different applications.

The commercial production of solar ells is steadily increasing and from 1996, the average increase is around 30%. The growth of the solar cell production is depicted in Figure

1.5 [5,6]. The total commercial production of solar cells in 2004 was 1GW$_p$ and was 1250 MW$_p$. As illustrated in Figure 1.5 almost all commercial solar modules were produced from silicon. Crystalline silicon based solar cells amounted to 95% of the total production and were the dominant solar cell technology. The *a*-Si:H technology contributed with 4% to the total production in 2004. The only non-silicon technology that was delivering commercial modules was the CIS and CdTe technology with almost 1% from the total production. In 2004 most of the solar modules were manufactured in Japan (47%), the USA contributed with 11%, and Europe with 27%, the rest of the solar cells was produced in countries such as China, India and Australia.

The PV solar systems are already an important part of our lives. The simplest PV solar systems power many of the small calculators and wrist watches that we use every day. More complicated systems provide electricity for pumping water, powering communications equipment, and even lighting our homes and running our household appliances.

At present, there are four primary market areas for photovoltaic terrestrial applications:

i) Consumer products, such as watches, calculators, and lanterns.
ii) Off-grid, also called stand alone, residential power systems, such as solar home systems for individual households.
iii) Off-grid industrial power systems for water management, lighting, and telecommunication.
iv) Grid connected PV systems that are integrated in roofs and outer walls of buildings or in noise barriers along the motorways.

Table 1.2 demonstrates the evolution of the share of PV modules in different market sectors. It is interesting to note that from 1996 the most growing market for PV modules are the grid connected PV systems that are integrated in roofs and outer walls of buildings.

Table 1.2: The share of PV modules in different market sectors[6].

Market sector	1993	1996	1999	2001	2003
	[MW$_p$]	[MW$_p$]	[MW$_p$]	[MW$_p$]	[MW$_p$]
Consumer products	18	22	35	45	65
US off-grid residential	5	8	13	19	30
World off-grid rural	8	15	31	45	70
Communications/signal	18	23	35	46	70
PV/diesel commercial	10	12	25	36	50
Grid connected	2	7	60	199	365
Central power	2	2	2	5	8
Total	**63**	**89**	**201**	**395**	**658**

[5] Photon International No. 3 (2005).
[6] P.D. Maycock, Renewable Energy World, Vol. 2, No. 4, July 1999.

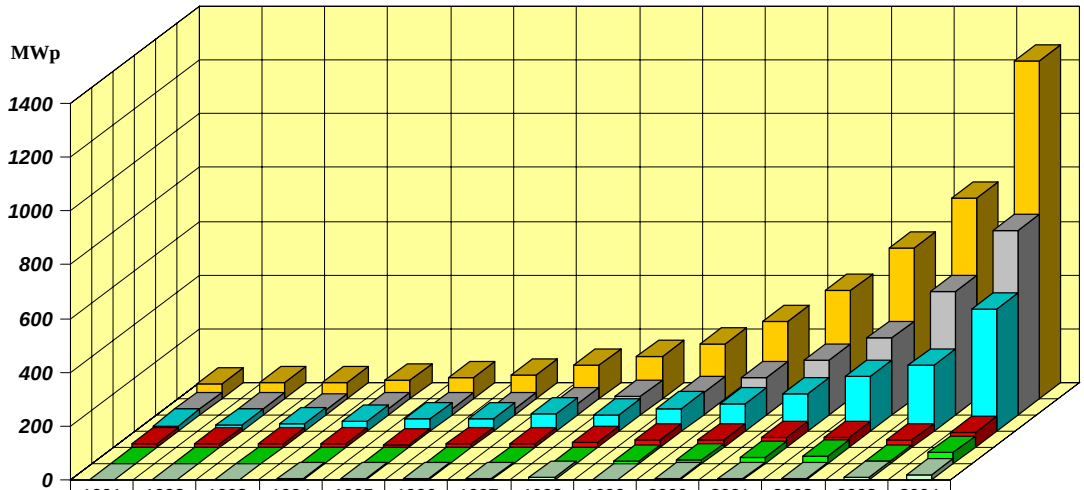

	1991	1992	1993	1994	1995	1996	1997	1998	1999	2000	2001	2002	2003	2004
rest	1.0	1.0	1.0	2.0	4.0	6.0	6.0	7.0	0.7	3.6	2.8	5.0	7.0	19.0
ribbon Si	0.0	0.0	0.0	0.0	0.0	0.0	0.0	0.0	6.3	14.7	22.5	26.3	6.8	41.0
a-Si	14.0	15.0	13.0	11.0	9.0	12.0	15.0	19.0	24.8	27.0	35.8	35.8	25.8	55.2
mono c-Si	20.0	22.0	29.0	36.0	47.0	47.0	62.0	60.0	85.0	102.0	138.7	201.4	244.0	455.0
multi c-Si	21.0	20.0	18.0	21.0	20.0	24.0	43.0	67.0	84.5	140.0	201.6	288.7	459.8	687.0
Total	55.4	57.9	60.1	69.4	77.6	88.6	125.8	154.9	201.3	287.7	401.4	559.6	744.1	1256.8

Figure 1.5. Commercial production of solar cells per technology.

Major national and international investments in research, development, demonstration and dissemination resulted in important technical improvements and a drop of the price of PV modules by a factor of more than 20 over the last two decades. In 1990 PV module costs were in the range US$5-6/$W_p$. This has now decreased to US$3.5-4.00/$W_p$. The cost of a PV system is about twice of PV module. The cost of solar electricity depends on the performance of the PV module. The solar cell performance, which is characterized by the conversion efficiency, has been improved. Commercial PV modules, which are made from crystalline silicon solar cells, have efficiencies of 12 to 17%. Further reductions in the cost of crystalline silicon solar cells are anticipated due to improved production methods, increases in efficiency of solar cells and reductions in the costs of producing modules. These could results in module costs of $2/$W_p$ by 2005. Amorphous silicon technology, which has a potential to become a low cost technology, delivers today modules with efficiencies of 5 to 8 %.

The world sales of PV modules in 1997 were around 0.5 billion US$. As costs decline and technology improves, more markets will be captured, leading to production increase and further cost reduction. Shell has predicted that a successful development of the PV business would involve annual 22% market growth linked to an annual 6% cost reduction in real terms. Current predictions show a 6 billion dollar global market for PV systems by 2010.

Chapter 2.

SOLAR RADIATION

2.1 Solar radiation

One of the basic processes behind the photovoltaic effect, on which the operation of solar cells is based, is generation of the electron-hole pairs due to absorption of visible or other electromagnetic radiation by a semiconductor material. Today we accept that electromagnetic radiation can be described in terms of waves, which are characterized by wavelength (λ) and frequency (ν), or in terms of discrete particles, ***photons***, which are characterized by energy ($h\nu$) expressed in electron volts. The following formulas show the relations between these quantities:

$$\nu = c/\lambda \tag{2.1}$$

$$h\nu = \frac{1}{q}\frac{hc}{\lambda} \tag{2.2}$$

In Eqs. 2.1 and 2.2 c is the speed of light in vacuum (2.998×10^{8} m/s), h is Planck's constant (6.625×10^{-34} Js), and q is the elementary charge (1.602×10^{-19} C). For example, a green light can be characterized by having a wavelength of 0.55×10^{-6} m, frequency of 5.45×10^{14} s^{-1} and energy of 2.25 eV.

Only photons of appropriate energy can be absorbed and generate the electron-hole pairs in the semiconductor material. Therefore, it is important to know the spectral distribution of the solar radiation, i.e. the number of photons of a particular energy as a function of wavelength. Two quantities are used to describe the solar radiation spectrum, namely the ***spectral power density***, $P(\lambda)$, and the ***photon flux density***, $\Phi(\lambda)$. The spectral power density is the incident power of solar radiation per unit area and per unit wavelength [W m^{-2} m^{-1}]. The total power from a radiant source falling on a unit area is also called ***irradiance***. The photon flux density is the number of photons per unit area, per unit time, and per unit wavelength [ph m^{-2} s^{-1} m^{-1}]. The photon flux density is related to the spectral power density by:

$$\Phi(\lambda) = P(\lambda)\frac{\lambda}{h\,c} \tag{2.3}$$

Each second, the sun releases an enormous amount of radiant energy into the solar system. The temperature at the centre of the sun is high enough to facilitate nuclear reactions, which are assumed to be the source of the sun's energy. The temperature at the centre is of the order of 10^6 degrees but the temperature of the surface layer of the sun, so called ***photosphere***, is about 6000K. The extraterrestrial spectrum of sun's radiant energy can be approximated by that of a black-body radiator at this temperature. The total power density of the solar radiation at the mean earth-sun distance on a plane perpendicular to the direction of the sun, outside the earth's atmosphere, is referred to as the ***solar constant***. Its value is 1353 W/m^2.

The solar radiation is attenuated, when it passes through the earth's atmosphere. Since the spectral distribution of the solar radiation also depends on the attenuation, various solar spectra can be measured at the earth's surface. The degree of attenuation is variable. The most important parameter that determines the solar irradiance under clear sky conditions is the distance that the sunlight has to travel through the atmosphere. This distance is the shortest when the sun is at the zenith, i.e. directly overhead. The ratio of an actual path length of the sunlight to this minimal distance is known as the ***optical air mass***. When the sun is at its zenith the optical air mass is unity and the radiation is described as ***air mass one*** (AM1) radiation. When the sun is at an angle θ to the zenith, the air mass is given by

$$Air\ mass = (\cos\theta)^{-1} \tag{2.4}$$

For example, when the sun is 60 degrees from the zenith, the radiation is described as AM2. The solar radiation spectrum is also a function of air mass. The spectral power density of some commonly used air mass radiation spectra are presented in Figure 2.1. AM0 radiation is the extraterrestrial spectrum of solar radiation outside the earth's atmosphere, which power density is the solar constant. Opposed to the situation outside the earth's atmosphere, terrestrial solar radiation varies both in intensity and spectral distribution depending on the position on the earth and the position of the sun in the sky. In order to allow comparison between the performances of solar cells tested at different locations, a terrestrial solar radiation standard has to be defined and measurements referred to this standard. ***AM1.5 radiation*** serves at present as the standard spectral distribution. It corresponds to an angle of 48.2 degrees between the sun's position and the zenith. The irradiance of the AM1.5 radiation

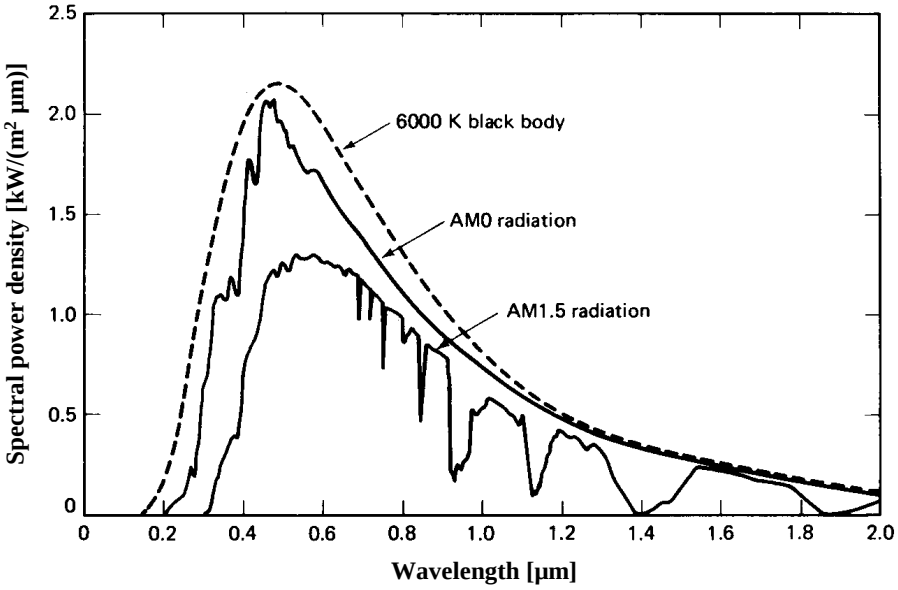

Figure 2.1. Spectral power density of sunlight. The different spectra refer to the black-body radiation at 6000K, the extraterrestrial AM0 radiation and the AM1.5 radiation.

is 827 W/m^2. The value of 1000 W/m^2 was incorporated to become a standard. This value of the irradiance is close to the maximum received at the earth's surface. The peak power of a photovoltaic system is the power generated under this standard AM1.5 (1000 W/m^2) radiation and is expressed in peak watts.

The attenuation of solar radiation is due to scattering and absorption by air molecules, dust particles and/or aerosols in the atmosphere. Especially, steam, oxygen and carbon dioxide (CO_2) cause absorption, which is wavelength-selective and therefore results in gaps in the spectral distribution of solar radiation as apparent in Figure 2.1. Ozone absorbs radiation with wavelengths below 0.3 μm. Depletion of ozone from the atmosphere allows more ultra-violet radiation to reach the earth, with consequent harmful effects upon biological systems. CO_2 molecules contribute to the absorption of solar radiation at wavelengths above 1 μm. By changing the CO_2 content in the atmosphere the absorption of the infrared solar spectrum is influenced, which has consequences for the earth's climate.

The actual amount of solar radiation that reaches a particular place on the earth is extremely variable. In addition to the regular daily and yearly variation due to the apparent motion of the sun, irregular variations are caused by local atmospheric conditions, such as clouds. These conditions particularly influence the direct and diffuse components of solar radiation. The ***direct*** component of solar radiation is that part of the sunlight that directly reaches the earth's surface. Scattering of the sunlight in the atmosphere generates the ***diffuse*** component. A part of the solar radiation that is reflected by the earth's surface, which is called ***albedo***, may be also present in the total solar radiation. We use a term ***global*** radiation to refer to the total solar radiation, which is made up of these three components.

The design an optimal photovoltaic system for a particular location depends on the availability of the solar insolation data at the location. Solar irradiance integrated over a period of time is called ***solar irradiation***. For example, the average annual solar irradiation in The Netherlands is 1000 kWh/ m^2, while in Sahara the average value is 2200 kWh/ m^2.

2.2 The sun

Many people on the Earth are fascinated by the existence of the sun. There are several examples in human history that the sun became an object of worship and people believed that it possessed divine powers. No wonder, the sun is the source of all life on the Earth. The sun is an intensely hot, self-luminous body of gases (mainly hydrogen and helium) at the centre of the solar system. Figure 2.2 shows a photograph of the sun. The sun is a medium-size main-sequence star. Here are some basic technical facts about the sun[1].

Mean distance from the earth:	149 600 000 km (the astronomic unit)
Diameter:	1 392 000 km (109 × that of the earth)
Volume:	1,300,000 times that of the earth
Mass:	$1{,}993 \times 10^{27}$ kg (332 000 times that of the earth)
Density (at its center):	$>100 \times 10^3$ kg m^{-3} (over 100 times that of water)
Pressure (at its center):	over 1 billion atmospheres
Temperature (at its center):	about 15 000 000 degrees Kelvin
Temperature (at the surface):	6 000 degrees Kelvin
Energy radiation:	380×10^{21} kW
The Earth receives:	170×10^{12} kW

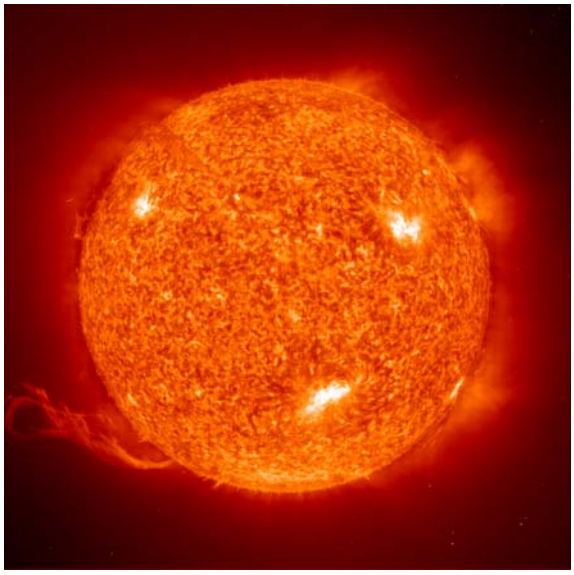

Figure 2.2. A fascinating photograph of the sun.

[1] The Concise Columbia Electronic Encyclopaedia, Third Edition Copyright © 1994, Columbia University Press.

Chapter 3.

SEMICONDUCTOR MATERIALS FOR SOLAR CELLS

3.1 Solar cell structure

In most of today solar cells the absorption of photons, which results in the generation of the charge carriers, and the subsequent separation of the photo-generated charge carriers take place in ***semiconductor materials***. Therefore, the semiconductor layers are the most important parts of a solar cell; they form the hart of the solar cell. There are a number of different semiconductor materials that are suitable for the conversion of energy of photons into electrical energy, each having advantages and drawbacks. In this chapter the most important semiconductor properties that determine the solar cell performance will be discussed.

The crystalline silicon (c-Si) solar cell, which dominates the PV market at present, has a simple structure, and provides a good example of a typical solar cell structure. Figure 3.1 shows the essential features of c-Si solar cells. An absorber material is typically a moderately-doped *p*-type square wafer having thickness around 300 μm and an area of 10×10 cm^2 or 12.5×12.5 cm^2. On both sides of the c-Si wafer a highly doped layer is formed, n^+-type on the top side and p^+-type on the back side, respectively. These highly doped layers help to separate the photo-generated charge carriers from the bulk of the c-Si wafer. The trend in the photovoltaic industry is to reduce the thickness of wafers up to 250 μm and to increase the area to 20×20 cm^2.

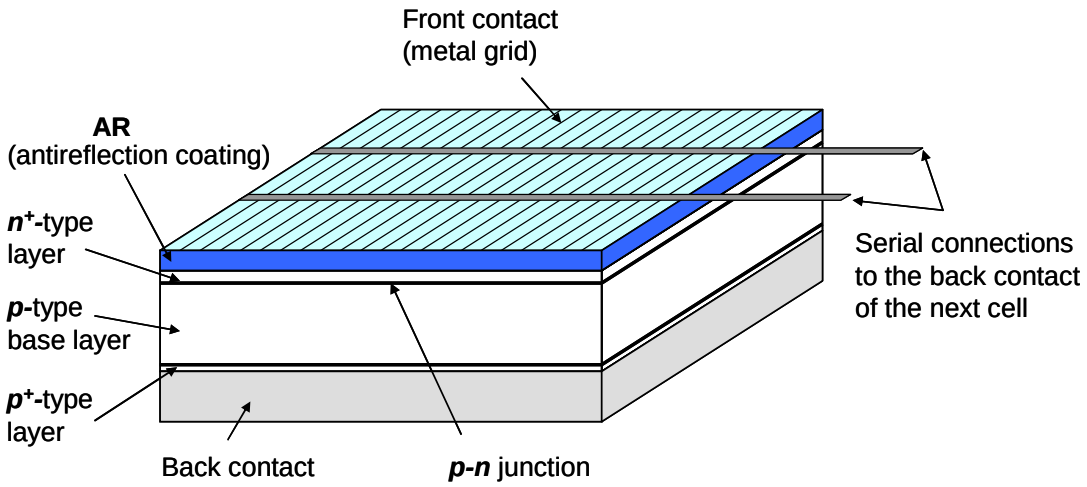

Figure 3.1. A typical structure of a c-Si solar cell.

In addition to semiconductor layers, solar cells consist of a top and bottom metallic grid or another electrical contact that collects the separated charge carriers and connects the cell to a load. Usually, a thin layer that serves as an antireflective coating covers the topside of the cell in order to decrease the reflection of light from the cell. In order to protect the cell against the effects of outer environment during its operation, a glass sheet or other type of transparent encapsulant is attached to both sides of the cell. In case of thin-film solar cells, layers that constitute the cell are deposited on a substrate carrier. When the processing temperature during the deposition of the layers is low, a wide range of low-cost substrates such as glass sheet, metal or polymer foil can be used.

The first successful solar cell was made from c-Si and c-Si is still the most widely used PV material. Therefore we shall use c-Si as an example to explain semiconductor properties that are relevant to solar cell operation. This gives us a basic understanding of how solar cells based on other semiconductor materials work. The ***central semiconductor parameters*** that determine the design and performance of a solar cell are:

i) concentrations of doping atoms, which can be of two different types; donor atoms which *donate* free electrons, N_D, or acceptor atoms, which *accept* electrons, N_A. The concentrations determine the width of a space-charge region of a junction.

ii) mobility, μ, and diffusion coefficient, D, of charge carriers that characterize carriers transport due to drift and diffusion, respectively.

iii) lifetime, τ, and diffusion length, L, of the excess carriers that characterize the recombination-generation processes.

iv) band gap energy, E_G, absorption coefficient, α, and refractive index, n, that characterize the ability of a semiconductor to absorb visible and other radiation.

3.2 Semiconductor properties

3.2.1 Atomic structure

The atomic number of Si atom is 14, it means there are 14 electrons orbiting the nucleus. In ground state configuration a Si atom has four valence electrons. These valence electrons are most important because they form the bonds with other Si atoms. Two Si atoms are bonded together when they share each other's valence electron. This is the so called covalent bond that is formed by two electrons. Since Si atom has four valence electrons it can be covalently bonded to four other Si atoms. In the crystalline form each Si atom is covalently bonded to four neighbouring Si atoms. All bonds have the same length and the angles between the bonds are equal. The number of bonds that an atom has with its immediate neighbours in the atomic structure is called the ***coordination number*** or ***coordination***. Thus, in single crystal silicon, the coordination number for all Si atoms is four, we can also say that Si atoms are fourfold coordinated. A ***unit cell*** can be defined, from which the crystal lattice can be reproduced by duplicating the unit cell and stacking the duplicates next to each other. Such a regular atomic arrangement is described as a structure with ***long range order***.

A diamond lattice unit cell represents the real lattice structure of single crystal silicon. Figure 3.2a shows the arrangement of the unit cell and Figure 3.2b the atomic structure of single crystal silicon. One can determine from Figure 3.2a that there are effective eight Si atoms in the volume of the unit cell. When a lattice constant of c-Si is 5.4 Å one can easily calculate that there are approximately 5×10^{22} Si atoms per cm^3. Figure 3.2 shows the crystalline Si atomic structure with no foreign atoms. In practice, a semiconductor sample always contains some impurity atoms. When the concentration of impurity atoms in a semiconductor is insignificant we refer to such semiconductor as an ***intrinsic semiconductor***.

At practical operational conditions, for example room temperature, there are always some of the covalent bonds broken. The breaking of the bonds results in liberating the valence electrons from the bonds and making them mobile through the crystal lattice. We refer to these electrons as free electrons (henceforth simply referred as electrons). The position of a missing electron in a bond, which can be regarded as positively charged, is referred to as a hole. This situation can be easily visualized by using the ***bonding model*** shown in Figure 3.3.

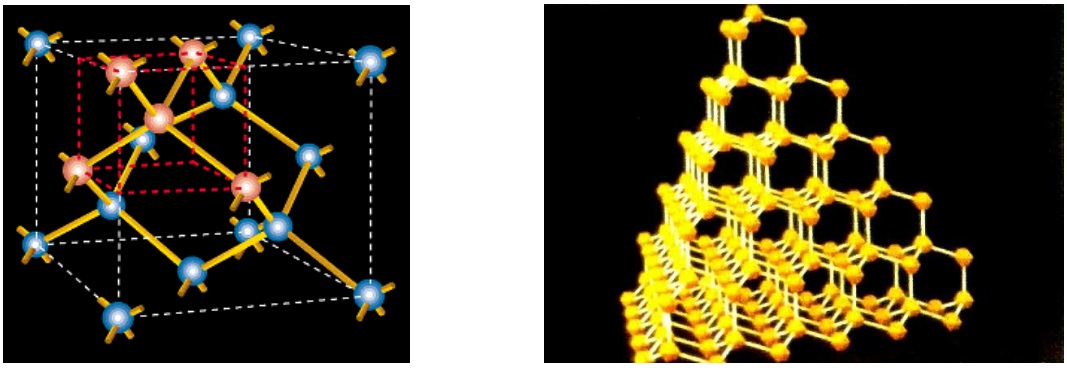

Figure 3.2. (a) A diamond lattice unit cell representing a unit cell of single crystal Si, (b) the atomic structure of a part of single crystal Si.

In the bonding model the atomic cores (atoms without valence electrons) are represented by circles and the valence or bonding electrons are represented by lines interconnecting the circles. In case of c-Si one Si atom has four valence electrons and four nearest neighbours. Each of the valence electron is equally shared with the nearest neighbour. There are therefore eight lines terminating on each circle. In an ideal Si crystal at 0°K all valence electrons take part in forming covalent bonds between Si atoms and therefore are no free electrons in the lattice. This situation is schematically shown in Figure 3.3a. At temperatures higher than 0°K the bonds start to break due to absorbing thermal energy. This process results in creation of mobile electrons and holes. Figure 3.3b shows a situation when a covalent bond is broken and one electron departs from the bond leaving a hole behind. A single line between the atoms in Figure 3.3b represents the remaining electron of the broken bond. When a bond is broken and a hole created, a valence electron from a neighbouring bond can "jump" into this empty position and restore the bond. The consequence of this transfer is that at the same time the jumping electron creates an empty position in its original bond. The subsequent "jumps" of a valence electron can be viewed as a motion of the empty position, hole, in the direction opposite to the motion of the valence electron through the bonds.

Because breaking of a covalent bond leads to the formation of an electron-hole pair, in intrinsic semiconductors the concentration of electrons is equal to the concentration of holes. At 300°K there are approximately 1.5×10^{10} broken bonds per cm^3 in the intrinsic c-Si. This number then gives also the concentration of holes, p, and electrons, n, in the intrinsic c-Si. It means, that at 300°K $n = p = 1.5 \times 10^{10}$ cm^{-3}. This concentration is called the ***intrinsic carrier concentration*** and is denoted n_i.

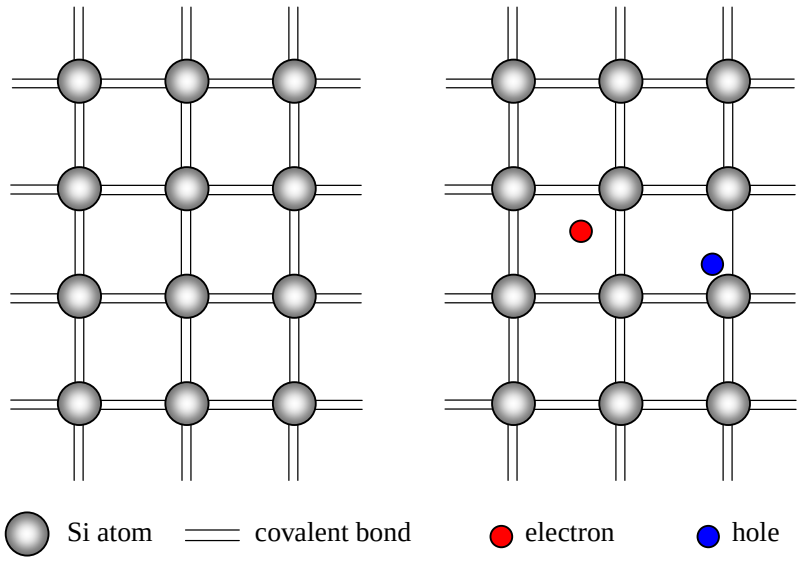

Figure 3.3. The bonding model for c-Si. (a) No bonds are broken. (b) A bond between two Si atoms is broken resulting in a mobile electron and hole.

3.2.2 Doping

The concentrations of electrons and holes in c-Si can be manipulated by doping. By doping c-Si we understand that atoms of appropriate elements substitute Si atoms in the crystal lattice. The substitution has to be carried out by atoms with three or five valence electrons, such as boron or phosphorous, respectively. The doping action can best be understood with the aid of the bonding model and is demonstrated in Figure 3.4.

When introducing phosphorous atom into the c-Si lattice, four of the five phosphorous atom valence electrons will readily form bonds with the four neighbouring Si atoms. The fifth valence electron cannot take part in forming a bond and becomes rather weakly bound to the phosphorous atom. It is easily liberated from the phosphorous atom by absorbing the thermal energy, which is available in the c-Si lattice at room temperature. Once free, the electron can move throughout the lattice. In this way the phosphorous atom that substitutes a Si atom in the lattice "*donates*" a free (mobile) electron into the c-Si lattice. The impurity atoms that enhance the concentration of electrons are called ***donors***. We donate the concentration of donors N_D.

An atom with three valence electrons such as boron cannot form all bonds with four neighbouring Si atoms when it substitutes a Si atom in the lattice. However, it can readily "*accept*" an electron from a nearby Si-Si bond. A thermal energy that the c-Si lattice contains at room temperature is sufficient to enable an electron from a nearby Si-Si bond to attach itself to the boron atom and complete the bonding to the four Si neighbours. In this process a hole is

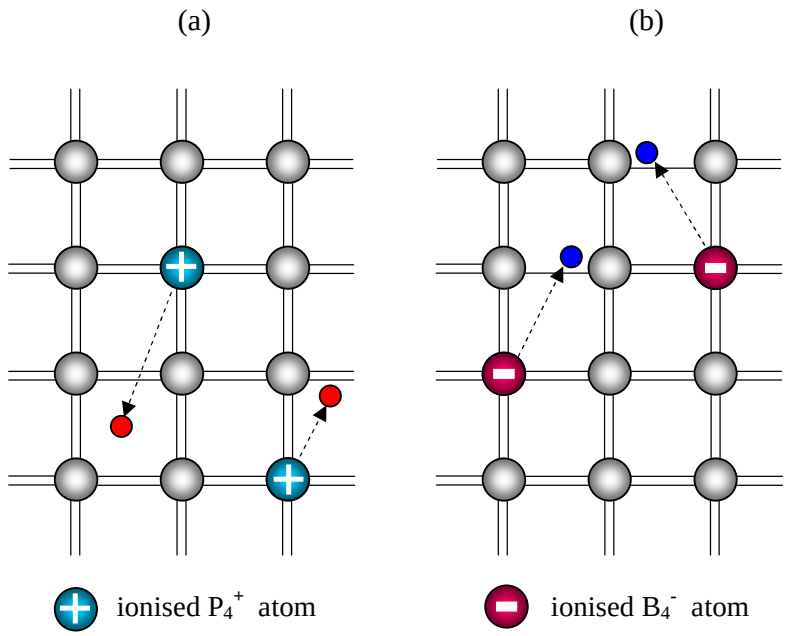

Figure 3.4. The doping process illustrated using the bonding model. (a) A P atom substitutes a Si atom in the lattice resulting in the positively-ionised P atom and a free electron, (b) A B atom substitutes a Si atom resulting in the negatively ionised B atom and a hole.

created that can move around the lattice. The impurity atoms that enhance the concentration of holes are called ***acceptors***. We denote the concentration of donors N_A. Note that by substituting Si atoms with only one type of impurity atoms, the concentration of only one type of mobile charge carriers is increased. Charge neutrality of the material is nevertheless maintained because the sites of the bonded and thus fixed impurity atoms become charged. The donor atoms become positively ionised and the acceptor atoms become negatively ionised.

A possibility to control the electrical conductivity of a semiconductor by doping is one of most important semiconductor features. The electrical conductivity in semiconductors depends on the concentration of electrons and holes and their mobility. The concentration of electrons and holes is influenced by the amount of the impurity atoms that are introduced into the atomic structure of semiconductor. Figure 3.5 shows the range of doping that is used in case of c-Si. We denote a semiconductor a ***p*-type** or ***n*-type** when holes or electrons, respectively, dominate its electrical conductivity. In case that one type of charge carriers has a higher concentration than the other type these carriers are called ***majority*** carriers (holes in the *p*-type and electrons in the *n*-type), while the other type with lower concentration are then called ***minority*** carriers (electrons in the *p*-type and holes in the *n*-type).

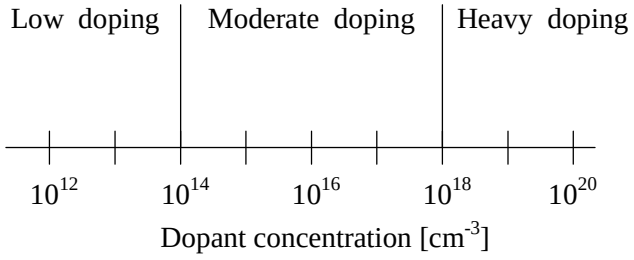

Figure 3.5. The range of doping levels used in c-Si.

3.2.3 Carrier concentrations

Any operation of a semiconductor device depends on the carriers that carry charge inside the semiconductor and cause electrical currents. In order to determine and/or to understand device operation it is important to know the precise number of these charge carriers. In the following section the concentrations of charge carriers inside a semiconductor are derived assuming the semiconductor is under ***equilibrium***. The term equilibrium is used to describe the unperturbed state of a system, to which no external voltage, magnetic field, illumination, mechanical stress, or other perturbing forces are applied. In the equilibrium state the observable parameters of a semiconductor do not change with time.

In order to determine the carrier concentration one has to know the function of density of allowed energy states of electrons and the occupation function of the allowed energy states. The density of energy states function, *g(E),* describes the number of allowed states per unit

volume and energy. The occupation function is the well known Fermi-Dirac distribution function, *f(E),* which describes the ratio of states filled with an electron to total allowed states at given energy *E*. In an isolated Si atom, electrons are allowed to have only discrete energy values. The periodic atomic structure of single crystal silicon results in the ranges of allowed energy states for electrons that are called ***energy bands*** and the excluded energy ranges, ***forbidden gaps*** or ***band gaps***. Electrons that are liberated from the bonds determine the charge transport in a semiconductor. Therefore, we further discuss only those bands of energy levels, which concern the valence electrons. Valence electrons, which are involved in the covalent bonds, have their allowed energies in the ***valence band*** (VB) and the allowed energies of electrons liberated from the covalent bonds form the ***conduction band*** (CB). The valence band is separated from the conduction band by a band of forbidden energy levels. The maximum attainable valence-band energy is denoted E_V, and the minimum attainable conduction-band energy is denoted E_C. The energy difference between the edges of these two bands is called the band gap energy or band gap, E_G, and it is an important material parameter.

$$E_G = E_C - E_V \tag{3.1}$$

The band gap of the single crystal silicon is of 1.12 eV at room temperature. An electron-volt is equal to the energy, which an electron acquires when it passes through a potential of 1 volt in vacuum ($1\text{eV} = 1.602 \times 10^{-19}$ J). A plot of allowed electron energy states as a function of position is called the energy band diagram and for intrinsic c-Si is shown in Figure 3.6.

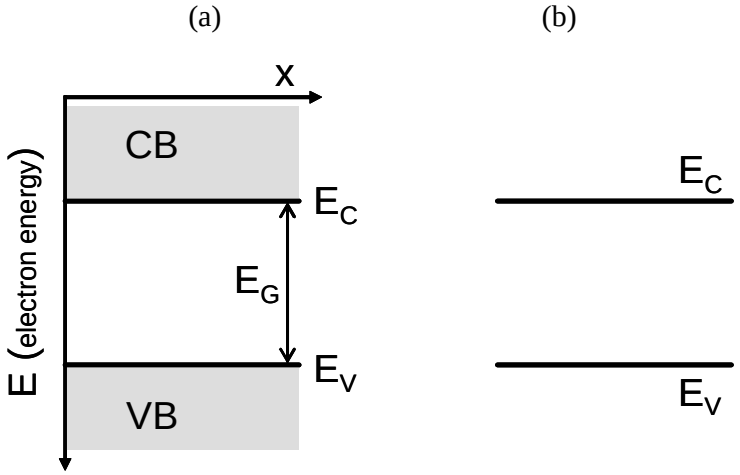

Figure 3.6. (a) The basic energy band diagram and (b) widely used simplified version of the energy diagram.

The density of energy states at an energy *E* in the conduction band close to E_c and in the valence band close to E_v are given by Eqs. (3.1).

$$g_C(E) = \left(\frac{4\sqrt{2}\,\pi m_n^*}{h^3} \right)^{3/2} (E - E_C)^{1/2} \tag{3.2a}$$

$$g_V(E) = \left(\frac{4\sqrt{2}\,\pi m_p^*}{h^3} \right)^{3/2} (E - E_V)^{1/2} \tag{3.2b}$$

where m_n^* and m_p^* is the effective mass of electrons and holes, respectively, averaged over different directions to take anisotropy into account. The Fermi-Dirac distribution function is given by

$$f(E) = \frac{1}{1 + \exp\left[(E - E_F)/kT \right]} \tag{3.3}$$

where k is Boltzmann's constant ($k = 1.38 \times 10^{-23}$ JK^{-1}) and E_F is the so-called Fermi energy. kT is expressed in eV and equals to 0.0258 eV at 300°K. The ***Fermi energy*** is the electrochemical potential of the electrons in a material and in this way it represents the averaged energy of electrons in the material. The Fermi-Dirac distribution function is shown in Figure 3.7 for different temperatures.

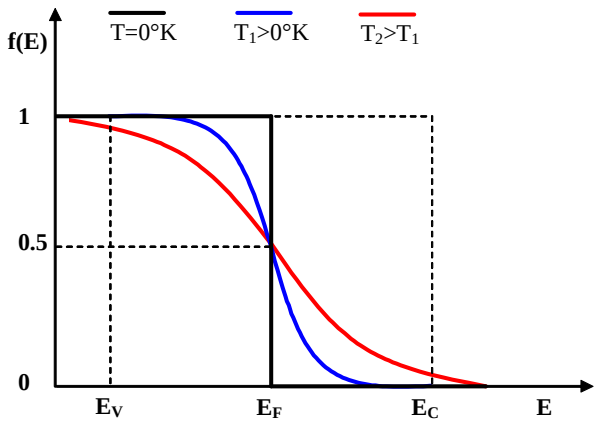

Figure 3.7. The Fermi-Dirac distribution function. For T = 0°K, all allowed states bellow the Fermi level are occupied by two electrons. At T > 0°K not all states below the Fermi level are occupied and there are some states above the Fermi level that are occupied.

The carriers that contribute to charge transport are electrons in the conduction band and holes in the valence band. The total concentration of electrons in the conduction band and the total concentration of holes in the valence band is obtained by multiplying the appropriate

density of states function with the appropriate distribution function and integrate over the whole energy band.

$$n = \int_{E_C}^{E_{top}} g_C(E) f(E) dE \tag{3.4a}$$

$$p = \int_{E_{bottom}}^{E_V} g_V(E)\left[1 - f(E)\right] dE \tag{3.4b}$$

Substituting the density of states and the Fermi-Dirac distribution function into Eq. (3.4) the resulting expressions for n and p are obtained after solving the equations. The full derivation can be found for example in reference [1].

$$n = N_C \exp\left[\left(E_F - E_C\right)/kT\right] \qquad \text{for } E_C - E_F \geq 3kT \tag{3.5a}$$

$$p = N_V \exp\left[\left(E_V - E_F\right)/kT\right] \qquad \text{for } E_F - E_V \geq 3kT \tag{3.5b}$$

where N_C and N_V are the effective density of conduction band states and the effective density of valence band states, respectively. In c-Si $N_C = 3.22 \times 10^{19}$ cm^{-3} and $N_V = 1.83 \times 10^{19}$ cm^{-3} at 300°K. When the requirement that the Fermi level lies in the band gap more than $3kT$ from either band edge is satisfied the semiconductor is referred to as ***nondegenerate***.

In an intrinsic semiconductor in the equilibrium $n = p = n_i$. When multiplying the corresponding sides of Eqs. (3.5) one obtains

$$np = n_i^2 = N_C N_V \exp\left[\left(E_V - E_C\right)/kT\right] = N_C N_V \exp\left[-E_g/kT\right], \tag{3.6}$$

which is independent of the position of the Fermi level and is valid also for doped semiconductors. When we denote the position of the Fermi level in the intrinsic material E_i one can write

$$n_i = N_C \exp\left[\left(E_i - E_C\right)/kT\right] = N_V \exp\left[\left(E_V - E_i\right)/kT\right] \tag{3.7}$$

From Eq. (3.7) we can easily the position of E_i, which is given by

$$E_i = \frac{E_C + E_V}{2} + \frac{kT}{2}\ln\left(\frac{N_V}{N_C}\right) = E_C - \frac{E_g}{2} + \frac{kT}{2}\ln\left(\frac{N_V}{N_C}\right) \tag{3.8}$$

The Fermi level E_i lies close to the midgap; a slight shift is caused by the difference in the effective densities of the valence and conduction band.

It has been already mentioned in Section 3.2.2 that the concentrations of electrons and holes in c-Si can be manipulated by doping. The concentration of electrons and holes is

[1] .F. Pierret. Advanced Semiconductor Fundamentals, in Modular series on solid state devices, Vol. **6**, Adison-Wesley Publishing Company, Inc., 1987.

influenced by the amount of the impurity atoms that substitute silicon atoms in the lattice. Under assumption that the semiconductor is uniformly doped and in equilibrium a simple relationship between the carrier and dopant concentrations can be established. We assume that at room temperature the dopant atoms are ionized. Inside a semiconductor the local charge density is given by:

$$\rho = q\left(p + N_D^+ - n - N_A^-\right) \tag{3.9}$$

where q is the elementary charge (q = 1.602 × 10^{-19} C). Under equilibrium conditions, in the uniformly doped semiconductor the local charge is zero, which means that the semiconductor is everywhere charge-neutral. One can write:

$$p + N_D^+ - n - N_A^- = 0 \tag{3.10}$$

As previously discussed, the thermal energy available at room temperature is sufficient to ionise almost all the dopant atoms. Under this assumption, $N_D^+ \approx N_D$ and $N_A^+ \approx N_A$, one obtains

$$p + N_D - n - N_A = 0 \tag{3.11}$$

which is the common form of the ***charge neutrality equation***.

Let's consider now an *n*-type material. At room temperature almost all donor atoms N_D are ionised and donate an electron into the conduction band. Under the assumption that $N_A = 0$, Eq. (3.11) becomes

$$p + N_D - n = 0\,. \tag{3.12}$$

Under the assumption that

$$N_D \approx N_D^+ \approx n \tag{3.13}$$

we can expect that the concentration of holes is lower than that of electrons, and becomes very low when N_D becomes very large. We can calculate more accurate the concentration of holes in the *n*-type material from Eq. (3.6).

$$p = \frac{n_i^2}{n} = \frac{n_i^2}{N_D} << n \tag{3.14}$$

In case of a *p*-type material almost all acceptor atoms N_A are ionised at room temperature and accept an electron and leaving a hole in the valence band. Under the assumption that $N_D = 0$, Eq. (3.11) becomes

$$p - n - N_A = 0\,. \tag{3.15}$$

Under the assumption that

$$N_A \approx N_A^- \approx p \tag{3.16}$$

we can expect that the concentration of electrons is lower than that of holes. We can calculate more accurate the concentration of electrons in the *p*-type material from Eq. (3.6).

$$n = \frac{n_i^2}{p} = \frac{n_i^2}{N_A} << p \tag{3.17}$$

Inserting donor and acceptor atoms into the lattice of crystalline silicon introduces allowed energy levels into the forbidden bandgap. For example, the fifth valence electron of the phosphorous atom does not take part in forming a bond, is rather weakly bound to the atom and easily liberates from the phosphorous atom. The energy of the liberated electron lies in the CB. The energy levels, which we denote E_D, of the weakly-bound valence electrons of the donor atoms have to be positioned close the CB. Notice that a dashed line represents the E_D. This means, that an electron that occupies the E_D level, is localized to the vicinity of the donor atom. Similarly, the acceptor atoms introduce allowed energy levels E_A close to the VB. Doping also influences the position of the Fermi energy. When increasing the concentration of electrons by increasing the concentration donors the Fermi energy will increase, which is represented by bringing the Fermi energy close to the CB in the band diagram. In the *p*-type material the Fermi energy is moving closer the VB. A change in the Fermi-energy position and the introduction of the allowed energy level into the bandgap due to the doping is illustrated in Figure 3.8.

The position of the Fermi level in an *n*-type semiconductor can be calculated using Eq. (3.5a) and the assumption (3.13) and in a *p*-type semiconductor using Eq. (3.5b) and Eq. (3.16), respectively.

$$E_C - E_F = kT \ln\left(N_C / N_D\right) \qquad \text{for } n\text{-type} \tag{3.18a}$$

$$E_F - E_V = kT \ln\left(N_V / N_A\right) \qquad \text{for } p\text{-type} \tag{3.18b}$$

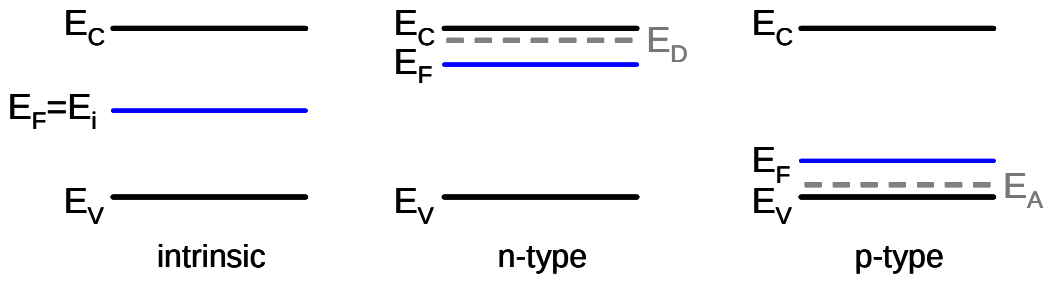

Figure 3.8. A shift of the position of the Fermi energy in the band diagram and the introduction of the allowed energy level into the bandgap due to the doping.

EXAMPLE.
This example demonstrates how much the concentration of electrons and holes can be manipulated by doping. A c-Si wafer is uniformly doped with 1×10^{17} cm^{-3} *phosphorous atoms. Phosphorous atoms act as donors and therefore at room temperature the concentration of electrons is almost equal to the concentration of donor atoms:*

$$n = N_D^+ \approx N_D = 1\times 10^{17}\ cm^{-3}.$$

The concentration of holes in the n-type material is calculated from Eq. (3.13)

$$p = n_i^2 / n = \left(1.5\times 10^{10}\right)^2 / 1\times 10^{17} = 2.25\times 10^{3}\ cm^{-3}.$$

We notice that there is a difference of 14 orders between n (1×10^{17} cm^{-3}*) and p (*2.25×10^{3} cm^{-3}*). It is now obvious why electrons are called in the n-type material the majority carriers and holes the minority carriers. We can calculate the change in the Fermi energy due to the doping. Let's assume that the reference energy level is the bottom of the conduction band,* E_c*=0 eV. Using Eq. (3.8) we calculate the Fermi energy in the intrinsic c-Si.*

$$E_i = E_C - E_G/2 + kT/2\ln\left(N_V/N_C\right) = -1.12/2 + 0.0258/2\ln\left(1.83\times 10^{19}/3.22\times 10^{19}\right) = -0.57\ \text{eV}.$$

The Fermi energy in the n-type doped c-Si wafer is calculated from Eq. (3.5a)

$$E_F = E_C + kT\ln\left(n/N_C\right) = 0.0258\ln\left(1\times 10^{17}/3.22\times 10^{19}\right) = -0.15\ \text{eV}.$$

We notice that the doping with phosphorous atoms has resulted in the shift of the Fermi energy towards the B. Note that when $n > N_C$*, the* $E_F > E_C$ *and the Fermi energy lies in the CB.*

3.2.4 Transport properties

In contrast to the equilibrium conditions, under operational conditions a net electrical current flows through a semiconductor device. The electrical currents are generated in a semiconductor due to the transport of charge from place to place by electrons and holes. The two basic transport mechanisms in a semiconductor are ***drift*** and ***diffusion***.

Drift

Drift is charged-particle motion in response to an electric field. In an electric field the force acts on the charged particles in a semiconductor, which accelerates the positively charged holes in the direction of the electric field and the negatively charged electrons in the direction opposite to the electric field. Because of collisions with the thermally vibrating lattice atoms and ionised impurity atoms, the carrier acceleration is frequently disturbed. The resulting motion of electrons and holes can be described by average drift velocities $\mathbf{v}_{dn}$ and $\mathbf{v}_{dp}$ for electrons and holes, respectively. In case of low electric fields, the average drift velocities are directly proportional to the electric field as expressed by Eqs. (3.19). The proportionality factor is called ***mobility***, μ, and is a central parameter that characterises electron and hole transport due to drift.

$$\mathbf{v}_{dn} = -\mu_n \xi \tag{3.19a}$$

$$\mathbf{v}_{dp} = \mu_p \xi \tag{3.19b}$$

Although the electrons move in the opposite direction to the electric field, because the charge of an electron is negative the resulting electron drift current is in the same direction as the electric field. This is illustrated in Figure 3.9.

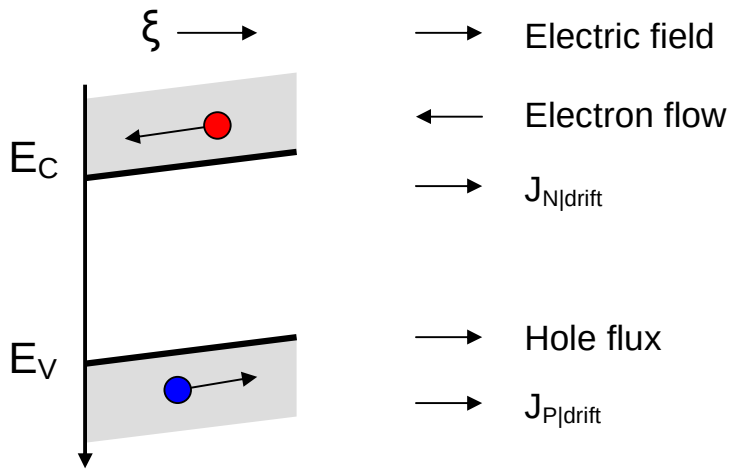

Figure 3.9. Visualization of carrier drift using the band diagram.

The electron and hole drift-current densities are defined by Eqs. (3.20) and the total drift current by Eq. (3.21).

$$\mathbf{J}_{N|drift} = -q\,n\,\mathbf{v}_{dn} = q\,n\,\mu_n\,\xi \tag{3.20a}$$

$$\mathbf{J}_{P|drift} = q\,p\,\mathbf{v}_{dp} = q\,p\,\mu_p\,\xi \tag{3.20b}$$

$$\mathbf{J}_{drift} = q\,(p\,\mu_p + n\,\mu_n)\,\xi \tag{3.21}$$

Mobility is a measure of how easily the charge particles can move through a semiconductor material. For example, at 300 K, $\mu_n \approx 1360$ cm^{2}V^{-1}s^{-1} and $\mu_p \approx 460$ cm^{2}V^{-1}s^{-1} in c-Si doped with N_D and N_A equal to 10^{14} cm^{-3}, respectively. As mentioned earlier, the motion of charged carriers is frequently disturbed by collisions. When number of collisions increases, the mobility decreases. Increasing the temperature increases the collisions of charged carriers with the vibrating lattice atoms, which results in a lower mobility. Increasing the doping concentration of donors or acceptors leads to more frequent collisions with the ionised dopant atoms, which again results in a lower mobility. The dependence of mobility on doping and temperature is in more detailed discussed in standard textbooks for semiconductor physics and devices [1,2].

Diffusion

Diffusion is a process whereby particles tend to spread out from regions of high particle concentration into regions of low particle concentration as a result of random thermal motion. A gradient in concentration of particles in a semiconductor is the driving force for the transport of particles associated with diffusion. On the contrary to the drift transport mechanism, the particles need not be charged to be involved in the diffusion process. Currents resulting from diffusion are proportional to the gradient in particle concentration and are expressed by Eqs (3.22) and the total diffusion current by Eq. (3.23). The total current due to both drift and diffusion is expressed by Eq. (3.24).

$$\mathbf{J}_{N|diff} = q\,D_N\nabla n \tag{3.22a}$$

$$\mathbf{J}_{P|diff} = -q\,D_P\nabla p \tag{3.22b}$$

$$\mathbf{J}_{diff} = q\left(D_N\nabla n - D_P\nabla p\right) \tag{3.23}$$

$$\mathbf{J} = \mathbf{J}_{drift} + \mathbf{J}_{diff} = q\,(p\,\mu_p + n\,\mu_n)\,\xi + q\left(D_N\nabla n - D_P\nabla p\right) \tag{3.24}$$

The constants of proportionality, D_N and D_P, are referred to as electron and hole ***diffusion coefficients***, respectively. The diffusion coefficients of electrons and holes are linked with the mobilities of the corresponding charge carriers by the Einstein relationship, which is expressed by Eqs. (3.25).

[2] D.A. Neaman, Semiconductor Physiscs and Devices: Basic principles, McGraw-Hill, 2003.

$$\frac{D_N}{\mu_n} = \frac{kT}{q} \tag{3.25a}$$

$$\frac{D_P}{\mu_p} = \frac{kT}{q} \tag{3.25b}$$

The visualization of the diffusion process and the resulting directions of particle fluxes and current are shown in Figure 3.10.

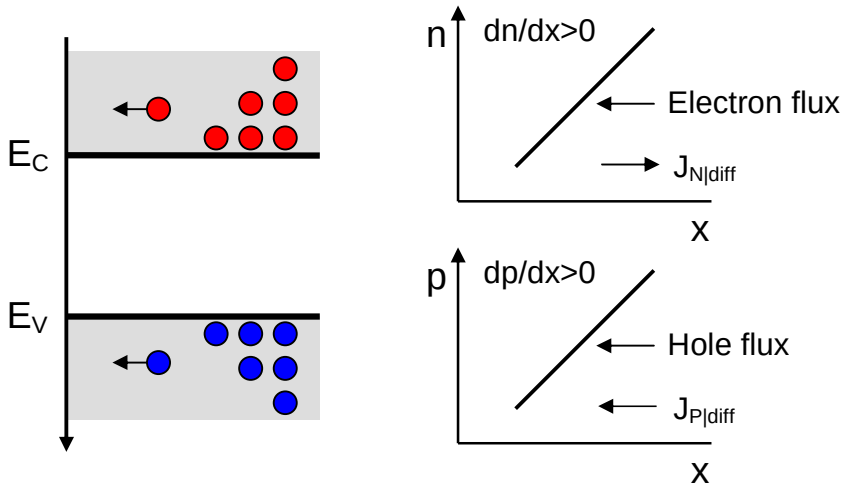

Figure 3.10. Visualization of carrier diffusion using the band diagram.

EXAMPLE. To obtain some idea about values of diffusion coefficients, let us assume Si sample at room temperature, doped with donors $N_D = 10^{14}$ cm^{-3}. According to Eq. (3.25a)

$$D_N = (kT/q)\,\mu_n = 0.0258\,\mathrm{V} \times 1360\,\mathrm{cm^2 V^{-1} s^{-1}} = 35\,\mathrm{cm^2\,s^{-1}}.$$

3.2.5 Recombination and generation

When a semiconductor is disturbed from the equilibrium state the electron and hole concentrations change from their equilibrium values. A number of processes start within the semiconductor after the perturbation in order to restore the equilibrium conditions. We call these processes recombination-generation (R-G) processes and they take care that a carrier excess or deficit is eliminated (if the perturbation is removed) or stabilized (if the perturbation is maintained). Generation is a process whereby electrons and holes are created. Recombination is a process whereby electrons and holes are annihilated or destroyed. As mentioned earlier, several processes can occur in a semiconductor, which lead to the generation or annihilation of the electrons and holes. In the following we shall describe only some of them, which are visualized in Figure 3.11.

1. **Band-to-band generation** (Figure 3.11a). The generation of an electron-hole pair can occur when the energy to break a bond is delivered by a photon (photogeneration) or by heat (direct thermal generation). This process can be visualized in terms of the band diagram as the excitation of an electron from the valence band into the conduction band.
2. **Band-to-band recombination** (Figure 3.11b). This process involves the direct annihilation of a conduction-band electron with a valence-band hole and is often called direct thermal recombination. It is typically a ***radiative*** process, in which a photon is emitted that carries an excess energy released in the recombination process.
3. **R-G center recombination or** indirect thermal recombination (Figure 3.11c). As the name suggests the annihilation or creation of electrons and holes does not occur directly but it is facilitated by a ***R-G center***. The R-G centers can be special impurity atoms or lattice defects. Their concentration is usually small compared to the acceptor or donor concentrations. The R-G centers introduce allowed energy levels (E_T) near the centre of the forbidden gap. An electron is trapped at the R-G center and consequently annihilated by a hole that is attracted by the trapped electron. Though this process seems to be less likely than the direct thermal recombination, it is at most operational conditions the dominant recombination-generation process in semiconductors. The process is typically non-radiative and the excess energy is dissipated into the lattice in form of heat.

The major effect of R-G processes in a semiconductor is to produce a change in the carrier concentration. In this way the R-G processes indirectly affects current flow in semiconductors by manipulating the concentrations of carriers that are involved in the drift and diffusion processes. The R-G processes change the carrier concentrations and this is mathematically characterized by the time rate of change in the carrier concentration ($\partial n/\partial t$ and $\partial p/\partial t$). In case of photogeneration, in which always an excess of an equal number of electrons and holes are created per second, one can write

$$\left.\frac{\partial n}{\partial t}\right|_{\text{light}} = \left.\frac{\partial p}{\partial t}\right|_{\text{light}} = G_L \qquad (3.26)$$

G_L is the generation rate due to light and its unit is (number/cm^3 s). G_L is a function of the distance in the material, depends in general on the absorption coefficient of the material, which is a function of the wavelength of light.

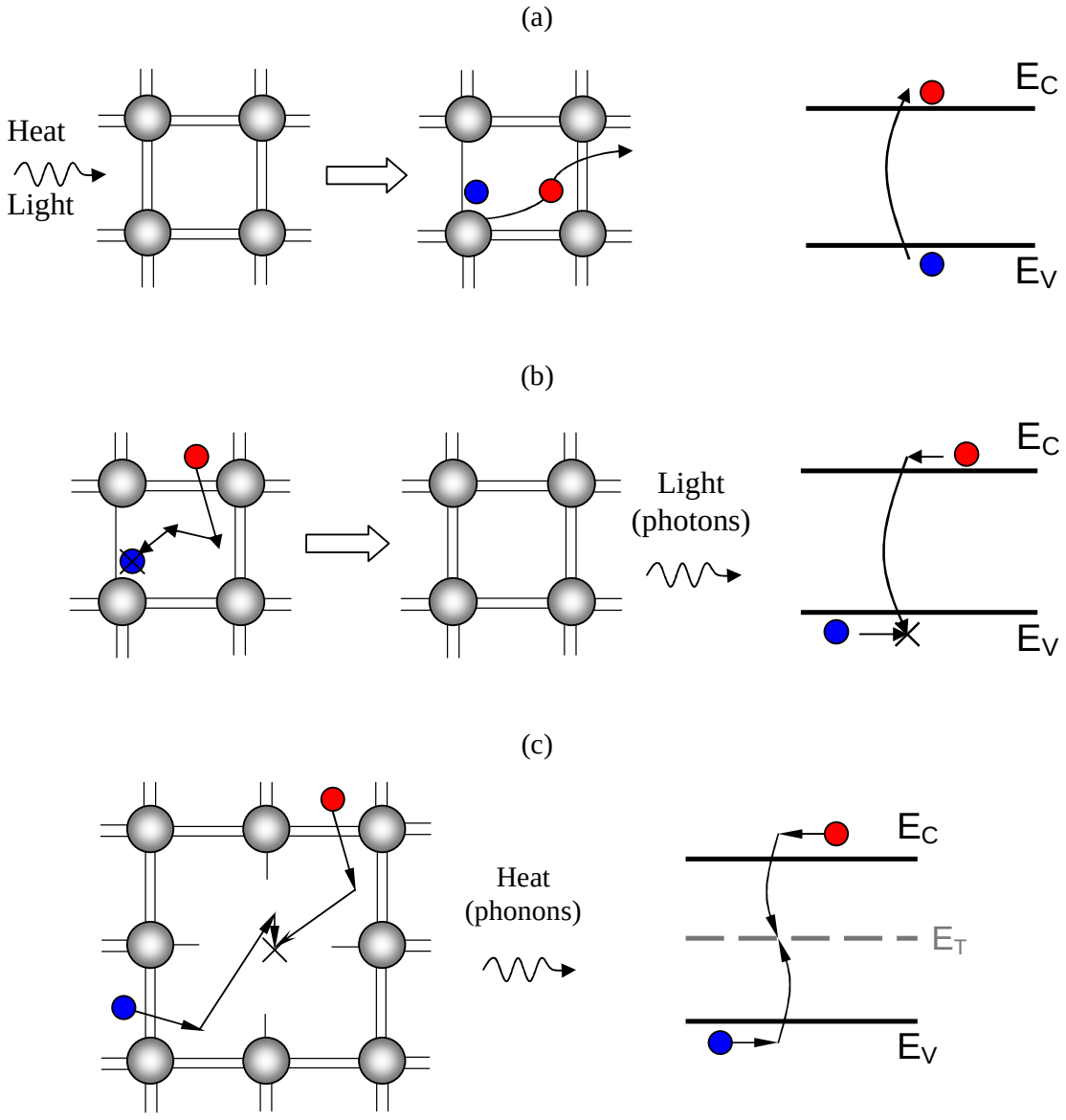

Figure 3.11. Visualization of some of the recombination-generation processes using the bonding model and the energy band diagram. (a) photogeneration and direct thermal generation, (b) direct thermal recombination, (c) R-G center (indirect thermal) recombination.

We shall introduce the equations describing the rate of change in the carrier concentration due to the dominant thermal R-G process for a semiconductor under following condition:
(1) the semiconductor is *n*- or *p*-type and
(2) the perturbation causes only ***low level injection***.

The low injection means that

$\Delta n << p_0$, $p \cong p_0$ in a *p*-type material;

$\Delta p << n_0$, $n \cong n_0$ in an *n*-type material.

In case of the dominant thermal R-G process, which is recombination-generation involving R-G centres, the time rate of change in the carrier concentration depends on the excess or deficit of electrons and holes, in respect to their equilibrium values, $\Delta n = n - n_0$ and $\Delta p = p - p_0$, respectively, and the concentration of the R-G centers, N_T.

$$\left.\frac{\partial n}{\partial t}\right|_{\substack{\text{thermal}\\ \text{R-G}}} = -c_n N_T \Delta n \qquad \text{for electrons in a } p\text{-type material} \qquad (3.27a)$$

$$\left.\frac{\partial p}{\partial t}\right|_{\substack{\text{thermal}\\ \text{R-G}}} = -c_p N_T \Delta p \qquad \text{for holes in an } n\text{-type material} \qquad (3.27b)$$

where c_n and c_p are proportionality constants and are referred to as the electron and hole capture coefficients, respectively. The minus sign is introduced in Eqs. (3.27) because $\partial n/\partial t$ and $\partial p/\partial t$ decreases (is negative) when $\Delta n > 0$ and $\Delta p > 0$. We introduce the time constants

$$\tau_n = \frac{1}{c_n N_T} \qquad (3.28a)$$

$$\tau_p = \frac{1}{c_p N_T} \qquad (3.28b)$$

which, when substituted into Eqs. (3.27), yield

$$\left.\frac{\partial n}{\partial t}\right|_{\substack{\text{thermal}\\ \text{R-G}}} = -\frac{\Delta n}{\tau_n} \qquad \text{for electrons in a } p\text{-type material} \qquad (3.29a)$$

$$\left.\frac{dp}{dt}\right|_{\substack{\text{thermal}\\ \text{R-G}}} = -\frac{\Delta p}{\tau_p} \qquad \text{for holes in an } n\text{-type material} \qquad (3.29b)$$

The time constants τ_n and τ_p are the central parameters associated with recombination-generation. They can be interpreted as the *average time* an excess minority carrier will survive among majority carriers. The time constants τ_n and τ_p are referred to as ***minority-carrier lifetimes***. The values of the minority-carrier lifetimes can vary a lot. When the R-G center concentration is reduced to a very low level in c-Si, a τ_n (τ_p) can achieve ~ 1 ms. On the other hand, the intentional introduction of gold atoms into Si, which introduce efficient R-G centers into Si, can decrease a τ_n (τ_p) to ~ 1 ns. Typical minority-carrier lifetimes in most c-Si devices are usually ~ 1 μs. For an efficient collection of photo-generated carriers in c-Si solar cells the minority carrier lifetimes should be in range of tens of milliseconds.

When an excess of generated carriers is not uniform throughout a semiconductor, diffusion of the excess carriers takes place. The excess carriers will diffuse in the semiconductor till they do not recombine. We define the average distance that the minority carriers can diffuse among majority carries before being annihilated as ***minority-carrier-diffusion length***. The minority-carrier-diffusion lengths are defined as:

$L_N = \sqrt{D_N \tau_n}$ for electrons in a *p*-type material (3.30a)

$L_P = \sqrt{D_P \tau_p}$ for holes in an *n*-type material (3.30b)

EXAMPLE. To get an idea about the diffusion lengths, let us assume room temperature, mobility of electrons in a p-type c-Si wafer to be $\mu_n \approx 1250\ cm^2V^{-1}s^{-1}$*, which corresponds to doping of* $N_A = 10^{14}\ cm^{-3}$*, and* $\tau_n = 10^{-6}$ *s. For the given conditions, the electron diffusion length in the p-type c-Si can be calculated from Eq. (3.30a).*

$$L_N = \sqrt{D_N \tau_n} = \sqrt{(kT/q)\mu_n \tau_n} = \sqrt{0.02586\,\mathrm{V}\times 1250\,\mathrm{cm^2V^{-1}s^{-1}}\times 10^{-6}\,\mathrm{s}} = 5.7\times 10^{-3}\ \mathrm{cm} = 57\,\mu\mathrm{m}.$$

3.2.6 Optical properties

Absorption of light in a semiconductor material represents a complex interaction of light with the semiconductor atomic structure. Only such interactions that lead to the generation of free charge carriers in a semiconductor, electrons and holes, contribute to the transformation of energy carried by light into electrical energy. The generation of charge carriers is a result of breaking of the atomic bonds, when the electron-hole pairs are created. The process of generating an electron-hole pair can be visualized in the energy band diagram as transferring an electron from the valence energy band to the conduction energy band. The light particles, photons, have to carry at least the energy equal to the ***band gap energy*** of a semiconductor in order to free an electron from a covalent bond. Photons with energy higher than the band gap energy generate electron-hole pairs. Since the electrons and holes tend to occupy energy levels at the bottom of the conduction band and the top of the valence band, respectively, the extra energy that the electron-hole pairs receive from the photons is released as heat into the semiconductor lattice in the ***thermalization*** process. The process of creation of an electron-hole pair by absorbing a photon and the process of thermalization are illustrated in Figure 3.12.

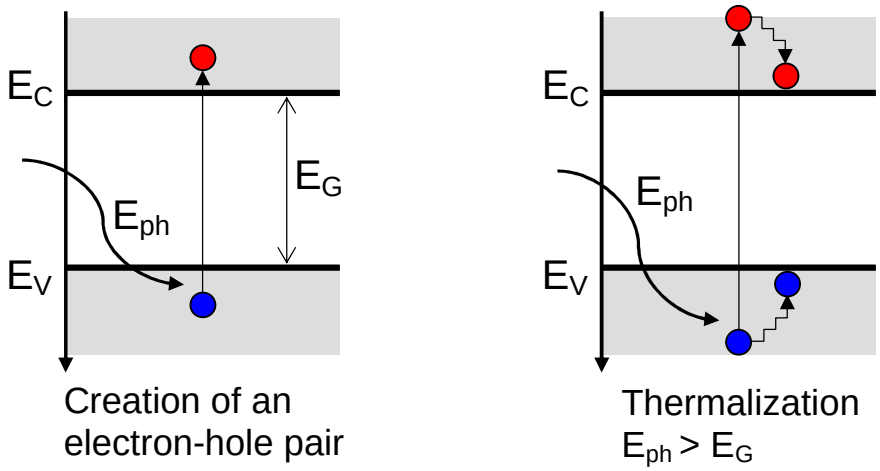

Figure 3.12. Visualization of the process of creation of an electron-hole pair by absorbing a photon and the process of thermalization using the energy band diagram.

An important key for obtaining an efficient solar cell is to minimize the heat losses due to the thermalization by choosing semiconductors with appropriate band gaps. When taking into account the energy distribution of the solar spectrum the most effective materials for solar energy conversion have band gap energies in the range of 1.0 to 1.8 eV (electron-volts).

The photon energy, E_{ph}, depends on the wavelength of light and is calculated using the following formula:

$$E_{ph} = hc/\lambda \qquad (3.31)$$

where h is the Planck constant ($h = 6.625 \times 10^{-34}$ Js) , c is the speed of light ($c = 2.998 \times 10^{8}$ ms^{-1}), and λ is the wavelength of light. The entire spectrum of sunlight, from infrared to ultraviolet, covers a range of about 0.5 eV to about 4.0 eV. About 55% of the energy of sunlight cannot be used by most solar cells because this energy is either lower than the band gap or it is higher and the excess energy is lost by thermalization.

While the band gap energy of a semiconductor provides us with information, which part of the solar spectrum is absorbed, the ***complex refractive index***, $\tilde{n} = n - ik$, describes how efficient the photons of a particular energy are absorbed in the material. The real part n is called the refractive index, and the imaginary part k is called the extinction coefficient. The extinction coefficient is related to the absorption coefficient α by:

$$k = \frac{\alpha \lambda}{4\pi} \tag{3.32}$$

The n and k are called ***optical constants***, although they are functions of the wavelength of light or the photon energy. The wavelength, λ is related to the photon energy, $h\nu$ as,

$$h\nu = \frac{h}{q}\frac{c}{\lambda} \tag{3.33}$$

where the photon energy is represented in eV.

When light impinges on an interface between two media that are characterized by their complex refractive indices, a part of the light is reflected from and the other part is transmitted through the interface. The interface is therefore characterized by the reflectance and transmittance. Reflectance is the ratio of the energy reflected from the surface of the interface to the total incident energy. Transmittance is the ratio of the energy transmitted through the interface to the total incident energy.

When light arrives at the optical interface at normal incidence, the reflectance and transmittance can be calculated by using the amplitude reflection and transmission coefficients also known as Fresnel amplitude coefficients ($\tilde{r}$, $\tilde{t}$) [3][3]:

$$\tilde{r} = \frac{\tilde{n}_0 - \tilde{n}_1}{\tilde{n}_0 + \tilde{n}_1} \tag{3.34}$$

$$\tilde{t} = \frac{2\tilde{n}_0}{\tilde{n}_0 + \tilde{n}_1} \tag{3.35}$$

The $\tilde{n}_0$ and $\tilde{n}_1$ are the complex refractive indices of the first and second medium. The Fresnel amplitude coefficients are also complex numbers. The reflectance and transmittance of the interface are:

[3] J.M. Bennett and H.E. Bennett, *Polarization.* in Handbook of Optics, eds. W.G. Driscoll and W. Vaughan, Chap. 10, Mc Graw-Hill, 1978.

$$R = |\tilde{r}|^2 = \left|\frac{\tilde{n}_0 - \tilde{n}_1}{\tilde{n}_0 + \tilde{n}_1}\right|^2 \tag{3.36}$$

$$T = \left|\frac{\tilde{n}_1}{\tilde{n}_0}\right| |\tilde{t}|^2 = \frac{4\,|\tilde{n}_0\ \tilde{n}_1|}{|\tilde{n}_0 + \tilde{n}_1|^2} \tag{3.37}$$

When light penetrates into a material it will be absorbed as it propagates through the material. The absorption profile in the material depends on the absorption coefficient of the material, which is wavelength dependent. The most frequent approach to calculate the absorption profile of photons in semiconductor devices is by using the Lambert-Beer absorption formula. The Lambert-Beer formula states that a photon flux density after passing a distance *x* in a film with absorption coefficient $\alpha(\lambda)$ is reduced with a factor $e^{-\alpha(\lambda)x}$,

$$\Phi(x,\lambda) = \Phi^0(\lambda)\exp(-\alpha(\lambda)x), \tag{3.38}$$

where $\Phi^0(\lambda)$ is the incident photon flux density. The photon flux density is the number of photons per unit area per unit time and per unit wavelength. It is related to the spectral power density $P(\lambda)$ associated with the solar radiation by:

$$\Phi^0(\lambda) = P(\lambda)\frac{\lambda}{hc} \tag{3.39}$$

The spectral generation rate $g_{sp}(x,\lambda)$, which is the number of electron-hole pairs generated at a depth *x* in the film per second per unit volume per unit wavelength, by photons of wavelength λ, is calculated according to the following formula, on the assumption of zero reflection:

$$g_{sp}(x,\lambda) = \eta_g \Phi^0(\lambda)\,\alpha(\lambda)\,e^{-\alpha(\lambda)x} \tag{3.40}$$

where η_g is the generation quantum efficiency, usually assumed to equal unity. This assumption means that every photon generates one and only one electron-hole pair. The optical generation rate $G_L(x)$ is calculated from the spectral generation rate by integrating over a desired wavelength spectrum:

$$G_L(x) = \int_{\lambda_1}^{\lambda_2} g_{sp}(x,\lambda)\,d\lambda \tag{3.41}$$

The optical generation rate is related to the absorption profile, *A*(*x*), in the film:

$$G_L(x) = \eta_g\, A(x) \tag{3.42}$$

$$A(x) = \int_{\lambda_1}^{\lambda_2} \Phi^0(\lambda)\,\alpha(\lambda)\,e^{-\alpha(\lambda)x}\,d\lambda \tag{3.43}$$

EXAMPLE.
Let's calculate how much light is reflected from the air/c-Si interface. Lets assume that the incident light has a wavelength of 500 nm. For this wavelength the complex refractive index of air is $\tilde{n}_0 = 1.0 - 0.0\,i$ and for c-Si $\tilde{n}_1 = 4.293 - 0.045\,i$. The reflectance is calculated from Eq. 3.36.

$$R = \left|\frac{\tilde{n}_0 - \tilde{n}_1}{\tilde{n}_0 + \tilde{n}_1}\right|^2 = \left|\frac{1.0 - 0.0i - (4.293 - 0.045i)}{1.0 - 0.0i + 4.239 - 0.045i}\right|^2 = \left|\frac{-3.293 - 0.045i}{5.293 - 0.045i}\right|^2 = 0.38.$$

It means 38% of light with the wavelength of 500 nm is reflected from the air/c-Si interface. In case of c-Si solar cells, over 30% of the incident light in the range of interest is reflected. In order to make solar cells with a high conversion efficiency, antireflection coatings are used to reduce the reflection from c-Si solar cells.

EXAMPLE.
Let's calculate the total absorption in a 300 μm thick c-Si wafer for light characterised by wavelength of 500 nm. The optical constants of c-Si for light with 500 nm are: refractive index is n = 4.293, extinction coefficient k = 0.045 and absorption coefficient $\alpha = 1.11 \times 10^4\ cm^{-1}$. The incident irradiance is 1000 W/m^2.

First we calculate the photon flux density at 500 nm corresponding to the irradiance of 1000 W/m^2. Using the Eq. 3.38 we obtain

$$\Phi^0 = P \times (\lambda / hc) = 1000\,\mathrm{W m^{-2}} \times 500 \times 10^{-9}\,\mathrm{m} / \left(6.625 \times 10^{-34}\,\mathrm{Js} \times 2.998 \times 10^{8}\,\mathrm{ms^{-1}}\right) = 2.5 \times 10^{21}\,\mathrm{m^{-2}s^{-1}}.$$

From Eq. 3.36 we calculate how many incident photons are reflected from the surface

$$R = \left|\frac{\tilde{n}_0 - \tilde{n}_1}{\tilde{n}_0 + \tilde{n}_1}\right|^2 = \left|\frac{1.0 - 0.0i - (4.293 - 0.045i)}{1.0 - 0.0i + 4.239 - 0.045i}\right|^2 = \left|\frac{-3.293 - 0.045i}{5.293 - 0.045i}\right|^2 = 0.38$$

Using Lambert-Beer formula (Eq. (3.38)) we calculate the photon flux density at the backside of the wafer, it means at the distance 300 μm from the surface. We take the reflected light into account by adapting Eq. (3.38).

$$\Phi(x) = \Phi^0 (1 - R) \exp(-\alpha x) = 2.5 \times 10^{21}\,\mathrm{m^{-2}s^{-1}} \times (1 - 0.38) \exp\left(-1.11 \times 10^{6}\ \mathrm{m^{-1}} \times 300 \times 10^{-6}\,\mathrm{m}\right) \simeq 0$$

The total absorption in the wafer is the difference between the photon flux density at the surface after reflection and the photon flux density at the back of the wafer.

$$A = \Delta\Phi = \Phi^0 (1 - R) - \Phi(x) = 2.5 \times 10^{21}\,\mathrm{m^{-2}s^{-1}} \times (1 - 0.38) - 0 = 1.55 \times 10^{21}\,\mathrm{m^{-2}s^{-1}}$$

When we assume that all the absorbed photons generate one electron-hole pair (η_g=1), we can calculate how large photocurrent density corresponds to the absorbed photons.

$$J_{ph} = qA = 1.602 \times 10^{-19}\,\mathrm{C} \times 1.55 \times 10^{21}\,\mathrm{m^{-2}s^{-1}} = 248.31\,\mathrm{C\,m^{-2}s^{-1}} = 248.31\,\mathrm{A\,m^{-2}}$$

3.2.7 Carrier concentrations in non-equilibrium

When a semiconductor is illuminated additional electrons and holes are generated in the material by the absorption of photons. The photo-generated carriers interact with the semiconductor lattice. The extra energy that the electron-hole pairs receive from the photons that have energy larger than the band gap of the semiconductor is released into the lattice in form of heat. After this so called ***thermalization*** process, which is very fast and takes approximately 10^{-12} s, the carrier concentrations achieve a steady-state. In this non-equilibrium state the electron and hole concentrations are different than those in the equilibrium state. In non-equilibrium states two Fermi distributions are used to describe the electron and hole concentrations. One Fermi distribution with the ***quasi-Fermi energy for electrons***, E_{FC}, describes the occupation of states in the conduction band with electrons. Another Fermi distribution with the ***quasi-Fermi energy for holes***, E_{FV}, describes the occupation of states in the valence band with electrons, and therefore determines also the concentration of holes. Using the band diagram with the quasi-Fermi levels the process of creation of electron-hole pairs and their subsequent thermalization that describe the carrier concentration under illumination is illustrated in Figure 3.13. The difference between the quasi-Fermi levels is the electrochemical energy, μ_{eh}, of the generated electron-hole pairs which represents the measure for the conversion efficiency of solar radiation.

The density of electrons and holes under non-equilibrium conditions is described by

$$n = N_C \exp\left[\left(E_{FC} - E_C\right)/kT\right] \tag{3.44a}$$

$$p = N_V \exp\left[\left(E_V - E_{FP}\right)/kT\right] \tag{3.44b}$$

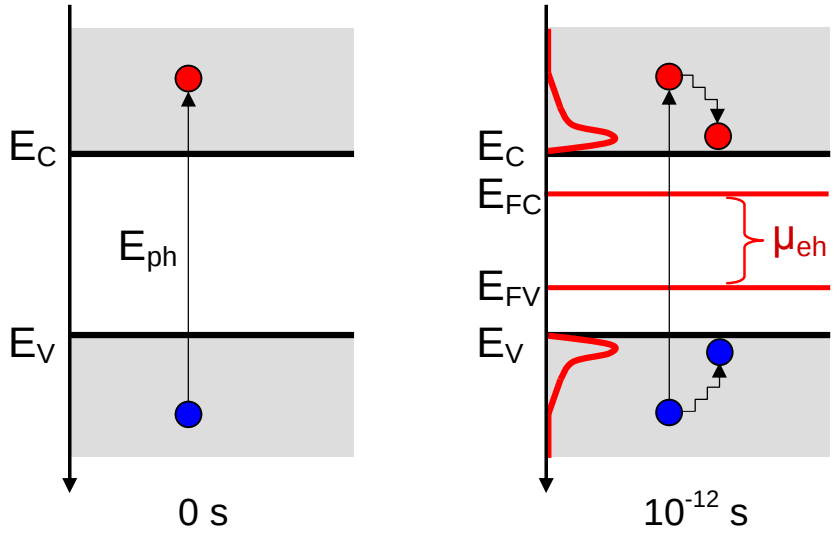

Figure 3.13. Thermalization photo-generated electron-hole pairs resulting in non-equilibrium charge-carrier concentrations described by the quasi-Fermi levels.

It then follows that under non-equilibrium conditions

$$n\,p = N_C\,N_V \exp\left[\frac{E_V - E_C}{kT}\right]\exp\left[\frac{E_{FC} - E_{FP}}{kT}\right] = n_i^2 \exp\left[\frac{E_{FC} - E_{FP}}{kT}\right] \tag{3.45}$$

By using the quasi-Fermi level formalism for describing the concentration of charge carriers in non-equilibrium conditions the electron and hole current densities inside a semiconductor, $\mathbf{J}_N$ and $\mathbf{J}_P$, can be expressed by following equations:

$$\mathbf{J_N} = n\mu_n \nabla E_{FC} \tag{3.46a}$$

$$\mathbf{J_P} = p\mu_p \nabla E_{FV} \tag{3.46b}$$

One can notice from Eq. (3.46) that when a quasi-Fermi level varies with position ($dE_{FC}/dx \neq 0$ or $dE_{FV}/dx \neq 0$) the current is flowing inside the semiconductor. By checking the position dependence of the quasi-Fermi levels in an energy band diagram, one can easily determine whether current flows inside the semiconductor.

3.3 Basic equations of device physics

In the previous section, semiconductor material properties and the carrier transport, creation and annihilation taking place inside a semiconductor were discussed and described. The results from the drift, diffusion, and recombination-generation analysis are put together into a set of equations, which form a general three-dimensional mathematical model for semiconductor device operation.

3.3.1 Continuity Equations

Drift, diffusion, and recombination-generation processes give rise to a change in the carrier concentrations in time. Nevertheless, there must be a spatial and time continuity in the carrier concentrations. The combined effect of all types of carrier action within a semiconductor is described by the following continuity equation for electrons (Eq. (3. 47a) and holes (Eq. (3.47b), respectively

$$\frac{\partial n}{\partial t} = \left.\frac{\partial n}{\partial t}\right|_{\text{drift}} + \left.\frac{\partial n}{\partial t}\right|_{\text{diff}} + \left.\frac{\partial n}{\partial t}\right|_{\substack{\text{thermal}\\ \text{R-G}}} + \left.\frac{\partial n}{\partial t}\right|_{\substack{\text{other processes}\\ \text{(photogeneration)}}} \tag{3.47a}$$

$$\frac{\partial p}{\partial t} = \left.\frac{\partial p}{\partial t}\right|_{\text{drift}} + \left.\frac{\partial p}{\partial t}\right|_{\text{diff}} + \left.\frac{\partial p}{\partial t}\right|_{\substack{\text{thermal}\\ \text{R-G}}} + \left.\frac{\partial p}{\partial t}\right|_{\substack{\text{other processes}\\ \text{(photogeneration)}}} \tag{3.47b}$$

The continuity equations can be written in a more compact form when introducing substitutions

$$\left.\frac{\partial n}{\partial t}\right|_{\substack{\text{thermal}\\ \text{R-G}}} = -R_N ; \qquad \left.\frac{dp}{dt}\right|_{\substack{\text{thermal}\\ \text{R-G}}} = -R_P \tag{3.48a,b}$$

$$\left.\frac{\partial n}{\partial t}\right|_{\text{other processes}} = G_N ; \qquad \left.\frac{\partial p}{\partial t}\right|_{\text{other processes}} = G_P \tag{3.49a,b}$$

and noting

$$\left.\frac{\partial n}{\partial t}\right|_{\text{drift}} + \left.\frac{\partial n}{\partial t}\right|_{\text{diff}} = \frac{1}{q}\nabla \cdot \mathbf{J}_{\text{N}} \tag{3.50a}$$

$$\left.\frac{\partial p}{\partial t}\right|_{\text{drift}} + \left.\frac{\partial p}{\partial t}\right|_{\text{diff}} = -\frac{1}{q}\nabla \cdot \mathbf{J}_{\text{P}} \tag{3.50b}$$

In these equations $\partial n/\partial t$ ($\partial p/\partial t$) is the time rate change in the electron (hole) concentration, $\mathbf{J}_{\text{N}}$ ($\mathbf{J}_{\text{P}}$) is the electron (hole) current density, R_N (R_P) denotes the net recombination-generation rate of electrons (holes), G_N (G_P) is the generation rate of electrons (holes) due to other processes, such as photogeneration. Substituting Eqs. (3.48) through (3.50) into (3.47), we obtain

$$\frac{\partial n}{\partial t} = \frac{1}{q}\nabla \cdot \mathbf{J_N} - R_N + G_N \tag{3.51a}$$

$$\frac{\partial p}{\partial t} = -\frac{1}{q}\nabla \cdot \mathbf{J_P} - R_P + G_P \tag{3.51b}$$

3.3.2 Current-Density Equations

The electron and hole current densities inside a semiconductor, $\mathbf{J}_{\text{N}}$ and $\mathbf{J}_{\text{P}}$, are obtained by adding the current densities due to drift and diffusion.

$$\mathbf{J}_{\text{N}} = q\, n\, \mu_n\, \boldsymbol{\xi} + q\, D_N \nabla n \tag{3.52a}$$

$$\mathbf{J}_{\text{P}} = q\, p\, \mu_p\, \boldsymbol{\xi} - q\, D_p \nabla p \tag{3.52b}$$

3.3.3 Poisson's Equation

The Poisson's equation (3.53) relates the divergence of the electric field to the space charge density, ρ.

$$\nabla \cdot \boldsymbol{\xi} = \frac{\rho}{\varepsilon_r \varepsilon_0} \tag{3.53}$$

In this equation ε_r is the semiconductor dielectric constant and ε_0 is the permittivity of the vacuum. The permittivity of the vacuum ε_0 = 8.854x10^{-14} F/cm and for c-Si ε_r = 11.7. Free electrons, holes and ionised dopant atoms are the main contributors to the charge density inside a semiconductor. It has been mentioned that impurities other than dopants and defects can be present in a semiconductor and act as charge capture centres. However, the concentration of such imperfections is kept small in semiconductors used for solar cells. The space charge density is therefore sufficiently described by Eq. (3.9):

$$\rho = q\left(p + N_D^+ - n - N_A^-\right).$$

3.3.4 Equations summary

Since the operation of a solar cell can be sufficiently described by processes taking place in one direction, the set of basic semiconductor equations will be given in one-dimensional form.

$$\left.\begin{aligned}
&\frac{d\xi}{dx} = \frac{\rho}{\varepsilon_r \varepsilon_0} \\
&J_N = q\,n\,\mu_n\,\xi + q\,D_N\,\frac{dn}{dx} \\
&J_P = q\,p\,\mu_p\,\xi - q\,D_P\,\frac{dp}{dx} \\
&\frac{\partial n}{\partial t} = \frac{1}{q}\frac{dJ_N}{dx} - R_N + G_N \\
&\frac{\partial p}{\partial t} = -\frac{1}{q}\frac{dJ_P}{dx} - R_P + G_P
\end{aligned}\right\} \qquad (3.54)$$

Chapter 4.

SOLAR CELL OPERATIONAL PRINCIPLES

4.1 Basic operational principles

The working principle of all today solar cells is essentially the same. It is based on the ***photovoltaic effect***. In general, the photovoltaic effect means the generation of a potential difference at the junction of two different materials in response to visible or other radiation. The basic processes behind the photovoltaic effect are:

1. generation of the charge carriers due to the absorption of photons in the materials that form a junction,
2. subsequent separation of the photo-generated charge carriers in the junction,
3. collection of the photo-generated charge carriers at the terminals of the junction.

In general, a solar cell structure consists of an absorber layer, in which the photons of incident radiation are efficiently absorbed resulting in the creation of electron-hole pairs. In order to separate the photo-generated electrons and holes from each other, the so-called "semi-permeable membranes" are attached to the both sides of the absorber[1]. The important requirement for the semi-permeable membranes is that they selectively allow only one type of charge carrier to pass through. An important issue for designing an efficient solar cell is that the electrons and holes generated in the absorber layer reach the membranes. This requires

[1] P. Würfel, Physics of Solar Cells: From Principles to New Concepts, Wiley-WCH, Weinheim, 2005.

that the thickness of the absorber layer is smaller than the diffusion lengths of the charge carriers.

A membrane that let electrons go through and blocks holes is a material, which has a large conductivity for electrons and a small conductivity of holes. An example of such a material is an *n*-type semiconductor, in which a large electron conductivity with respect to the hole conductivity is caused namely by a large difference in electron and hole concentrations. Electrons can easily flow through the *n*-type semiconductor while the transport of holes, which are the minority carriers in such material, is due to the recombination processes very limited. The opposite holds for electrons in a *p*-type semiconductor, which is an example of the hole membrane.

In order to minimize the injection of holes from the absorber into the *n*-type semiconductor an energy barrier should be introduced in the valence band, ΔE_V, between the *n*-type semiconductor and the absorber. Ideally, this can be achieved by choosing an *n*-type semiconductor that has a larger band gap than that of the absorber and the energy difference is located in the valence band of the two materials. Similarly, the injection of electrons from the absorber into the *p*-type semiconductor could be suppressed by using a *p*-type semiconductor with a larger band gap than that of the absorber and having the band off-set in the conduction band, ΔE_C, between the absorber and the *p*-type semiconductor. The requirement of having the band off-set in the conduction band means that the electron affinity, χ_e, of the *p*-type semiconductor is smaller that the electron affinity of the absorber. The additional advantage applying membrane materials with large band gaps is to allow almost all photons to be transmitted and absorbed into the absorber.

The asymmetry in the electronic structure of the *n*-type and *p*-type semiconductors is the basic requirement for the photovoltaic energy conversion. Figure 4.1 shows a schematic band diagram of an illuminated idealized solar cell structure with an absorber and the semi-permeable membranes. The terminals or in other words electrodes of the solar cell are attached to the membranes. We refer to the structure between the terminals as a ***junction*** and the above described solar cell structure is denoted as a ***single junction solar cell***. The quasi-Fermi level for electrons, E_{FC}, and the quasi-Fermi level for holes, E_{FV}, are used to describe the illuminated state of the solar cell. The energy difference between the quasi-Fermi levels is a measure of efficient conversion of energy of radiation into electrochemical energy. The illuminated solar cell is shown in Figure 4.1 at two conditions. The first is at the ***open-circuit*** condition, when the terminals of the solar cell are not connected to each other and therefore no electric current can flow through an external circuit. At this condition, a voltage difference can be measured between the terminals of the solar cell. This voltage is denoted the ***open-circuit voltage***, V_{oc}, and it is an important parameter that characterizes the performance of solar cells. Figure 4.1b shows the band diagram of the solar cell in the ***short-circuit*** condition. In this case the terminals of the solar cell are short circuited and a current flows through the external circuit. This current is denoted as the ***short-circuit current***, I_{sc}. The I_{sc} is also an important parameter that characterizes the performance of solar cells.

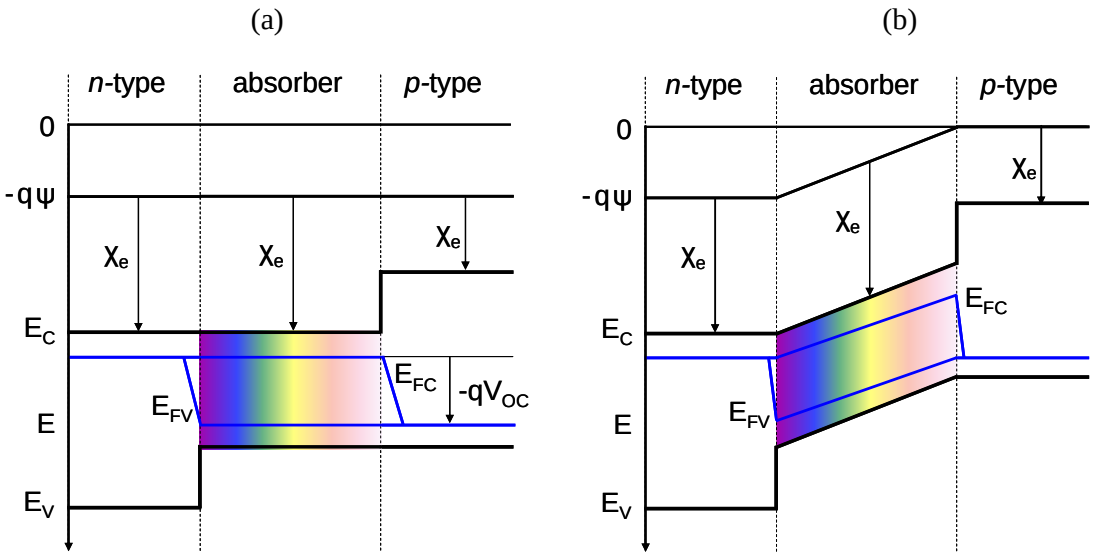

Figure 4.1. Band diagram of an idealized solar cell structure at the a) open-circuit and b) short-circuit conditions.

4.2 The *p-n* junction

At present, the most frequent example of the above-described solar cell structure is realized with crystalline silicon (c-Si). A typical c-Si solar cell structure is shown in Figure 3.1. A moderately-doped *p*-type c-Si with an acceptor concentration of 10^{16} cm^{-3} is used as the absorber. On the top side of the absorber a thin, less than 1 μm thick, highly-doped *n*-type layer is formed as the electron membrane. On the back side of the absorber a highly-doped *p*-type serves as the hole membrane. At the interfaces between the c-Si *p*-type absorber and the highly-doped *n*-type and *p*-type membranes, regions are formed with an internal electric field. These regions are especially important for solar cells and are known as ***p-n* junctions**. The presence of the internal electric field in the solar cell facilitates the separation of the photo-generated electron-hole pairs. When the charge carriers are not separated from each other in a relatively short time they will be annihilated in a process that is called recombination and thus will not contribute to the energy conversion. The easiest way to separate charge carriers is to place them in an electric field. In the electric field the carriers having opposite charge are drifted from each other in opposite directions and can reach the electrodes of the solar cell. The electrodes are the metal contacts that are attached to the membranes.

The *p-n* junction fabricated in the same semiconductor material such as c-Si is an example of the *p-n* homojunction. There are also other types of a junction that result in the formation of the internal electric field in the junction. The *p-n* junction that is formed by two chemically different semiconductors is called the *p-n* heterojunction. In the *p-i-n* junctions, the region of the internal electric field is extended by inserting an intrinsic, *i*, layer between the *p*-type and the *n*-type layers. The *i*-layer behaves like a capacitor and it stretches the electric field formed by the *p-n* junction across itself. Another type of the junction is a junction between a metal and a semiconductor, MS junction. The Schottky barrier formed at the metal-semiconductor interface is a typical example of the MS junction.

4.2.1 Formation of a space-charge region in the *p-n* junction

Figure 4.2 shows schematically isolated pieces of a *p*-type and an *n*-type semiconductor and their corresponding band diagrams. In both isolated pieces the charge neutrality is maintained. In the *n*-type semiconductor the large concentration of negatively-charged free electrons is compensated by positively-charged ionized donor atoms. In the *p*-type semiconductor holes are the majority carriers and the positive charge of holes is compensated by negatively-charged ionized acceptor atoms. For the isolated *n*-type semiconductor we can write:

$$n = n_{n0} \approx N_D \tag{4.1a}$$

$$p = p_{n0} \approx n_i^2 / N_D \,. \tag{4.1b}$$

For the isolated *p*-type semiconductor

$$p = p_{p0} \approx N_A \tag{4.2a}$$

$$n = n_{p0} \approx n_i^2 / N_A \,. \tag{4.2b}$$

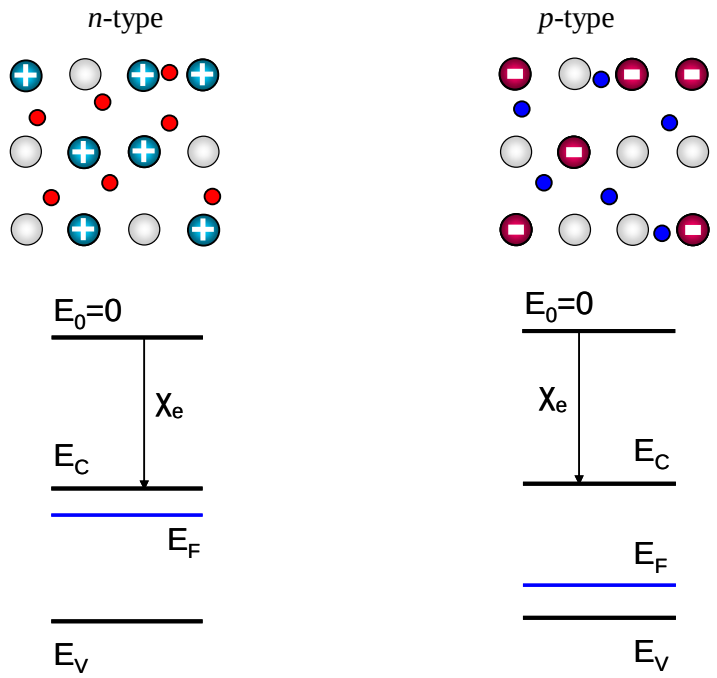

Figure 4.2. Schematic representation of an isolated *p*-type and *n*-type semiconductor and corresponding band diagrams.

When a *p*-type and an *n*-type semiconductor are brought together, a very large difference in electron concentration between *n*- and *p*-type semiconductors causes a diffusion current of electrons from the *n*-type material across the metallurgical junction into the *p*-type material. Similarly, the difference in hole concentration causes a diffusion current of holes from the *p*- to the *n*-type material. Due to this diffusion process the region close to the metallurgical junction becomes almost completely depleted of mobile charge carriers. The gradual depletion of the charge carriers gives rise to a space charge created by the charge of the ionized donor and acceptor atoms that is not compensated by the mobile charges any more. This region of the space charge is called the ***space-charge region*** or ***depleted region*** and is schematically illustrated in Figure 4.3. Regions outside the depletion region, in which the charge neutrality is conserved, are denoted as the ***quasi-neutral regions***.

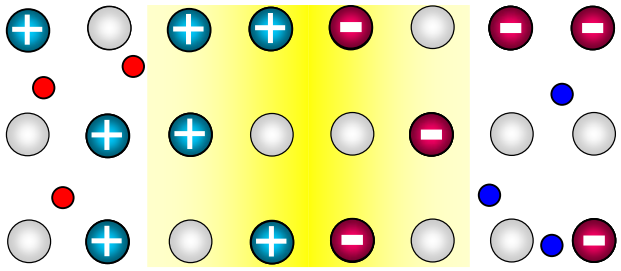

Figure 4.3. Formation of a space-charge region, when *n*-type and *p*-type semiconductors are brought together to form a junction. The colored part represents the space-charge region.

The space charge around the metallurgical junction results in the formation of an internal electric field which forces the charge carriers to move in the opposite direction than the concentration gradient. The diffusion currents continue to flow until the forces acting on the charge carriers, namely the concentration gradient and the internal electrical field, compensate each other. The driving force for the charge transport does not exist any more and no net current flows through the *p-n* junction.

4.2.2 *p-n* junction under equilibrium

The *p-n* junction represents a system of charged particles in diffusive equilibrium in which the electrochemical potential is constant and independent of position. The electrochemical potential describes an average energy of electrons and is represented by the Fermi energy. It means that under equilibrium conditions the Fermi level has constant position in the band diagram of the *p-n* junction. Figure 4.4 shows the energy-band diagram of a *p-n* junction under equilibrium. The distance between the Fermi level and the valence and/or conduction bands does not change in the quasi-neutral regions and is the same as in the isolated *n*- and *p*-type semiconductors. Inside the space-charge region, the conduction and valence bands are not represented by straight horizontal lines any more but they are curved. This indicates the presence of an electric field in this region. Due to the electric field a difference in the electrostatic potential is created between the boundaries of the space-charge region. Across the depletion region the changes in the carriers concentration are compensated by changes in the electrostatic potential. The electrostatic-potential profile is included in Figure 4.4.

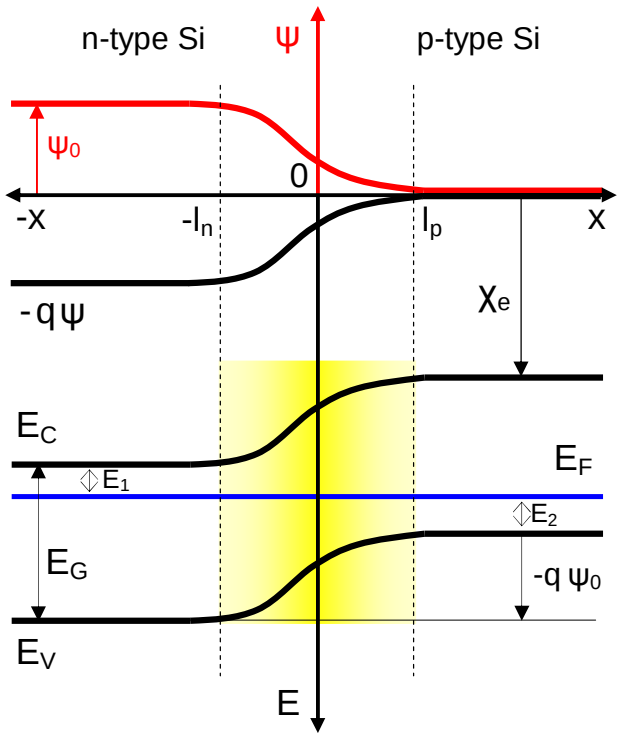

Figure 4.4. Energy-band diagram of the p-n junction. The electrostatic potential profile (red curve) is also presented in the figure.

The concentration profile of charge carriers in a *p*-*n* junction is schematically presented in Figure 4.5. In the quasi-neutral regions the concentration of electrons and holes is the same as in the isolated doped semiconductors. In the space-charge region the concentrations of majority charge carriers decrease very rapidly. This fact allows us to use the assumption that the space-charge region is depleted of mobile charge carriers. This assumption means that the charge of the mobile carriers represents a negligible contribution to the total space charge in the depletion region. The space charge in this region is fully determined by the ionized dopant atoms fixed in the lattice.

The presence of the internal electric field inside the *p*-*n* junction means that there is an electrostatic potential difference, ψ_0, across the space-charge region. We shall determine a profile of the internal electric field and electrostatic potential in the *p*-*n* junction. First we introduce an approximation, which simplifies the calculation of the electric field and electrostatic-potential. This approximation (*the depletion approximation*) assumes that the space-charge density, ρ, is zero in the quasi-neutral regions and it is fully determined by the concentration of ionized dopants in the depletion region. In the depletion region of the *n*-type semiconductor it is the concentration of positively charged donor atoms, N_D, which determines the space charge in this region. In the *p*-type semiconductor, the concentration of negatively charged acceptor atoms, N_A, determines the space charge in the depletion region. This is illustrated in Figure 4.6. Further, we assume that the *p*-*n* junction is a step junction; it means that there is an abrupt change in doping at the metallurgical junction and the doping concentration is uniform both in the *p*-type and the *n*-type semiconductors.

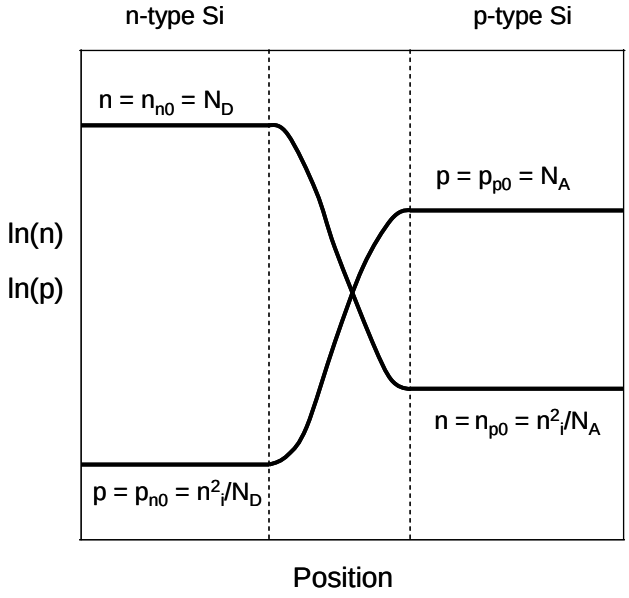

Figure 4.5. Concentrations profile of mobile charge carriers in a *p*-*n* junction under equilibrium.

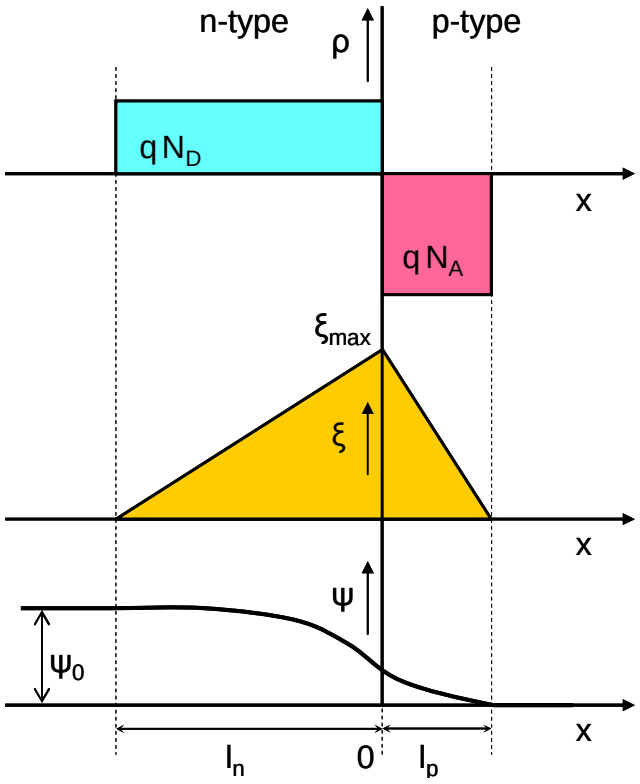

Figure 4.6. a) Space-charge density $\rho(x)$; b) electric field $\xi(x)$; c) electrostatic potential $\psi(x)$ across the depletion region of a *p*-*n* junction under equilibrium.

According to Figure 4.6 the position of the metallurgical junction is placed at zero, the width of the space-charge region in the *n*-type material is denoted as l_n and the width of the space-charge region in the *p*-type material is denoted as l_p. The space-charge density is described by following equations:

$$\rho(x) = q N_D \qquad \text{for } -l_n \le x \le 0 \qquad (4.3a)$$

$$\rho(x) = -q N_A \qquad \text{for } 0 \le x \le l_p \qquad (4.3b)$$

N_D and N_A is the concentration of donor and acceptor atoms, respectively. Outside the space-charge region the space-charge density is zero. The electric field is can be calculated from the Poisson' s equation, which has the following form for one dimensional analysis:

$$\frac{d^2\psi}{dx^2} = -\frac{d\xi}{dx} = -\frac{\rho}{\varepsilon_r \varepsilon_0}. \qquad (4.4)$$

In Eq. (4.4) ψ is the electrostatic potential, ξ is the electric field, ρ is the space-charge density, ε_r is the semiconductor dielectric constant and ε_0 is the permittivity of the vacuum. For crystalline Si ε_r = 11.7 and the permittivity of the vacuum ε_0 = 8.854x10^{-14} F/cm. The electric

field profile can be found by integrating the space-charge density across the space-charge region.

$$\xi = \frac{1}{\varepsilon_r \varepsilon_0} \int \rho \, dx \tag{4.5}$$

Substituting the space-charge density with Eqs. (4.3a) and (4.3b) and using the following boundary conditions:

$$\xi(-l_n) = \xi(l_p) = 0\,, \tag{4.6}$$

the solution for the electric field is

$$\xi(x) = \frac{q}{\varepsilon_r \varepsilon_0} N_D (l_n + x) \qquad \text{for } -l_n \le x \le 0 \tag{4.7a}$$

$$\xi(x) = \frac{q}{\varepsilon_r \varepsilon_0} N_A (l_p - x) \qquad \text{for } 0 \le x \le l_p \tag{4.7b}$$

At the metallurgical junction, $x = 0$, the electric field is continuous, which requires that the following condition has to be fulfilled

$$N_A l_p = N_D l_n \tag{4.8}$$

Outside the space-charge region the material is electrically neutral and therefore the electric field is zero there.

The profile of the electrostatic potential is calculated by integrating the electric field throughout the space-charge region and applying the boundary conditions.

$$\psi = -\int \xi \, dx \tag{4.9}$$

We define the zero electrostatic potential level at the outside edge of the *p*-type semiconductor. Since we assume no potential drop across the quasi-neutral region the electrostatic potential at the boundary of the space-charge region in the *p*-type material is also zero

$$\psi(l_p) = 0\,. \tag{4.10}$$

Using Eqs. 4.6a and 4.6b for describing the electric field in the *n*-type and *p*-type parts of the space-charge region, respectively, and taking into account that at the metallurgical junction the electrostatic potential is continuous, the solution for the electrostatic potential can be written as:

$$\psi(x) = -\frac{q}{2\varepsilon_r \varepsilon_0} N_D \ (x + l_n)^2 + \frac{q}{2\varepsilon_r \varepsilon_0}\left(N_D l_n^2 + N_A l_p^2\right) \qquad \text{for } -l_n \le x \le 0 \qquad (4.11a)$$

$$\psi(x) = \frac{q}{2\varepsilon_r \varepsilon_0} N_A \left(x - l_p\right)^2 \qquad \text{for } 0 \le x \le l_p \qquad (4.11b)$$

Under equilibrium a difference in electrostatic potential, ψ_0, develops across the space-charge region. The electrostatic potential difference across the *p*-*n* junction is an important characteristic of the junction and is denoted as the ***built-in potential*** or ***diffusion potential*** of the *p*-*n* junction. We can calculate ψ_0 as the difference between the electrostatic potential at the edges of the space-charge region:

$$\psi_0 = \psi(-l_n) - \psi(-l_p) = \psi(-l_n) \qquad (4.12)$$

Using Eq. 4.11a we obtain for the built-in potential the following expression:

$$\psi_0 = \frac{q}{2\varepsilon_r \varepsilon_0}\left(N_D l_n^2 + N_A l_p^2\right). \qquad (4.13)$$

Another way to determine the built-in potential ψ_0 is to use the energy-band diagram presented in Figure 4.4.

$$q\psi_0 = E_G - E_1 - E_2 \qquad (4.14)$$

Using Eq. (3.1) and Eqs (3.18a) and (3.18b), which determine the band gap, and the positions of the Fermi energy in the *n*-type and *p*-type semiconductor, respectively,

$$E_G = E_C - E_V$$
$$E_1 = E_C - E_F = kT \ln\left(N_C / N_D\right)$$
$$E_2 = E_F - E_V = kT \ln\left(N_V / N_A\right)$$

we can write

$$q\psi_0 = E_G - kT \ln\left(\frac{N_V}{N_A}\right) - kT \ln\left(\frac{N_C}{N_D}\right) = E_G - kT \ln\left(\frac{N_V N_C}{N_A N_D}\right) \qquad (4.15)$$

Using the relationship between the intrinsic concentration, n_i and the band gap, E_G, (Eq. (3.6))

$$n_i^2 = N_C N_V \exp\left[-E_G / kT\right],$$

we can rewrite Eq. (4.15) to obtain

$$\psi_0 = \frac{kT}{q} \ln\left(\frac{N_A N_D}{n_i^2}\right). \qquad (4.16)$$

Eq. (4.16) allows us to determine the built-in potential of a *p*-*n* junction from the standard semiconductor parameters, such as doping concentrations and the intrinsic carrier concentration. When knowing the built-in potential we can calculate the width of the space charge region of the *p*-*n* junction in the thermal equilibrium. Substituting ψ_0 using Eq. (4.16) into Eq. (4.13) and taking the condition (4.7) into account, the resulting expressions for l_n and l_p are obtained. The full derivation can be found for example in reference[2].

$$l_n = \sqrt{\frac{2\varepsilon_r \varepsilon_0}{q}\psi_0 \frac{N_A}{N_D}\left(\frac{1}{N_A + N_D}\right)} \tag{4.17a}$$

$$l_p = \sqrt{\frac{2\varepsilon_r \varepsilon_0}{q}\psi_0 \frac{N_D}{N_A}\left(\frac{1}{N_A + N_D}\right)} \tag{4.17b}$$

The total space-charge width, *W*, is the sum of the partial space-charge widths in the *n*-type and *p*-type semiconductors and can be calculated using Eq. (4.18).

$$W = l_n + l_p = \sqrt{\frac{2\varepsilon_r \varepsilon_0}{q}\psi_0 \left(\frac{1}{N_A} + \frac{1}{N_D}\right)} \tag{4.18}$$

The space-charge region is not uniformly distributed in the *n*-type and *p*-type regions. The widths of the space-charge region in the *n*-type and *p*-type semiconductor are determined by the doping concentrations as illustrated by Eqs. (4.17a) and (4.17b), respectively. Knowing the expressions for l_n and l_p we can determine the maximum value of the internal electric field, which is at the metallurgical junction. By substituting l_p expressed by Eq (4.17b) into Eq. (4.7b) we obtain the expression for the maximum value of the internal electric field.

$$\xi_{\max} = \sqrt{\frac{2q}{\varepsilon_r \varepsilon_0}\psi_0 \left(\frac{N_A N_D}{N_A + N_D}\right)} \tag{4.19}$$

[2] D.A. Neaman, Semiconductor Physics and devices: Basic Principles, McGraw-Hill, 2003.

EXAMPLE
A crystalline silicon wafer is doped with 1× 10^{16} acceptor atoms per cubic centimetre. A 1 micrometer thick emitter layer is formed at the surface of the wafer with a uniform concentration of 1×10^{18} donors per cubic centimetre. Assume a step p-n junction and that all doping atoms are ionized. The intrinsic carrier concentration in silicon at 300 K is 1.5×10^{10} cm^{-3}.

Let's calculate the electron and hole concentrations in the p-type and n-type quasi-neutral regions at thermal equilibrium. We shall use Eqs. (4.1a,b) and Eqs. (4.2a,b) to calculate the charge carrier concentrations.
P-type region:
$p = p_{p0} \approx N_A = 1\times 10^{16}\ cm^{-3}$.

$$n = n_{p0} = n_i^2 \big/ p_{p0} = \left(1.5\times10^{10}\right)^2 \big/ 10^{16} = 2.25\times10^{4}\ cm^{-3}$$

N-type region:
$n = n_{n0} \approx N_D = 1\times 10^{18}\ cm^{-3}$.

$$p = p_{n0} = n_i^2 \big/ n_{n0} = \left(1.5\times10^{10}\right)^2 \big/ 10^{18} = 2.25\times10^{2}\ cm^{-3}$$

We can calculate the position of the Fermi energy in the quasi-neutral n-type and p-type regions, respectively, using Eq. (3.18a). Let's assume that the reference energy level is the bottom of the conduction band, E_c=0 eV.

N-type region:

$$E_F - E_C = -kT\ln\left(N_C/n\right) = -0.0258\ \ln\left(3.32\times10^{19}/1\times10^{18}\right) = -0.09\,eV$$

P-type region:

$$E_F - E_C = -kT\ln\left(N_C/n\right) = -0.0258\ln\left(3.32\times10^{19}/2.25\times10^{4}\right) = -0.90\,eV$$

The minus sign tells us that the Fermi energy is positioned below the E_c.

The built-in voltage across the p-n junction is calculated using Eq. (4.16)

$$\psi_0 = \frac{kT}{q}\ln\left(\frac{N_A N_D}{n_i^2}\right) = 0.0258\ln\left(10^{16}\times10^{18}\big/\left(1.5\times10^{10}\right)^2\right) = 0.81V$$

The width of the depletion region is calculated from Eq. (4.18)

$$W = \sqrt{\frac{2\varepsilon_r\varepsilon_0}{q}\psi_0\left(\frac{1}{N_A}+\frac{1}{N_D}\right)} = \sqrt{\frac{2\times11.7\times8.854\times10^{-14}}{1.602\times10^{-19}}\times0.81\times\left(\frac{1}{10^{16}}+\frac{1}{10^{18}}\right)} = 3.25\times10^{-5}\ cm = 0.325\ \mu m$$

A typical thickness of c-Si wafer is 300 μm. The depletion region is 0.3 μm which represents 0.1% of the thickness of the wafer. It is important to realize that almost the whole bulk of the wafer is a quasi-neutral region without the internal electrical field.

The maximum electric field is at the metallurgical junction and is calculated from Eq. (4.19).

$$\xi_{\max} = \sqrt{\frac{2q}{\varepsilon_r\varepsilon_0}\psi_0\left(\frac{N_A N_D}{N_A+N_D}\right)} = \sqrt{\frac{2\times1.602\times10^{-19}}{11.7\times8.854\times10^{-14}}\times0.81\times\left(\frac{10^{16}\times10^{18}}{10^{16}+10^{18}}\right)} = 50\times10^{3}\ V\,cm^{-1}$$

4.2.3 *p-n* junction under applied voltage

When an external voltage, V_a, is applied to a *p-n* junction the potential difference between the *n*-type and *p*-type regions will change and the electrostatic potential across the space-charge region will become (ψ_0 - V_a). Remember that under equilibrium the built-in potential is negative in the *p*-type region with respect to the *n*-type region. When the applied external voltage is negative with respect to the potential of the *p*-type region, the applied voltage will increase the potential difference across the *p-n* junction. We refer to this situation as *p-n* junction under reverse-bias voltage. The potential barrier across the junction is increased under reverse-bias voltage, which results in a wider space-charge region. The band diagram of the *p-n* junction under reverse-biased voltage is presented in Figure 4.7a. Under external voltage the *p-n* junction is not under equilibrium any more and the concentrations of electrons and holes are described by the quasi-Fermi energy for electrons, E_{FC}, and the quasi-Fermi energy holes, E_{FV}, respectively. When the applied external voltage is positive with respect to the potential of the *p*-type region, the applied voltage will decrease the potential difference across the *p-n* junction. We refer to this situation as *p-n* junction under forward-bias voltage. The band diagram of the *p-n* junction under forward-biased voltage is presented in Figure 4.7b. The potential barrier across the junction is decreased under forward-bias voltage and the space charge region becomes narrower. The balance between the forces responsible for diffusion (concentration gradient) and drift (electric field) is disturbed. The lowering of the electrostatic potential barrier leads to a higher concentration of minority carriers at the edges of the space-charge region compared to the situation in equilibrium. This process is referred to as minority-carrier ***injection***. This gradient in concentration causes the diffusion of the minority carriers from the edge into the bulk of the quasi-neutral region.

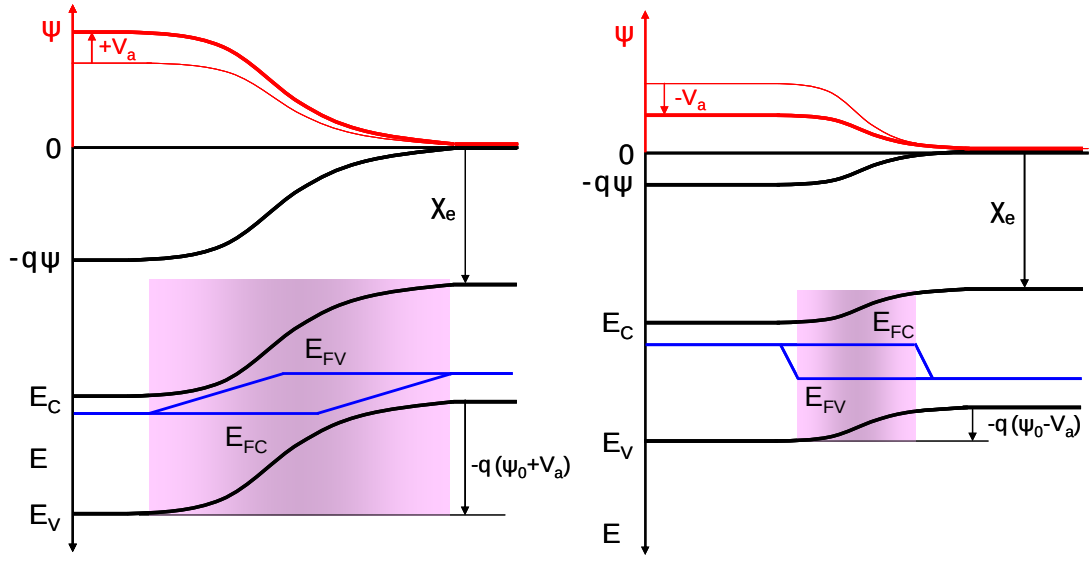

Figure 4.7: Energy band diagram and potential profile (in red colour) of a *p-n* junction under a) reverse bias, and b) forward bias.

The diffusion of minority carriers into the quasi-neutral region causes a so-called ***recombination current***, J_{rec}, since the diffusing minority carriers recombine with the majority carriers in the bulk. The recombination current is compensated by the so-called ***thermal generation current***, J_{gen}, which is caused by the drift of minority carriers, which are present in the corresponding doped regions (electrons in the *p*-type region and holes in the *n*-type region), across the junction. Both, the recombination and generation currents have contributions from electrons and holes. When no voltage is applied to the *p*-*n* junction, the situation inside the junction can be viewed as the balance between the recombination and generation currents.

$$J = J_{rec} - J_{gen} = 0 \qquad \text{for } V_a = 0 \text{ V} \tag{4.20}$$

It is assumed that when a moderate forward-bias voltage is applied to the junction the recombination current increases with the Boltzmann factor ($\exp(qV_a/kT)$) (*the Boltzmann approximation*):

$$J_{rec}(V_a) = J_{rec}(V_a = 0)\exp\left(\frac{qV_a}{kT}\right) \tag{4.21}$$

On the other hand, the generation current is almost independent of the potential barrier across the junction and is determined by the availability of the thermally-generated minority carriers in the doped regions.

$$J_{gen}(V_a) \approx J_{gen}(V_a = 0) \tag{4.22}$$

The external net-current density can be expressed as

$$J(V_a) = J_{rec}(V_a) - J_{gen}(V_a) = J_0\left[\exp\left(\frac{qV_a}{kT}\right) - 1\right], \tag{4.23}$$

where J_0 is the saturation-current density of the *p*-*n* junction, given by

$$J_0 = J_{gen}(V_a = 0) \tag{4.24}$$

Eq. (4.23) is known as the ***Shockley equation*** that describes the current-voltage behavior of an ideal *p*-*n* diode. It is a fundamental equation for microelectronics device physics. The detailed derivation of the dark-current density of the *p*-*n* junction is carried out in the Appendix 4.4.1 of Chapter 4. The saturation-current density is expressed by Eq. (4.25)

$$J_0 = q\, n_i^2\left(\frac{D_N}{L_N\, N_A} + \frac{D_P}{L_P\, N_D}\right). \tag{4.25}$$

The saturation-current density depends in a complex way on the fundamental semiconductor parameters. Ideally the saturation-current density should be as low as possible and this requires an optimal and balanced design of the *p*-type and *n*-type semiconductor properties.

For example, an increase in the doping concentration decreases the diffusion length of the minority carriers, which means that the optimal product of these two quantities requires a delicate balance between these two properties.

The recombination of the majority carriers due to the diffusion of the injected minority carriers into the bulk of the quasi-neutral regions results in a lowering of the concentration of the majority carriers compared to the one under equilibrium. The drop in the concentration of the majority carriers is balanced by the flow of the majority carriers from the electrodes into the bulk. In this way the net current flows through the *p-n* junction under forward-bias voltage. For high reverse-bias voltage, the Boltzmann factor in Eq. (4.23) becomes very small and can be neglected. The net current density is given by

$$J(V_a) = -J_0 , \tag{4.26}$$

and represents the flux of thermally generated minority carriers across the junction. The current density-voltage (*J-V*) characteristic of an ideal *p-n* junction is schematically shown in Figure 4.8.

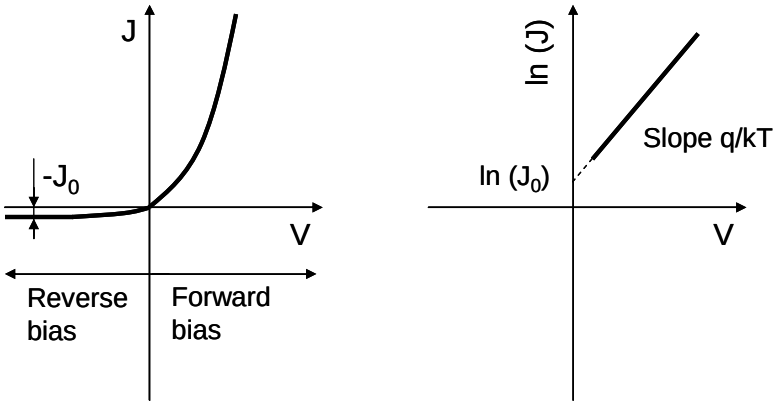

Figure 4.8. *J-V* characteristic of a *p-n* junction; a) linear plot and b) semi-logarithmic plot.

4.2.4 *p-n* junction under illumination

When a *p-n* junction is illuminated the additional electron-hole pairs are generated in the semiconductor. The concentration of minority carriers (electrons in the *p*-type region and holes in the *n*-type region) strongly increases. This increase in the concentration of minority carriers leads to the flow of the minority carriers across the depletion region into the qausi-neutral regions. Electrons flow from the *p*-type into the *n*-type region and holes from the *n*-type into the *p*-type region. The flow of the photo-generated carriers causes the so-called ***photo-generation current***, J_{ph}, which adds to the thermal-generation current, J_{gen}. When no external contact between the *n*-type and the *p*-type regions is established, which means that the junction is in the open-circuit condition, no net current can flow inside the *p-n* junction. It means that the current resulting from the flux of photo-generated and thermally-generated carriers has to be balanced by the opposite recombination current. The recombination current

will increase through lowering of the electrostatic potential barrier across the depletion region. This situation of the illuminated *p-n* junction under open-circuit condition using the band diagram is presented in Figure 4.9a. The electrostatic-potential barrier across the junction is lowered by an amount of V_{oc}. We refer to V_{oc} as the open-circuit voltage. Under non-equilibrium conditions the concentrations of electrons and holes are described by the quasi-Fermi energy levels. It is illustrated in Figure 4.9a that the electrochemical potential of electrons, denoted by E_{FC}, is higher in the n-type region than in the *p*-type region by an amount of $q\,V_{oc}$. This means that a voltmeter will measure a voltage difference of V_{oc} between the contacts of the *p-n* junction. Under illumination, when the *n*-type and *p*-type regions are short circuited, the photo-generated current will also flow through the external circuit. This situation is illustrated in Figure 4.9b. Under the short-circuit condition the electrostatic-potential barrier is not changed, but from a strong variation of the quasi-Fermi levels inside the depletion region one can determine that the current is flowing inside the semiconductor.

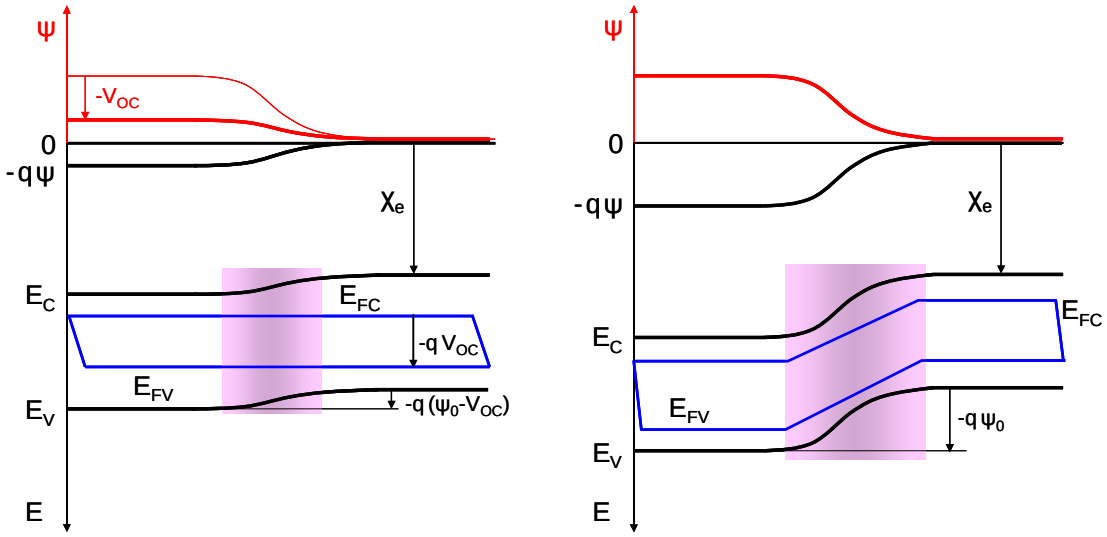

Figure 4.9. Energy band diagram and electrostatic-potential (in red colour) of an illuminated *p-n* junction under the a) open-circuit and b) short-circuit conditions.

When a load is connected between the electrodes of the illuminated *p-n* junction, only a fraction of the photo-generated current will flow through the external circuit. The electro-chemical potential difference between the *n*-type and *p*-type regions will be lowered by a voltage drop over the load. This in turn lowers the electrostatic potential over the depletion region which results in an increase of the recombination current. The net current flowing through the load is determined as the sum of the photo- and thermal generation currents and the recombination current (*the superposition approximation*). The voltage drop at the load can be simulated by applying a forward-bias voltage to the junction, therefore Eqs. (4.23), which describes the behaviour of the junction under applied voltage, is included to describe the net current of the illuminated *p-n* junction:

$$J(V_a) = J_{rec}(V_a) - J_{gen}(V_a) - J_{ph} = J_0\left[\exp\left(\frac{qV_a}{kT}\right) - 1\right] - J_{ph} \qquad (4.27)$$

The dark and illuminated *J-V* characteristics of the *p-n* junction are represented in Figure 4.10. Note, that the superposition principle is reflected in Figure 4.10. The illuminated *J-V* characteristic of the *p-n* junction is the same as the dark *J-V* characteristic, but it is shifted down by the photo-generated current density J_{ph}. The detailed derivation of the photo-generated current density of the *p-n* junction is carried out in the Appendix 4.4.2 of Chapter 4 and its value under uniform generation rate, *G*, is

$$J_{ph} = q\,G\left(L_N + W + L_P\right), \tag{4.28}$$

where L_N and L_P is the minority-carrier-diffusion length for electrons and holes, respectively, and *W* is the width of the depletion region. It means only carriers generated in the depletion region and in the regions up to the minority-carrier-diffusion length from the depletion region contribute to the photo-generated current. Eq. (4.28) is useful when designing the thickness of a solar cell. The thickness of the absorber should not be thicker than the region from which the carriers contribute to the photo-generated current.

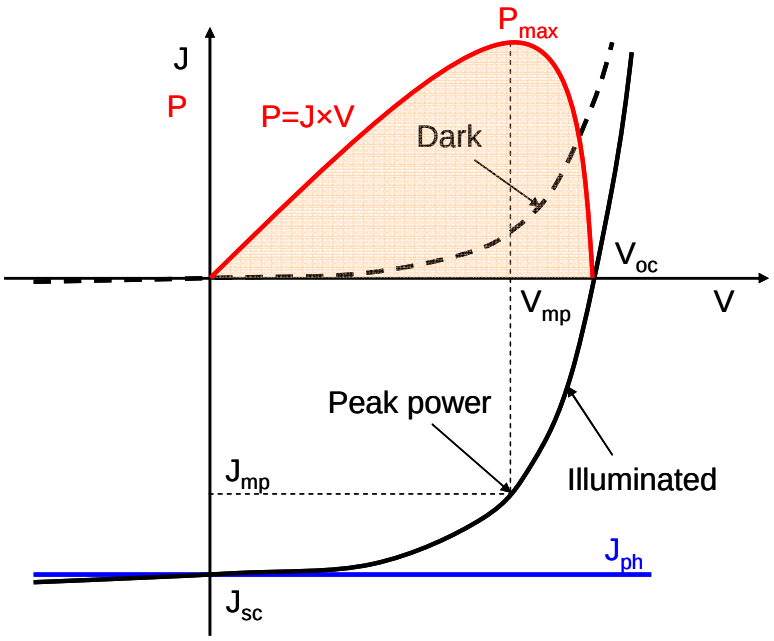

Figure 4.10. *J-V* characteristics of a *p-n* junction in the dark and under illumination.

4.3 Solar cell external parameters

The main parameters that are used to characterize the performance of solar cells are the peak power, P_{max}, the short-circuit current density, J_{sc}, the open-circuit voltage, V_{oc}, and the fill factor, *FF*. These parameters are determined from the illuminated *J-V* characteristic as illustrated in Figure 4.10. The conversion efficiency, η, is determined from these parameters.

Short-circuit current

The short-circuit current, I_{sc}, is the current that flows through the external circuit when the electrodes of the solar cell are short circuited. The short-circuit current of a solar cell depends on the photon flux density incident on the solar cell, that is determined by the spectrum of the incident light. For the standard solar cell measurements, the spectrum is standardized to the AM1.5 spectrum. The I_{sc} depends on the area of the solar cell. In order to remove the dependence of the I_{sc} on the solar cell area, the short-circuit current density is often used to describe the maximum current delivered by a solar cell. The maximum current that the solar cell can deliver strongly depends on the optical properties (absorption in the absorber layer and total reflection) of the solar cell.

In the ideal case, J_{sc} is equal to the J_{ph} as can be easily derived from Eq. (4.27). The J_{ph} can be approximated by Eq. (4.28), which shows that in case of ideal diode (for example no surface recombination) and uniform generation, the critical material parameters that determine the J_{ph} are the diffusion lengths of minority carriers. Crystalline silicon solar cells can deliver under an AM1.5 spectrum a maximum possible current density of 46 mA/cm^2. In laboratory c-Si solar cells the measured J_{sc} is above 42 mA/cm^2, and commercial solar cell have the J_{sc} over 35 mA/cm^2.

Open-circuit voltage

The open-circuit voltage is the voltage at which no current flows through the external circuit. It is the maximum voltage that a solar cell can deliver. The V_{oc} corresponds to the forward bias voltage, at which the dark current compensates the photo-current. The V_{oc} depends on the photo-generated current density and can be calculated from Eq. (4.26) assuming that the net current is zero.

$$V_{oc} = \frac{kT}{q} \ln\left(\frac{J_{ph}}{J_0} + 1 \right) \tag{4.29}$$

The above equation shows that V_{oc} depends on the saturation current of the solar cell and the photo-generated current. While J_{ph} typically has a small variation, the key effect is the saturation current, since this may vary by orders of magnitude. The saturation current density, J_0, depends on the recombination in the solar cell. Therefore, V_{oc} is a measure of the amount of recombination in the device. Laboratory crystalline silicon solar cells have o V_{oc} of up to 720 mV under the standard AM1.5 conditions, while commercial solar cells typically have V_{oc} above 600 mV.

Fill factor

The fill factor is the ratio between the maximum power ($P_{max} = J_{mp} \times V_{mp}$) generated by a solar cell and the product of V_{oc} and J_{sc} (see Figure 4.10).

$$FF = \frac{J_{mp} V_{mp}}{J_{sc} V_{oc}} \tag{4.30}$$

In case that the solar cell behaves as an ideal diode the fill factor can be expressed as a function of open-circuit voltage[3].

$$FF = \frac{v_{oc} - \ln(v_{oc} + 0.72)}{v_{oc} + 1}, \tag{4.31}$$

where $v_{oc} = \frac{q}{kT} V_{oc}$ is a normalized voltage. Eq. (4.31) is a good approximation of the ideal value of *FF* for $v_{oc} > 10$. The *FF* as a function of V_{oc} is shown in Figure 4.11. The figure shows that *FF* does not change drastically with a change in V_{oc}. For a solar cell with a particular absorber, large variations in V_{oc} are not common. For example, at standard illumination conditions, the difference between the maximum open-circuit voltage measured for a silicon laboratory device and a typical commercial solar cell is about 120 mV, giving the maximal *FF* of 0.85 and 0.83, respectively. However, the variation in maximum *FF* can be significant for solar cells made from different materials. For example, a GaAs solar cell may have a *FF* approaching 0.89.

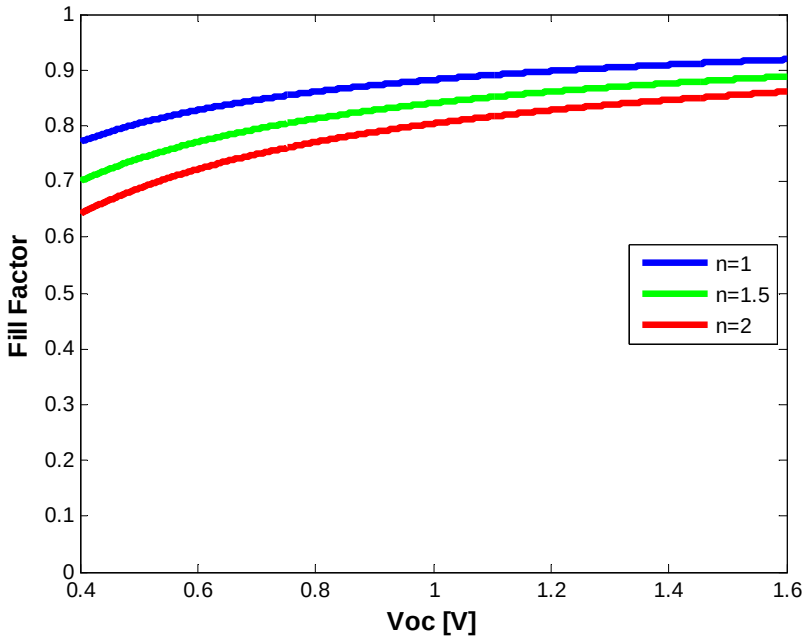

Figure 4.11. The *FF* as a function of V_{oc} for a solar cell with ideal diode behaviour.

However, in practical solar cells the dark diode current Eq. (4.23) does not obey the Boltzmann approximation. The non-ideal diode is approximated by introducing an ***ideality factor***, *n*, into the Boltzmann factor ($\exp(qV_a/nkT)$). Figure 4.11 also demonstrates the importance of the diode ideality factor when introduced into the normalized voltage ($v_{oc} = V_{oc}\, q/nkT$) in Eq. (4.31). The ideality factor is a measure of the junction quality and

[3] M.A. Green, Solar Cells; Operating Principles, Technology and System Applications, Prentice-Hall, 1982.

the type of recombination in a solar cell. For the ideal junction where the recombination is represented by the recombination of the minority carriers in the quasi-neutral regions the n-factor has a value of 1. However, when other recombination mechanisms occur, the *n* factor can have a value of 2. A high *n* value not only lowers the *FF*, but since it signals a high recombination, it leads to a low V_{oc}. Eq. (4.31) describes a maximum achievable *FF*. In practice the *FF* is often lower due to the presence of parasitic resistive losses.

Conversion efficiency

The conversion efficiency is calculated as the ratio between the generated maximum power and the incident power. The irradiance value, P_{in}, of 1000 W/m^2 of AM1.5 spectrum has become a standard for measuring the conversion efficiency of solar cells.

$$\eta = \frac{P_{\max}}{P_{in}} = \frac{J_{mp} V_{mp}}{P_{in}} = \frac{J_{sc} V_{oc} FF}{P_{in}} \tag{4.32}$$

Typical external parameters of a crystalline silicon solar cell as shown in Figure 3.1 are; J_{sc} of 35 mA/cm^2, V_{oc} up to 0.65 V and *FF* in the range 0.75 to 0.80. The conversion efficiency lies in the range of 17 to 18%.

EXAMPLE

A crystalline silicon solar cell generates a photo-current density J_{ph} = 35 mA/cm^2. The wafer is doped with 1×10^{17} acceptor atoms per cubic centimeter and the emitter layer is formed with a uniform concentration of 1×10^{19} donors per cubic centimeter. The minority-carrier diffusion length in the p-type region and n-type region is 500×10^{-6} m and 10×10^{-6} m, respectively.

The intrinsic carrier concentration in silicon at 300 K is 1.5×10^{10} cm^{-3}, the mobility of electrons in the p-type region is μ_n = 1000 cm^{2}V^{-1}s^{-1} and holes in the n-type region is μ_p = 100 cm^{2}V^{-1}s^{-1}.

Assume that the solar cell behaves as an ideal diode. Calculate the built-in voltage, open-circuit voltage and the conversion efficiency of the cell.

$J_{ph} = 350$ A/m^2.
$N_A = 1\times10^{17}$ cm^{-3} = 1×10^{23} m^{-3}.
$N_D = 1\times10^{19}$ cm^{-3} = 1×10^{25} m^{-3}.
$L_N = 500\times10^{-6}$ m.
$L_P = 10\times10^{-6}$ m.
$D_N = (kT/q)\,\mu_n = 0.0258\text{ V}\times 1000\times10^{-4}\text{ m}^2\text{V}^{-1}\text{s}^{-1} = 2.58\times10^{-3}\text{ m}^2\text{s}^{-1}$.
$D_P = (kT/q)\,\mu_p = 0.0258\text{ V}\times 100\times10^{-4}\text{ m}^2\text{V}^{-1}\text{s}^{-1} = 0.258\times10^{-3}\text{ m}^2\text{s}^{-1}$.

Using Eq (4.16) we calculate the built-in voltage of the cell:

$$\psi_0 = \frac{kT}{q}\ln\left(\frac{N_A N_D}{n_i^2}\right)$$

$\psi_o = 0.0258\text{ V}\times\ln((1\times10^{23}\text{ m}^{-3}\times1\times10^{25}\text{ m}^{-3})/(1.5\times10^{16})^2\text{ m}^{-6}) = 0.92$ V

According to the assumption the solar cell behaves as an ideal diode, it means that the Shockley equation describing the J-V characteristic is applicable. Using Eq. (4.25) we determine the saturation-current density:

$$J_0 = qn_i^2\left(\frac{D_N}{L_N N_A}+\frac{D_P}{L_P N_D}\right)$$

$J_0 = (1.602\times10^{-19}\text{ C}\times(1.5\times10^{16})^2\text{ m}^{-6})\times$
$[(2.58\times10^{-3}\text{ m}^2\text{s}^{-1}/(500\times10^{-6}\text{ m}\times1\times10^{23}\text{ m}^{-3})) + (0.258\times10^{-3}\text{ m}^2\text{s}^{-1}/(10\times10^{-6}\text{ m}\times1\times10^{25}\text{ m}^{-3}))] =$
$3.6\times10^{13}\text{ C m}^{-6}\times[(5.16\times10^{-23}+2.58\times10^{-24})\text{ m}^4\text{s}^{-1}] = 1.95\times10^{-9}\text{ C s}^{-1}\text{m}^{-2} = 1.95\times10^{-9}\text{ Am}^{-2}$

Using Eq. (4.29) we determine the open-circuit voltage:

$$V_{oc} = \frac{kT}{q}\ln\left(\frac{J_{ph}}{J_0}+1\right)$$

$V_{oc} = 0.0258\text{ V}\times\ln((350\text{ Am}^{-2}/1.95\times10^{-9}\text{ Am}^{-2})+1) = 0.67$ V

The fill factor of the cell can be calculated from Eq. (4.31). First we normalize the V_{oc}.

$v_{oc} = V_{oc}/(kT/q) = 0.67\text{ V}/0.0258\text{ V} = 26.8$

$$FF = \frac{v_{oc}-\ln(v_{oc}+0.72)}{v_{oc}+1}$$

$FF = (26.8 - \ln(26.8+0.72))/(26.8+1) = 0.84$

The conversion efficiency is determined using Eq. (4.32)

$$\eta = \frac{J_{sc}V_{oc}FF}{P_{in}}$$

$\eta = (350\text{ Am}^{-2}\times0.67\text{ V}\times0.84)/1000\text{ W m}^{-2} = 0.197$
$\eta = 19.7\%$

4.4 Appendix

4.4.1 Derivation of *J-V* characteristic in dark

When an external voltage, V_a, is applied to a *p-n* junction the potential difference between the *n*-type and *p*-type regions will change and the electrostatic potential across the space-charge region will become (ψ_0 - V_a). Under the forward-bias condition an applied external voltage decreases the electrostatic-potential difference across the *p-n* junction. The concentration of the minority carriers at the edge of the space-charge region increases exponentially with the applied forward-bias voltage but it is still much lower that the concentration of the majority carriers (*low-injection conditions*). The concentration of the majority carriers in the quasi-neutral regions do not change significantly under forward bias. The concentration of charge carriers in a *p-n* junction under forward bias is schematically presented in Figure 4.12.

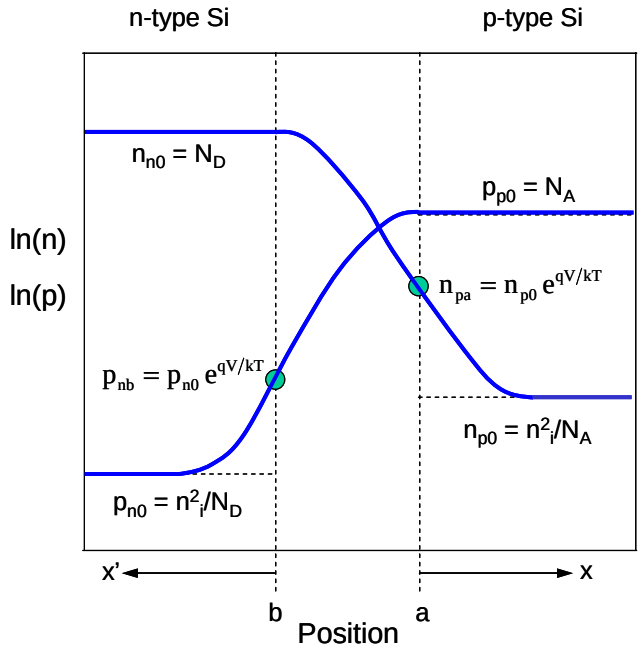

Figure 4.12. Concentration profiles of mobile charge carriers in a *p-n* junction under forward bias (blue line). Concentration profiles of carriers under thermal equilibrium are shown for comparison (black line).

The concentrations of the minority carriers at the edges of the space-charge region, electrons in the *p*-type semiconductor and holes in the *n*-type semiconductor after applying forward-bias voltage are described by Eq. (4.33a) and Eq. (4.33b), respectively.

$$n_{pb} = n_{p0} \exp[qV_a/kT] = \frac{n_i^2}{N_A} \exp[qV_a/kT] \qquad (4.33a)$$

$$p_{na} = p_{n0}\exp[qV_a/kT] = \frac{n_i^2}{N_D}\exp[qV_a/kT] \quad (4.33b)$$

Since it is assumed that there is no electric field in the quasi-neutral region the current-density equations of carriers reduce to only diffusion terms and are not coupled by the electric field. The current is based on the diffusive flows of carriers in the quasi-neutral regions and is determined by the diffusion of the minority carriers. The minority-carriers concentration can be calculated separately for both quasi-neutral regions. The electron-current density in the quasi-neutral region of the *p*-type semiconductor and the hole-current density in the quasi-neutral region of the *n*-type semiconductor are described by Eq. (4.34a) and Eq. (4.34b), respectively.

$$J_N = qD_N\frac{dn}{dx} \quad (4.34a)$$

$$J_P = -qD_P\frac{dp}{dx} \quad (4.34b)$$

The continuity equations (Eq. 3.54) for electrons and holes in steady-state ($\partial n/\partial t = 0$ and $\partial p/\partial t = 0$) can be written as

$$\frac{1}{q}\frac{dJ_N}{dx} - R_N + G_N = 0 \quad (4.35a)$$

$$-\frac{1}{q}\frac{dJ_P}{dx} - R_P + G_P = 0 \quad (4.35b)$$

Under *low-injection conditions*, a change in the concentration of the majority carriers due to generation and recombination can be neglected. However, the recombination-generation rate of minority carriers depends strongly on the injection and is proportional to the excess of minority carriers at the edges of the depletion region. The recombination-generation rate of electrons, R_N, in the *p*-type semiconductor and holes, R_P, in the *n*-type semiconductor is described by Eq. (3.29a) and Eq. (3.29b), respectively,

$$R_N = \frac{\Delta n}{\tau_n} \quad (4.36a)$$

$$R_P = \frac{\Delta p}{\tau_p}, \quad (4.36b)$$

where Δn is the excess concentration of electrons in the *p*-type semiconductor with respect to the equilibrium concentration n_{p0} and τ_n is the electrons (minority carriers) lifetime and Δp is the excess concentration of holes in the *n*-type semiconductor with respect to the equilibrium concentration p_{n0} and τ_p is the holes (minority carriers) lifetime. Δn and Δp are given by Eq. (4.37a) and Eq. (4.37b), respectively,

$$\Delta n = n_p(x) - n_{p0} \tag{4.37a}$$

$$\Delta p = p_n(x) - p_{n0} \tag{4.37b}$$

Combining Eq. (4.35a) with Eq. (4.34a) and Eq. (4.36a) results in Eq. (4.38a) that describes the diffusion of electrons in the *p*-type semiconductor, while combining Eq. (4.35b) with Eq. (4.34b) and Eq. (4.36b) results in Eq. (4.38b) that describes the diffusion of holes in the *n*-type semiconductor

$$D_N \frac{d^2 n_p(x)}{dx^2} = \frac{\Delta n}{\tau_n} - G_N \tag{4.38a}$$

$$D_P \frac{d^2 p_n(x)}{dx^2} = \frac{\Delta p}{\tau_p} - G_P \tag{4.38b}$$

Substituting $n_p(x)$ from Eq. (4.37a) and $p_n(x)$ from Eq. (4.37b) into Eq. (4.38a) and Eq. (4.38b), respectively, knowing that $d^2 n_{p0}/dx^2 = 0$, $d^2 p_{n0}/dx^2 = 0$ and in dark $G_N = G_P = 0$, Eqs. (4.38a) and Eq. (4.38b) simplify to

$$\frac{d^2 \Delta n}{dx^2} = \frac{\Delta n}{D_N \tau_n} \tag{4.39a}$$

$$\frac{d^2 \Delta p}{dx^2} = \frac{\Delta p}{D_P \tau_p} \tag{4.39b}$$

The electron-concentration profile in the quasi-neutral region of the *p*-type semiconductor is given by the general solution to Eq. (4.39a):

$$\Delta n(x) = A \exp\left(\frac{x}{L_N}\right) + B \exp\left(-\frac{x}{L_N}\right) \tag{4.40a}$$

where $L_N = \sqrt{D_N \tau_n}$ (Eq. (3.30a)) is the electron minority-carrier diffusion length. The starting point of the x axis is defined at the edge of the depletion region in the *p*-type semiconductor and denoted as a (see Figure 4.12). The infinite thickness of the *p*-type semiconductor is assumed (*approximation of the infinite thickness*). The constants *A* and *B* can be determined from the boundary conditions:

1. At $x = 0$, $n_{pa} = n_{p0} \exp(qV_a/kT)$,
2. n_p is finite at $x \to \infty$, therefore $A = 0$.

Using the boundary conditions the solution for the concentration profile of electrons in the *p*-type quasi-neutral region is

$$n_p(x) = n_{p0} + n_{p0}\left[\exp\left(\frac{qV_a}{kT}\right) - 1\right]\exp\left(-\frac{x}{L_N}\right), \tag{4.41a}$$

The hole concentration profile in the quasi-neutral region of the *n*-type semiconductor is given by the general solution to Eq. (4.39b):

$$\Delta p(x') = A'\exp\left(\frac{x'}{L_P}\right) + B'\exp\left(-\frac{x'}{L_P}\right) \tag{4.40b}$$

where $L_P = \sqrt{D_P \tau_p}$ (Eq. (3.30b)) is the hole minority-carrier diffusion length. The starting point of the x' axis ($x' = -x$) is defined at the edge of the depletion region in the *n*-type semiconductor and denoted as b (see Figure 4.12). The infinite thickness of the *n*-type semiconductor is assumed (*approximation of the infinite thickness*). The constants A' and B' can be determined from the boundary conditions:

1. At $x' = 0$, $p_{nb} = p_{n0}\exp(qV_a/kT)$,
2. p_n is finite at $x' \to \infty$, therefore $A' = 0$.

The concentration profile of holes in the quasi-neutral region of the *n*-type semiconductor is described by Eq. (4.41b).

$$p_n(x') = p_{n0} + p_{n0}\left[\exp\left(\frac{qV_a}{kT}\right) - 1\right]\exp\left(-\frac{x'}{L_P}\right) \tag{4.41b}$$

When substituting the corresponding concentration profiles of minority carriers (Eq. (4.41)) into Eq. (4.34) one obtains for the current densities:

$$J_N(x) = \frac{qD_N n_{p0}}{L_N}\left[\exp\left(\frac{qV_a}{kT}\right) - 1\right]\exp\left(-\frac{x}{L_N}\right) \tag{4.42a}$$

$$J_P(x') = \frac{qD_P p_{n0}}{L_P}\left[\exp\left(\frac{qV_a}{kT}\right) - 1\right]\exp\left(-\frac{x'}{L_P}\right) \tag{4.42b}$$

Under assumption that the effect of recombination and thermal generation of carriers in the depletion region can be neglected, which means that the electron and hole current densities are essentially constant across the depletion region, one can write for the current densities at the edges of the depletion region

$$J_N\big|_{x=0} = J_N\big|_{x'=0} = \frac{qD_N n_{p0}}{L_N}\left[\exp\left(\frac{qV_a}{kT}\right) - 1\right] \tag{4.43a}$$

$$J_P\big|_{x'=0} = J_P\big|_{x=0} = \frac{qD_P\, p_{n0}}{L_P}\left[\exp\left(\frac{qV_a}{kT}\right)-1\right] \tag{4.43b}$$

The total current density flowing through the *p-n* junction at the steady state is constant across the device therefore we can determine the total current density as the sum of the electron and hole current densities at the edges of the depletion region:

$$J(V_a) = J_N\big|_{x=0} + J_P\big|_{x=0} = \left(\frac{qD_N n_{p0}}{L_N} + \frac{qD_P\, p_{n0}}{L_P}\right)\left[\exp\left(\frac{qV_a}{kT}\right)-1\right] \tag{4.44}$$

Using Eq. (4.2b) and Eq. (4.1b), Eq. (4.44) can be rewritten as

$$J(V_a) = J_0\left[\exp\left(\frac{qV_a}{kT}\right)-1\right] \tag{4.45}$$

where J_0 is the saturation-current density of the *p-n* junction which is given by Eq. (4.46)

$$J_0 = \left(\frac{qD_N n_i^2}{L_N\, N_A} + \frac{qD_P\, n_i^2}{L_P\, N_D}\right) \tag{4.46}$$

Eq. (4.45) is known as the ***Shockley equation*** that describes the current-voltage behaviour of an ideal *p-n* diode. It is a fundamental equation for microelectronics device physics.

4.4.2 Derivation of *J-V* characteristic under illumination

When a *p-n* junction is illuminated the additional electron-hole pairs are generated through the junction. In case of moderate illumination the concentration of majority carriers does not change significantly while the concentration of minority carriers (electrons in the *p*-type region and holes in the *n*-type region) will strongly increase. In the following section it is assumed that the photo-generation rate, *G*, is uniform throughout the *p-n* junction (*uniform generation-rate approximation*). This assumption reflects a situation when the device is illuminated with a long-wavelength light which is weakly absorbed by the semiconductor. The concentration of charge carriers in a *p-n* junction with uniform photo-generation rate is schematically presented in Figure 4.13.

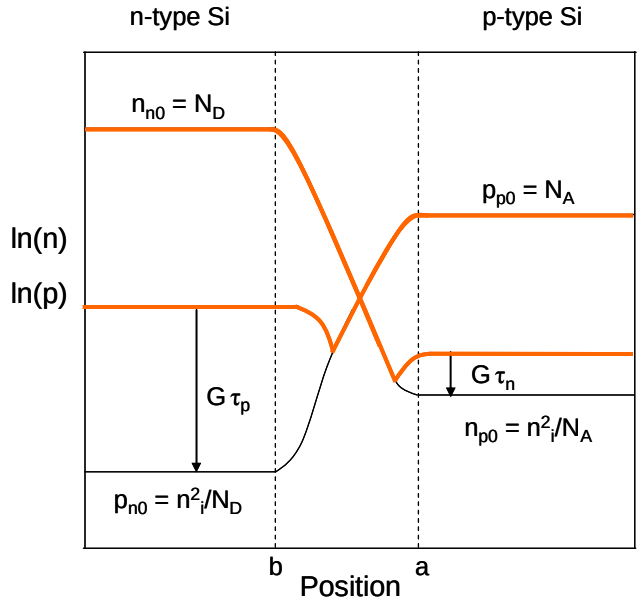

Figure 4.13: Concentration profiles of mobile charge carriers in an illuminated *p-n* junction with uniform generation rate *G* (orange line). Concentration profiles of charge carriers under equilibrium conditions are shown for comparison (black line).

Eqs. (4.38) describe the steady-state situation for minority carriers when the junction is illuminated. In this case the generation rate is not zero and the equation can be rewritten to

$$\frac{d^2\Delta n}{dx^2} = \frac{\Delta n}{D_N \tau_n} - \frac{G}{D_N} \qquad (4.47a)$$

$$\frac{d^2\Delta p}{dx^2} = \frac{\Delta p}{D_P \tau_p} - \frac{G}{D_P} \qquad (4.47b)$$

Under the assumption that G/D_N and G/D_P are constant, the general solution to Eq. (4.47) is

$$\Delta n(x) = G\tau_n + C\exp\left(\frac{x}{L_N}\right) + D\exp\left(-\frac{x}{L_N}\right) \tag{4.48a}$$

$$\Delta p(x') = G\tau_p + C'\exp\left(\frac{x'}{L_P}\right) + D'\exp\left(-\frac{x'}{L_P}\right) \tag{4.48b}$$

The constants in the Eqs. (4.48) can be determined from the same boundary conditions as were used in the analysis of the *p-n* junction in dark. The particular solution for the concentration profile of electrons in the quasi-neutral region of the *p*-type semiconductor and holes in the quasi-neutral region of the *n*-type semiconductor is described by Eq. (4.49a) and Eq. (4.49b), respectively.

$$n_p(x) = n_{p0} + G\tau_n + \left[n_{p0}\left(\exp\left(\frac{qV}{kT}\right)-1\right) - G\tau_n\right]\exp\left(-\frac{x}{L_N}\right) \tag{4.49a}$$

$$p_n(x') = p_{n0} + G\tau_p + \left[p_{n0}\left(\exp\left(\frac{qV}{kT}\right)-1\right) - G\tau_p\right]\exp\left(-\frac{x'}{L_P}\right) \tag{4.49b}$$

When substituting the corresponding concentration profiles of minority carriers (Eq. (4.49)) into Eq. (4.34) one obtains for the current densities:

$$J_N(x) = \frac{qD_N\, n_{p0}}{L_N}\left[\exp\left(\frac{qV}{kT}\right)-1\right]\exp\left(-\frac{x}{L_N}\right) - qGL_N\exp\left(-\frac{x}{L_N}\right) \tag{4.50a}$$

$$J_P(x') = \frac{qD_P\, p_{n0}}{L_P}\left[\exp\left(\frac{qV}{kT}\right)-1\right]\exp\left(-\frac{x'}{L_P}\right) - qGL_P\exp\left(-\frac{x'}{L_P}\right) \tag{4.50b}$$

In case of ideal *p-n* junction the effect of recombination in the depletion region was neglected. However, the contribution of photo-generated charge carriers to the current in the depletion region has to be taken into account. The contribution of optical generation from the depletion region to the current density is given by

$$J_N\big|_{x=0} = q\int_{-W}^{0}(-G)dx = -qGW \tag{4.51a}$$

$$J_P\big|_{x'=0} = q\int_{-W}^{0}(-G)dx' = -qGW \tag{4.51b}$$

The total current density flowing through the *p-n* junction in the steady state is constant across the junction therefore we can determine the total current density as the sum of the electron and hole current densities at the edges of the depletion region (the superposition approximation):

$$J(V_a) = J_N\big|_{x=0} + J_P\big|_{x=0} = \left(\frac{qD_N n_{p0}}{L_N} + \frac{qD_P\, p_{n0}}{L_P}\right)\left[\exp\left(\frac{qV_a}{kT}\right) - 1\right] - qG(L_N + L_P + W) \quad (4.52)$$

Eq. (4.52) can be rewritten as

$$J(V_a) = J_0\left[\exp\left(\frac{qV_a}{kT}\right) - 1\right] - J_{ph}, \quad (4.53)$$

where J_{ph} is the photo-current expressed by Eq. 4.28

$$J_{ph} = qG\left(L_N + W + L_P\right)$$

A number of approximations have been made in order to derive the analytical expressions for the current-voltage characteristics of an ideal *p-n* junction in dark and under illumination. The approximations are summarized below:

- The depletion-region approximation
- The Boltzmann approximation
- Low-injection conditions
- The superposition principle
- Infinite thickness of doped regions
- Uniform generation rate

The derived expressions describe the behaviour of an ideal *p-n* junction and help to understand the basic processes behind the operation of the *p-n* junction, but they do not fully and correctly describe practical *p-n* junctions. For example, the thickness of a *p-n* junction is limited, which means that the recombination at the surface of the doped regions has to be taken into account. The thinner a *p-n* junction is, the more important the surface recombination becomes. The surface recombination modifies the value of the saturation-current density. Further it was assumed that there are no recombination-generation processes in the depletion region. However, in real *p-n* junctions, the recombination in the depletion region represents a substantial loss mechanism. These and other losses in a solar cell are discussed in Chapter 5.

Chapter 5.

SOLAR CELL CONVERSION-EFFICIENCY LIMITS

5.1 Solar cell conversion efficiency and radiation spectrum

The conversion efficiency, η, of solar cells is calculated as the ratio between the generated maximum power, P_m, generated by a solar cell and the incident power, P_{in}. The incident power is equal to the irradiance of AM1.5 spectrum, normalized to 1000 W/m^2. The η is determined from the *I-V* measurement using Eq. (4.32).

$$\eta = \frac{P_m}{P_{in}} = \frac{J_{mp} V_{mp}}{P_{in}} = \frac{J_{sc} V_{oc} FF}{P_{in}}$$

The irradiance of AM1.5 spectrum can be calculated from the spectral power density, $P(\lambda)$, (see Figure 5.1) using the following equation:

$$P_{in} = \int_0^\infty P(\lambda) d\lambda \tag{5.1}$$

Using Eq. (2.3) that relates the photon flux density, $\Phi(\lambda)$, to the spectral power density, Eq. (5.2) can be written as:

$$P_{in} = \int_0^\infty \Phi(\lambda) \frac{hc}{\lambda} d\lambda \tag{5.2}$$

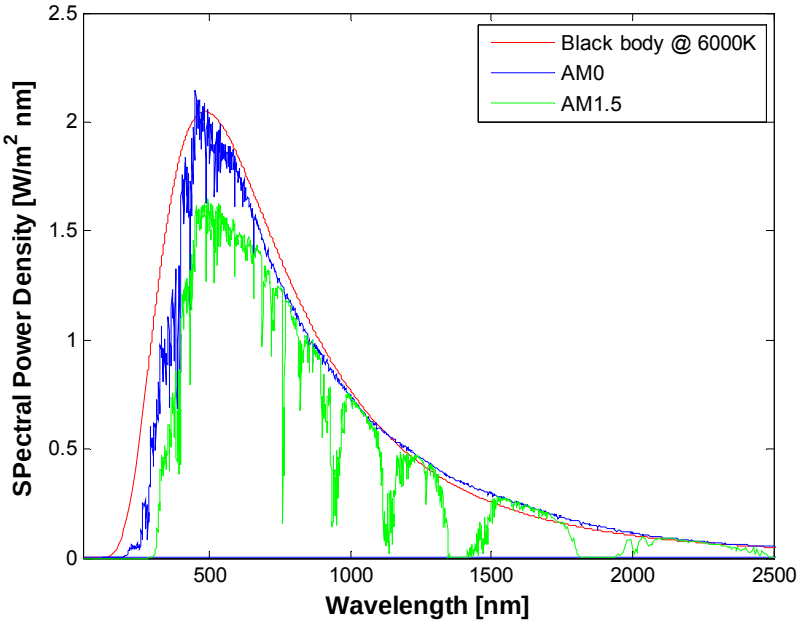

Figure 5.1. Spectral power density of black-body radiation at 6000 K, AMO and AM1.5 spectra.

5.2 Conversion efficiency limiting factors

5.2.1 Spectral mismatch

There are two principal losses that strongly reduce the energy conversion efficiency of today's solar cells. As discussed in Chapter 4, an important part of a solar cell is the absorber layer, in which the photons of the incident radiation are efficiently absorbed resulting in a creation of electron-hole pairs. The absorber layer of the solar cells is in most cases formed by a semiconductor material, which has its distinct optical properties characterized by the band gap energy, E_G, and the complex refractive index, $\tilde{n} = n - ik$. In principle, only photons with energy higher than the band gap energy of the absorber generate electron-hole pairs. Since the electrons and holes tend to occupy energy levels at the bottom of the conduction band and the top of the valence band, respectively, the extra energy that the electron-hole pairs receive from the photons is released as heat into the semiconductor lattice in the ***thermalization*** process. Photons with energy lower than the band gap energy of the semiconductor absorber are in principle not absorbed and cannot generate electron-hole pairs. Therefore these photons are not involved in the energy conversion process. The ***non-absorption*** of photons carrying less energy than the semiconductor band gap and the excess energy of photons, larger than the band gap, are the two main losses in the energy conversion process using solar cells. Both of these losses are thus related to the ***spectral mismatch*** of the energy distribution of photons in the solar spectrum and the band gap of a semiconductor material

We can determine the fraction of energy of the incident radiation spectrum that is absorbed by a single junction solar cell. When we denote λ_G as the wavelength of photons that corresponds to the band gap energy of the absorber of the solar cell, only the photons with the energy higher than the band gap are absorbed, it means photons with $\lambda \leq \lambda_G$. The fraction of the incident power, p_{abs} that is absorbed by a solar cell and used for energy conversion is expressed as:

$$p_{abs} = \frac{\int_0^{\lambda_G} \Phi(\lambda) \frac{hc}{\lambda} d\lambda}{\int_0^{\infty} \Phi(\lambda) \frac{hc}{\lambda} d\lambda} \tag{5.3}$$

A part of the absorbed energy, the excess energy of photons, is lost due tot the thermalization of photo-generated electrons and holes in the absorber material. The fraction of the absorbed energy that the solar can deliver as useful energy, p_{use}, is described by Eq. (5.4):

$$p_{use} = \frac{E_G \int_0^{\lambda_G} \Phi(\lambda) d\lambda}{\int_0^{\lambda_G} \Phi(\lambda) \frac{hc}{\lambda} d\lambda} \tag{5.4}$$

We can determine the conversion efficiency limited by the spectral mismatch:

$$\eta = p_{abs} p_{use} = \frac{\int_0^{\lambda_G} \Phi(\lambda) \frac{hc}{\lambda} d\lambda}{\int_0^{\infty} \Phi(\lambda) \frac{hc}{\lambda} d\lambda} \frac{E_G \int_0^{\lambda_G} \Phi(\lambda) d\lambda}{\int_0^{\lambda_G} \Phi(\lambda) \frac{hc}{\lambda} d\lambda} \tag{5.5}$$

Figure 5.2 illustrates the fraction of the AM1.5 spectrum that can be converted into a usable energy by a crystalline silicon solar cell.

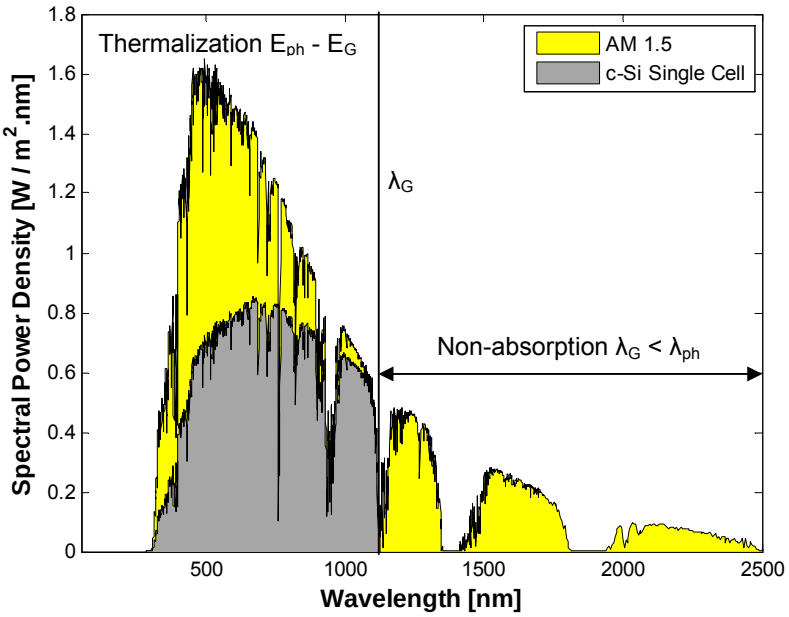

Figure 5.2. The fraction of the AM1.5 spectrum that can be converted into a usable energy by a crystalline silicon solar cell.

Figure 5.3 shows the conversion efficiency of a solar cells limited only by spectral mismatch as a function of the band gap of a semiconductor absorber for three different radiation spectra, black-body radiation at 6000 K, AM0 and AM1.5 solar radiation spectra. The figure demonstrates that in the case of a crystalline silicon solar cell (E_G = 1.1 eV) the losses due to the spectral mismatch account for almost 50 %. It also shows that an optimal absorber material for a single junction solar cell has a band gap of 1.1 eV and 1.0 eV for AM0 and AM1.5 spectrum, respectively. Note that the maximum conversion efficiency for the AM1.5 spectrum is higher than that for AM0, while the AM0 spectrum has a higher overall power density. This is caused by the fact that the AM1.5 spectrum has a lower power density in parts of the spectrum that are not contributing to the energy conversion process as can be seen in Fig. 5.2. The dips in the AM1.5 spectrum also result in the irregular shape of the maximum conversion efficiency as function of the band gap.

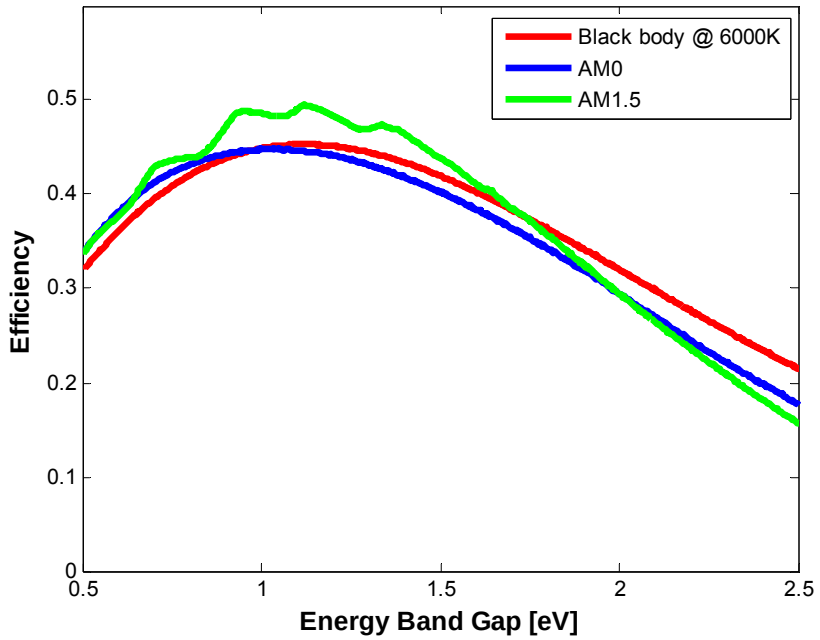

Figure 5.3. Maximum conversion efficiency for the black body spectrum at 6000 K, the AM0 and AM1.5 solar radiation spectra, limited only by the spectral mismatch as a function of the band gap of a semiconductor absorber in single junction solar cells.

5.2.2 Solar cell optical properties

As mentioned in the previous section there are also other optical parameters than E_G that have influence on the conversion efficiency of a solar cell. These are optical constants of the individual layers,that are expressed in the complex refractive index $\tilde{n}=n - ik$. The optical constants, refractive index, n, and extinction coefficient, k, are function of the wavelength.

In general, when light arrives on an interface between two media, a part of the light is reflected from and the other part is transmitted through the interface. The interface is therefore characterized by the wavelength dependent reflectance, $R(\lambda)$, and transmittance, $T(\lambda)$. Reflectance is the ratio of the energy reflected from the surface of the interface to the total

incident energy. There is a reflection of light at the interface between the first layer of a solar cell and the incident medium, usually air, and there is also reflection at the interfaces between the individual layers within the solar cell. All these processes result in a total reflectance between the solar cell and air. This means that a part of the incident energy that can be converted into a usable energy by the solar cell is lost by ***reflection***. We shall denote the total reflectance as R^*, which can be considered as the effective reflectance in the wavelength range of interest.

In most c-Si solar cells one of the metal electrodes is placed on the front side of the cell. The metal-covered area does not allow the light to enter the solar cell because it totally reflects the light in wavelength range of interest. The area that is covered by the electrode effectively decreases the active area of the solar cell through which the light enters the solar cell. When we denote the total area of the cell A_{tot} and the cell area that is not covered by the electrode A_f, the active area of the cell is determined by the ratio of A_f/A_{tot}. This ratio is called the ***coverage factor*** and determines the so called ***shading losses***. The design of the front electrode is therefore of great importance since in order to minimize the losses due to the series resistance of the front electrode, it should be designed with sufficient cross-section. The optimal design of the front electrode is a trade-off between a high coverage factor and a sufficiently low series resistance of the front electrode.

When light penetrates into a material, it will be absorbed as it propagates through the material. The absorption of light in the material depends on its absorption coefficient which is related to the extinction coefficient through Eq. (3.32). In general, light is absorbed in all layers that form the solar cell. However, the solar cell is optimally designed when most of the incident light is absorbed in the absorber layer. Due to the limited thickness of the absorber layer, not all the light entering the absorber layer is absorbed. ***Incomplete absorption*** in the absorber due to its limited thickness is an additional loss that lowers the efficiency of the energy conversion. The incomplete absorption loss can be described by the internal optical quantum efficiency, QE_{op}, which is the probability of a photon being absorbed in a material. Since there is a chance that a high energetic photon can generate more than one electron-hole pair, we define the quantum efficiency for carrier generation, η_g, which represents the number of electron-hole pairs generated by one absorbed photon. Usually η_g is assumed to be unity.

5.2.3 Solar cell collection losses

Not all charge carries that are generated in a solar cell are collected at the electrodes. The photo-generated carries are the excess carriers with respect to the thermal equilibrium and are subjected to the ***recombination***. The carriers recombine in the bulk, at the interfaces, and/or at the surfaces of the junction. The recombination is determined by the electronic properties of materials that form the junction, such as density of states introduced into the band gap by the R-G centers. The concentration of R-G centers strongly influences the minority-carrier lifetimes as discussed in Chapter 3.

The contributions of both the electronic and optical properties of the solar cell materials to the photovoltaic performance are taken into account in the absolute external quantum efficiency. The absolute external quantum efficiency is defined as the number of charge carriers collected (from all layers of the device) per incident photon at each wavelength λ. This quantum efficiency can be approximated as

$$QE(\lambda) = (1 - R^*)\, QE_{op}(\lambda)\eta_g(\lambda)\, QE_{el}(\lambda), \tag{5.6}$$

Where the QE_{el} is the electrical quantum efficiency and is defined as the probability that a photo-generated carrier is collected. When we combine the absolute external quantum efficiency (Eq. (5.6)) and shading losses with the photon flux density of the spectrum of incident radiation we can determine the expected short-circuit current density that a solar cell can deliver. The maximal current density that the solar cell can deliver is determined by the band gap of the absorber layer that determines which photons of the incident radiation can generate electron-hole pairs. When we assume that all these photons are absorbed and all generated carriers are collected the maximum current density, J_{max}, is described as:

$$J_{\max} = q \int_0^{\lambda_G} \Phi(\lambda)\, d\lambda \tag{5.7}$$

The short-circuit current density is determined by the absolute external quantum efficiency and the shading loss:

$$J_{sc} = J_{\max} \left(1 - R^*\right) QE_{opt}\, \eta_G\, QE_{el}\, \frac{A_f}{A_{tot}} \tag{5.8}$$

Combining Eq. (5.7) and Eq. (5.8) we obtain:

$$J_{sc} = q \left(1 - R^*\right) QE_{opt}\, \eta_G\, QE_{el}\, \frac{A_f}{A_{tot}} \int_0^{\lambda_G} \Phi(\lambda)\, d\lambda \tag{5.9}$$

Note that the upper limit of the integration is set at the wavelength corresponding to the band gap of the absorber layer. Photons with larger wavelength (lower energy) cannot generate electron hole pairs. Therefore QE_{op} equals zero larger wavelengths.

5.2.4 Additional limiting factors

In chapter 4 we discussed that the V_{oc} of a solar cell depends on the saturation current and the photo-generated current (Eq. (4.29)) of the solar cell. The saturation current density depends on the recombination in the solar cell that cannot be avoided and is referred to as the ***fundamental recombination***. This fundamental recombination depends on the doping of the different regions (n-type and p-type regions) of a junction and the electronic quality of materials forming the junction. The doping levels and the recombination determine the ***voltage factor***, qV_{oc}/E_G, that is the ratio of the maximum voltage developed by the solar cell (V_{oc}) to the voltage related to the band-gap of the absorber (E_G/q).

The maximum power generated by a solar cell is dependent on the ***fill factor***, *FF*. In case of a solar cell that behaves as an ideal diode only direct recombination occurs and the maximal *FF* is a function of V_{oc} and can be approximated by Eq. (4.31). In a practical solar cell the *FF* is lower than the ideal value due to following reasons:

- The voltage drop due to the series resistance R_s of a solar cell. The series resistance is introduced by the resistance of the main current path through which the photo-generated carriers arrive to the external circuit. The contributions to the series resistance come from the bulk ressistance of the junction, the contact resistance between the junction and electrodes, the resistance of the electrodes.

- The voltage drop due to the leakage current and characterized by the shunt resistance R_p of a solar cell. The leakage current is caused by the current through local defects in the junction or due to the shunts at the edges of solar cells.
- The recombination in a non-ideal solar cell results in a decrease of the *FF*.

5.2.5 Conversion efficiency

The conversion efficiency determined from the I-V measurement can be expressed as:

$$\eta = \frac{J_{sc} V_{oc} FF}{P_{in}}$$

Using Eq. (5.2) and Eq. (5.9) we can rewrite the expression for the conversion efficiency as

$$\eta = \frac{q \int_0^{\lambda_G} \Phi^0(\lambda)\, d\lambda}{\int_0^{\infty} \Phi^0(\lambda) \frac{hc}{\lambda} d\lambda} \left(1 - R^*\right) QE_{opt}\, \eta_G\, QE_{el} \frac{A_f}{A_{tot}} V_{oc}\, FF \tag{5.10}$$

We can introduce the voltage factor (qV_{oc}/E_G) into Eq. (5.10) by expressing the V_{oc} as:

$$V_{oc} = \frac{qV_{oc}}{E_G} \frac{E_G}{q} \tag{5.11}$$

$$\eta = \frac{q \int_0^{\lambda_G} \Phi^0(\lambda)\, d\lambda}{\int_0^{\infty} \Phi^0(\lambda) \frac{hc}{\lambda} d\lambda} \left(1 - R^*\right) QE_{opt}\, \eta_G\, QE_{el} \frac{A_f}{A_{tot}} \frac{qV_{oc}}{E_G} \frac{E_G}{q} FF \tag{5.12}$$

By introducing a term $\frac{\int_0^{\lambda_G} \Phi^0(\lambda) \frac{hc}{\lambda} d\lambda}{\int_0^{\lambda_G} \Phi^0(\lambda) \frac{hc}{\lambda} d\lambda}$ into the right side of Eq. (5.12) and manipulating it, the conversion efficiency can be now written as[1]

$$\eta = \underbrace{\frac{\int_0^{\lambda_G} \Phi^0(\lambda) \frac{hc}{\lambda} d\lambda}{\int_0^{\infty} \Phi^0(\lambda) \frac{hc}{\lambda} d\lambda}}_{1} \underbrace{\frac{E_G \int_0^{\lambda_G} \Phi^0(\lambda) d\lambda}{\int_0^{\lambda_G} \Phi^0(\lambda) \frac{hc}{\lambda} d\lambda}}_{2} \underbrace{\left(1 - R^*\right)}_{3} \underbrace{QE_{opt}^*\, \eta_G^*}_{4} \underbrace{QE_{el}^*}_{5} \underbrace{\frac{A_f}{A_{tot}}}_{6} \underbrace{\frac{qV_{oc}}{E_G}}_{7} \underbrace{FF}_{8} \tag{5.13}$$

[1] R.J. van Overstraeten, R.P. Mertens, Physics, Technology and Use of Photovoltaics, Adam Hilger Ltd, 1986.

Eq. (5.13) describes the conversion efficiency of a solar cell in terms of components that represent particular losses in energy conversion.

1. Loss due to non-absorption of long wavelengths
2. Loss due to thermalization of the excess energy of photons
3. Loss due to the total reflection
4. Loss by incomplete absorption due to the finite thickness
5. Loss due to recombination
6. Loss by metal electrode coverage, shading losses
7. Loss due to voltage factor
8. Loss due to fill factor

Figure 5.4 shows the efficiency as a function of the band gap of the absorber of an ideal solar cell, such that losses due to 3, 4, 6 are eliminated.

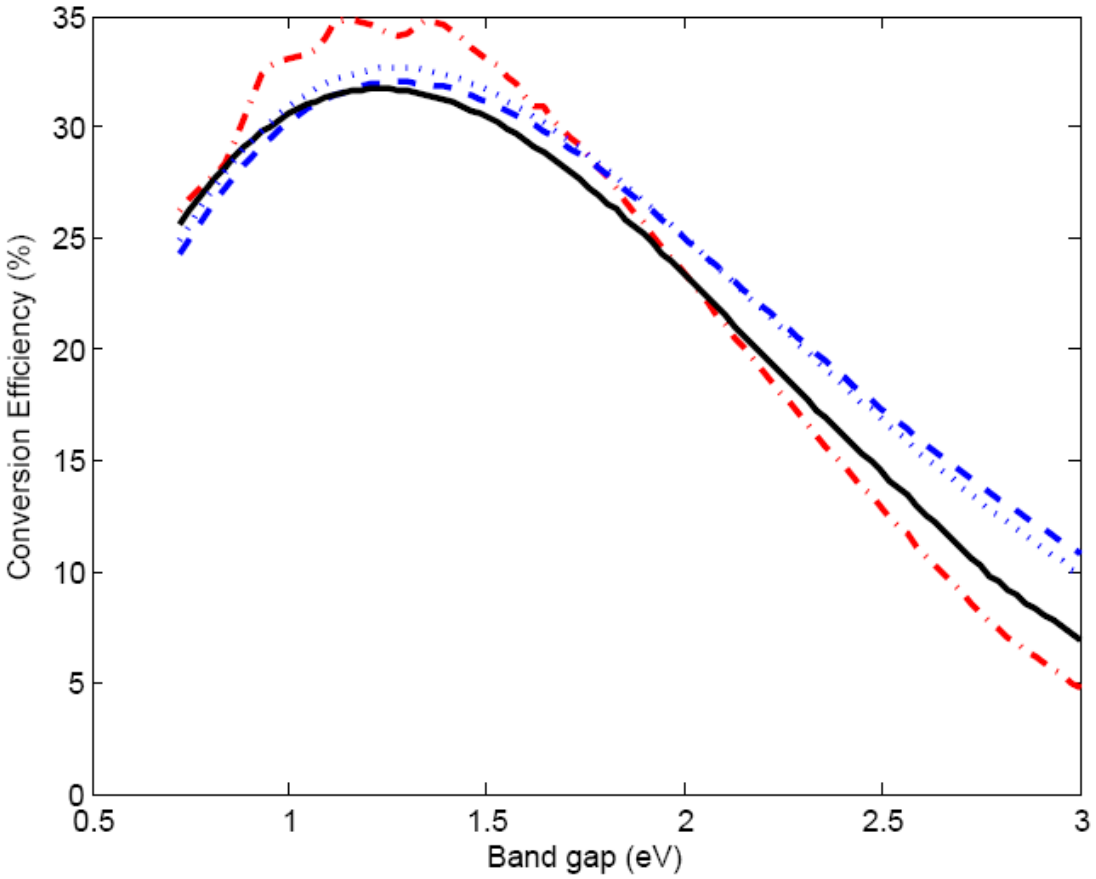

Figure 5.4. The detailed balance efficiency limit as a function of the band gap of a solar cell illuminated by different incident spectra: Black body radiator at 6000K (blue dots); sampled black body radiator (blue dashes); AM0 (black solid line); AM1.5 (red dash-dot).

5.3 Equivalent circuit

The *J-V* characteristic of an illuminated solar cell that behaves as the ideal diode is discribed by Eq. (4.27):

$$J = J_0\left[\exp\left(\frac{qV}{kT}\right)-1\right]-J_{ph}$$

This behaviour can be described by a simple equivalent circuit, in which a diode and a current source are connected in parallel. The equivalent circuit is shown in Figure 5.5a. The diode is formed by a p-n junction. The first term in Eq. (4.27) describes the dark diode current density and the second term describes the photo-generated current density. In practice the *FF* is influenced by the series resistance, R_s, and the shunt resistance, R_p, of a solar cell. The influence of these parameters on the *J-V* characteristic of the solar cell can be studied using the equivalent circuit presented in Figure 5.5b. The *J-V* characteristic of the one-diode equivalent circuit with the series resistance and the shunt resistance is described by (*A* is the area of the solar cell):

$$J = J_0\left[\exp\left(\frac{q(V-AJR_s)}{kT}\right)-1\right]+\frac{V-AJR_s}{R_p}-J_{ph} \qquad (5.14)$$

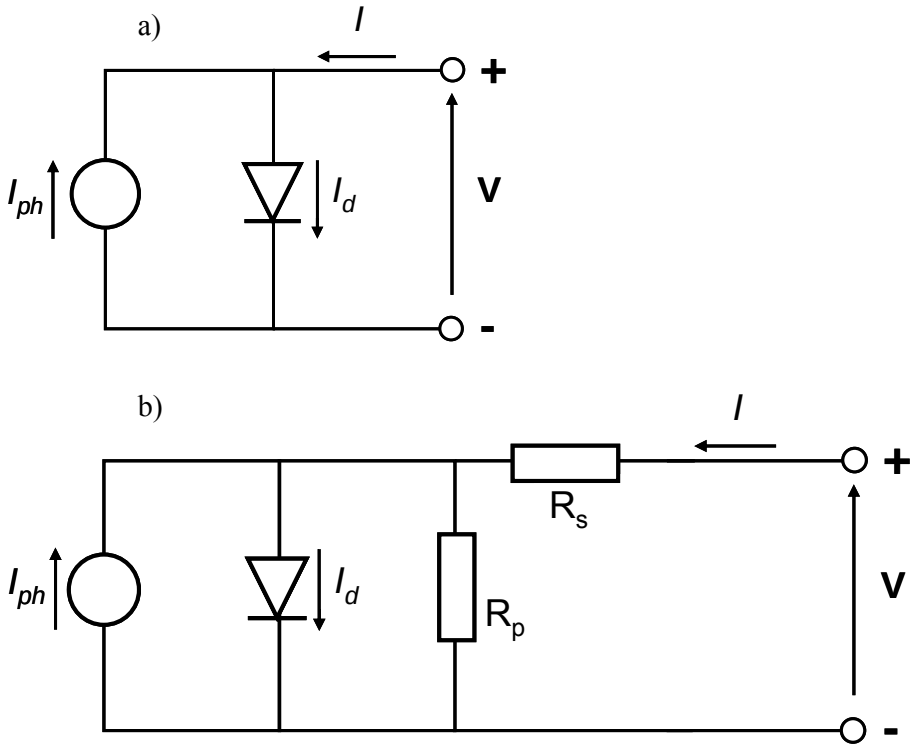

Figure 5.5. a) The equivalent circuit of an ideal solar cell. b) The equivalent circuit of a solar cell with series and shunt resistance. R_s is the series resistance, R_p is the shunt resistance.

The effect of R_s and R_p on the *J-V* characteristic is illustrated in Figure 5.6a and 5.6b, respectively.

a)

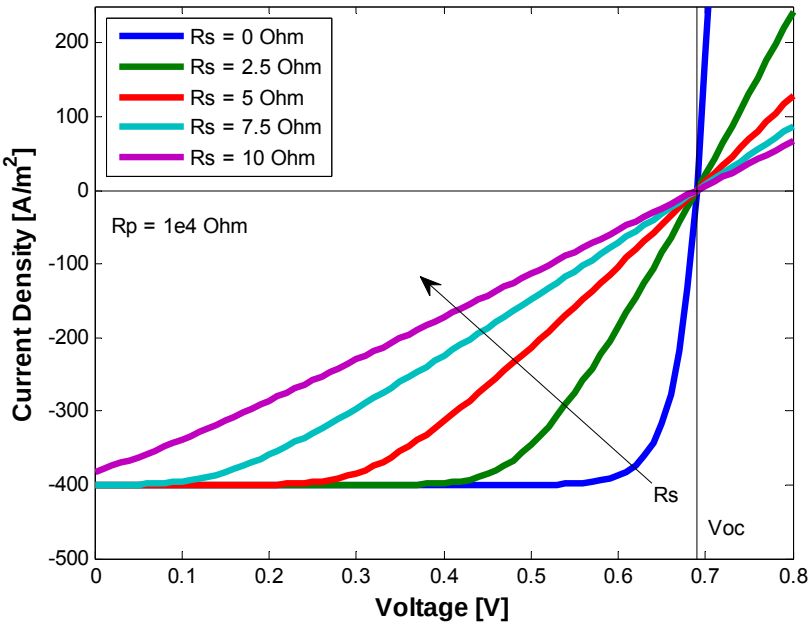

b)

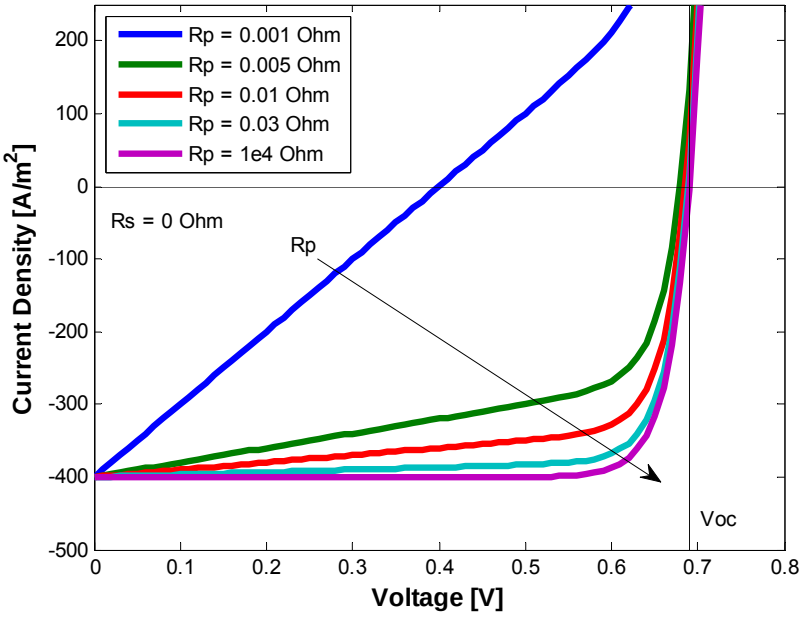

Figure 5.6. Effect of parasitic resistances on the *J-V* characteristic of a solar cell.

In practical solar cells the *FF* is influenced by the additional recombination occurring in the p-n junction. This non-ideal diode is often represented in the equivalent circuit by two diodes, an ideal one with an ideality factor equal to unity and a non-ideal diode with an ideality factor larger than unity. The equivalent circuit of a practical solar cell is presented in Figure 5.7. The *J-V* characteristic of the two-diode equivalent circuit is described by:

$$J = J_{01}\left[\exp\left(\frac{q(V - AJR_s)}{n_1 kT}\right) - 1\right] + J_{02}\left[\exp\left(\frac{q(V - AJR_s)}{n_2 kT}\right) - 1\right] + \frac{V - AJR_s}{R_p} - J_{ph} \qquad (5.15)$$

The J_{01} and J_{02} are the saturation currents of the two diodes, respectively, and n_1 and n_2 are the ideality factors of the two diodes.

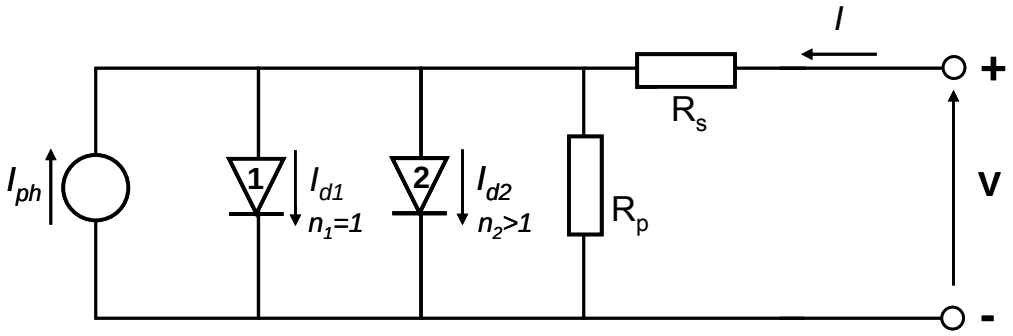

Figure 5.7. The equivalent circuit of a solar cell based on a two-diode model.

EXAMPLE.
A commercial multi-crystalline silicon solar cell with a so-called H-pattern as a front contact design (see figure) has the following specifications:
• V_{oc}=605 mV, I_{sc}=5.0 A,
• V_{mpp}=500 mV, I_{mpp}=4.6 A,
• size:156 cm^2,
• 9% metallization coverage.
V_{mpp} and I_{mpp} are the voltage and current, respectively, at the maximum power point

a) Calculate the total area and active area efficiency of the cell, respectively (irradiance: 100 mW/cm^2)
$\eta_{ta}=V_{mpp}\times I_{mpp}/(156\ cm^2\times 0.1\ Wcm^{-2})\times 100\%=0.5\times 4.6/(156\times 0.1)\times 100\%=14.7\%$
$\eta_{aa}=V_{mpp}\times I_{mpp}/(156\ cm^2\times 0.91\times 0.1\ Wcm^{-2})\times 100\%=0.5\times 4.6/(156\times 0.91\times 0.1)\times 100\%=16.2\%$

b) Calculate the fill factor FF of the cell
$FF=V_{mpp}\times I_{mpp}/(V_{oc}\ x\ I_{sc})=0.5\times 4.6/(0.605*5)=0.760.$

Cells with these characteristics will be interconnected with strips (see figure). This will result in an additional 2 mΩ series resistance loss.
c) Calculate the lower FF due to this higher series resistance (Hint: use the voltage drop at the maximum power point to calculate the lower FF)
$\Delta V=I_{mpp}\Delta R=4.6\times 2\cdot 10^{-3}=9.2\cdot 10^{-3}$ V = 9.2 mV
$\Delta FF=\Delta V/V_{mpp}\times FF=9.2/500\times 0.760=0.014$; $FF_{new}=0.760-0.014=0.746$

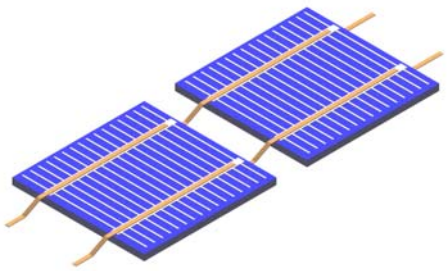

Figure: Standard cells with H pattern and interconnection strips

Chapter 7.

THIN-FILM SILICON SOLAR CELLS

7.1 Introduction

The simplest semiconductor junction that is used in solar cells for separating photo-generated charge carriers is the *p*-*n* junction, an interface between the *p*-type region and *n*-type region of one semiconductor. Therefore, the basic semiconductor property of a material, the possibility to vary its conductivity by doping, has to be demonstrated first before the material can be considered as a suitable candidate for solar cells. This was the case for amorphous silicon.

The first amorphous silicon layers were reported in 1965 as films of "silicon from silane" deposited in a radio frequency glow discharge[1]. Nevertheless, it took more ten years until Spear and LeComber, scientists from Dundee University, demonstrated that amorphous silicon had semiconducting properties by showing that amorphous silicon could be doped *n*-type and *p*-type by adding phosphine or diborane to the glow discharge gas mixture, respectively[2]. This was a far-reaching discovery since until that time it had been generally thought that amorphous silicon could not be doped. At that time it was not recognised immediately that hydrogen played an important role in the newly made amorphous silicon doped films. In fact, amorphous silicon suitable for electronic applications, where doping is required, is an alloy of silicon and hydrogen. The electronic-grade amorphous silicon is therefore called ***hydrogenated amorphous silicon*** (***a*-Si:H**).

[1] H.F. Sterling and R.C.G. Swann, *Solid-State Electron*. **8** (1965) p. 653-654.
[2] W. Spear and P. LeComber, *Solid State Comm*. **17** (1975) p. 1193-1196.

The successful doping of amorphous silicon initiated a tremendous interest in this material and the research activities in this field grew explosively all over the world. There were two main reasons for this interest. First, the material had several interesting properties that opened many opportunities for semiconductor device applications. Second, the glow discharge deposition technique enabled the production of *a*-Si:H films over a large area and at a low temperature. At present, this material is for instance used for photoconductive layers in electrophotography, for thin film transistors, and not in the least for solar cells.

Due to a high absorption coefficient of *a*-Si:H in the visible range of the solar spectrum, 1 micrometer (μm) thick *a*-Si:H layer is sufficient to absorb 90% of usable solar light energy. Low processing temperature allows using a wide range of low-cost substrates such as glass sheet, metal or polymer foil. These features has made *a*-Si:H a promising candidate for low-cost ***thin-film*** solar cells. Low-cost thin-film solar cells are regarded as the second-generation solar cells for terrestrial application.

Since the first *a*-Si:H solar cell made by Carlson and Wronski in 1976, which had an energy conversion efficiency of 2.4%[3], the *a*-Si:H solar technology has improved tremendously, leading to present solar cells with initial efficiencies exceeding 15%[4]. Today, amorphous silicon solar cell technology is a matured thin-film solar cell technology that delivered in 2002 *a*-Si:H modules with the total output power of 35.8 MW_p. This represented about 6% of the total PV module production in the world. Recently, experimental modules have been introduced which are based on a combination of *a*-Si:H solar cell and ***hydrogenated microcrystalline silicon* (*μc*-Si:H)** solar cells. A distinct feature of these solar cells is that all silicon-based layers are deposited in the low-temperature regime (T < 600ºC) by plasma assisted chemical vapour deposition techniques. Since in silicon solar cell technology the term "thin-film" usually covers a range of 1 to 100 micrometers thick layers, we refer to the low temperature silicon based solar cells as ***thin-film silicon*** (TF Si) solar cells.

7.2 Overview of thin-film silicon solar cell technology development

7.2.1 1970-ies

Carlson and Wronski announced the first experimental *a*-Si:H solar cell made at RCA Laboratory in 1976[3]. This single junction *p-i-n a*-Si:H solar cell deposited on a glass substrate coated with transparent conductive oxide (TCO) and aluminium back contact exhibited 2.4% conversion efficiency. In order to increase the output voltage of *a*-Si:H solar cells the concept of a stacked (also called multi-junction) solar cell structure was introduced[5]. A key step to industrial production was the development of a monolithically integrated type of *a*-Si:H solar cell[6]. Using the monolithic series integration of *a*-Si:H solar sub-cells, a desired output

[3] D.E. Carlson and C.R. Wronski, *Appl. Phys. Lett*. **28** (1976) p. 671-673.
[4] J. Yang, A. Banerjee, K. Lord, and S. Guha, *Proceedings of the 2nd World Conference and Exhibition on Photovoltaic Solar Energy Conversion*, Vienna, Austria, July6 – 10, 1998, p. 387-390.
[5] Y. Hamakawa, H. Okamoto, Y. Nitta, *Appl. Phys. Lett*. **35**(2) (1979), p. 187-189.
[6] Y. Kuwano, T. Imai, M. Ohnishi, and S. Nakano, in *Proceedings of the 14th IEEE Photovoltaic Specialist Conference* (1980), p. 1402.

voltage from a single substrate can be easily achieved. In 1980 the integrated type *a*-Si:H solar cells were commercialised by Sanyo and Fuji Electric and applied in consumer electronics, such as calculators and watches.

7.2.2 1980-ies

A large research activity in the field of *a*-Si:H solar cell was devoted to developing and optimising *a*-Si:H based alloys. A *p*-type hydrogenated amorphous silicon carbide (*a*-SiC:H) was implemented as a low-absorbing layer, usually denoted as a window layer[7], and a hydrogenated amorphous silicon germanium (*a*-SiGe:H) became an attractive low band gap material for stacked solar cells[8]. Surface-textured substrates for optical absorption enhancement were introduced[9]. The laboratory cells reached the initial efficiency in the range of 11 to 12%. Commercial single junction *a*-Si:H modules with efficiencies up to 5% were introduced to the market. The annual production capacity of *a*-Si:H solar cells and modules reached at the end of 1980-ies about 15 MW_p.

7.2.3 1990-ies

The research and manufacturing effort was directed towards achieving 10% stabilized module efficiency and a high throughput process. Several companies optimised and implemented an *a*-SiGe:H alloy in tandem (BP Solar[10], Sanyo[11], Fuji Electric[12]) and triple-junction (United Solar[13]) solar cell structures. The annual total production capacity for TF Si single- and multi-junction modules reached around 30 MW_p at the end of the 20th century.

Hydrogenated microcrystalline silicon deposited using the low-temperature PECVD technique emerged in this period as a new candidate for the low band gap material in multi-junction *a*-Si:H based solar cells. The University of Neuchâtel introduced a micromorph tandem solar cell in 1994, which comprised an *a*-Si:H top cell and a *μc*-Si:H bottom cell[14]. A promising potential of the micromorph cell concept was soon demonstrated by fabricating micromorph tandem and triple solar cells with stabilized efficiencies in the range of 11 to 12%[15],[16] and Kaneka Corporation started the development of micromorph module production technology[16]. The introduction and implementation of *μc*-Si:H in TF Si solar cells focused the

---

[7] Y. Tawada, H. Okamoto, Y. Hamakawa, *Appl. Phys. Lett*. **39**(3) (1981), p. 237-239.
[8] G. Nakamura, K. Sato, Y. Yukimoto, K. Shirahata, in *Proceedings of the 3rd E.C. Photovoltaic Solar Energy Conference* (1980), p. 835.
[9] H.W. Deckman, C.R. Wronski, H. Witzke, and E. Yablonovitch, *Appl. Phys. Lett*. **42**(11) (1983), p. 968.
[10] R.R. Arya and D.E. Carlson, *Progress in Photovoltaics: Research and Applications*, Vol. 10, 2002, p. 69-76.
[11] S. Okamoto. A. Terakawa, E. Maruyama, W. Shinohara, M. Tanaka and S. Kiyama, in *Amorphous and Heterogeneous Silicon-Based Films – 2001*, (Mater. Res. Soc. Proc., **664**, San Francisco, CA, 2001), A11.1.
[12] Y. Ichikawa, T. Yoshida, T. Hama, H. Sakai and K. Harashima, *Solar Energy Materials & Solar Cells*, 66 (2001) 107-115.
[13] S. Guha, J. Yang and A. Banerjee, *Progress in Photovoltaics: Research and Applications*, Vol. 8, 2000, p. 141-150.
[14] J. Meier, S. Dubail, R. Flückiger, D. Fischer, H. Keppner, A. Shah, in *Proceedings of the 1st World Conference on Photovoltaic Energy Conversion* (1994), p.409-412.
[15] J. Meier, S. Dubail, J. Cuperus, U. Kroll, R. Platz, P. Torres, J.A. Anna Selvan, P. Pernet, N. Beck, N. Pellaton Vaucher, Ch. Hof, D. Fischer, H. Keppner, A. Shah, *J. Non-Cryst. Solids* **227-230** (1998) 1250-1256.
[16] K. Yamamoto, M. Yoshimi, Y. Tawada, Y. Okamoto, A. Nakajima, *J. Non-Cryst. Solids* **266-269** (2000) 1082-1087.

attention upon the increase of the deposition rate. Several new deposition methods[17] have been investigated for fabrication of solar cells at high deposition rates (0.5 to 1.0 nm/s), such as very high frequency and microwave PECVD, hot wire CVD, and expanding thermal plasma CVD.

7.3 Hydrogenated amorphous silicon

In order to understand design and operation of an *a*-Si:H solar cell, which is different from a crystalline silicon (c-Si) cell, the material properties of *a*-Si:H are summarised and compared to the single crystal silicon.

7.3.1 Atomic structure

Figure 7.1 illustrates the difference in the atomic structure between single crystal silicon and *a*-Si:H. Figure 7.1a shows the structure of single crystal silicon schematically. Each Si atom is covalently bonded to four neighbouring Si atoms. All bonds have the same length and the angles between the bonds are equal. The number of bonds that an atom has with its immediate neighbours in the atomic structure is called the ***coordination number*** or ***coordination***. Thus, in single crystal silicon, the coordination number for all Si atoms is four; we can also say that Si atoms are fourfold coordinated. A ***unit cell*** can be defined, from which the crystal lattice can be reproduced by duplicating the unit cell and stacking the duplicates next to each other. Such a regular atomic arrangement is described as a structure with ***long range order***. A diamond lattice unit cell represents the real lattice structure of single crystal silicon.

Figure 7.1b illustrates that *a*-Si:H does not exhibit the structural order over a long-range as is the case for single crystal silicon. Nevertheless, there is a similarity in atomic configuration on a local atomic scale, where most Si atoms have covalent bonds with four neighbours. The *a*-Si:H has the same ***short-range order*** as the single crystal silicon but it lacks the long range order. The small deviations in bonding angles and bonding lengths between the neighbouring atoms in *a*-Si:H lead to a complete loss of the locally ordered structure on a scale exceeding a few atomic distances. The resulting atomic structure of *a*-Si:H is called the ***continuous random network***. Due to the short-range order in the continuous random network of *a*-Si:H, the common semiconductor concept of the energy states bands, represented by the conduction and valence bands, can still be used.

The larger deviations in bonding angles and bonding lengths between the neighbouring atoms in *a*-Si:H result in the so-called ***weak*** or ***strained bonds***. The energy of the weak bonds is higher than the energy of optimal silicon covalent bonds in ideal single crystal silicon. Therefore, the weak bonds can easily break and form ***defects*** in the atomic network. We note that in the continuous random network, the definition of a defect is modified with respect to the crystal structure. In a crystal any atom that is out of place in a lattice forms a defect. In the continuous random network an atom cannot be out of place. Because the only specific structural feature of an atom in the continuous random network

[17] R.E.I. Schropp and M. Zeman, *Amorphous and Microcrystalline Solar Cells: Modeling, Materials, and Device Technology*, Kluwer Academic Publishers, 1998.

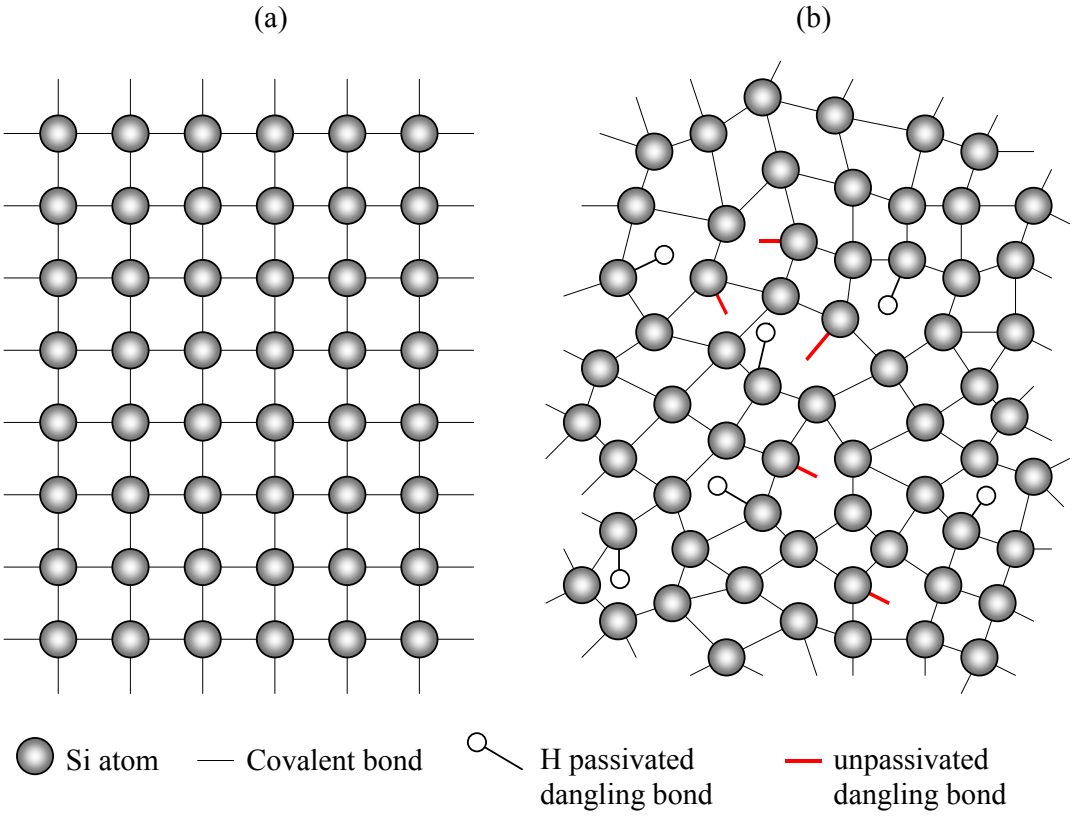

Figure 7.1. Schematic representation of the atomic structure of (a) single crystal silicon (b) hydrogenated amorphous silicon.

is the coordination to its neighbours, a defect in *a*-Si:H is the ***coordination defect***. This happens when an atom has too many or too few bonds. In *a*-Si:H the defects are mainly represented by Si atoms that are covalently bonded to only three Si atoms (***threefold coordinated***) and have one unpaired electron, a so-called ***dangling bond***. Since this configuration is the dominant defect in *a*-Si:H, the defects in *a*-Si:H are often related to the dangling bonds.

When amorphous silicon is deposited in such a way that hydrogen can be incorporated in the network (as in the case of glow discharge deposition from silane), then the hydrogen atoms bond with most of the dangling bonds. We say that the dangling bonds are ***passivated*** by hydrogen. Hydrogen passivation reduces the dangling bond density from about 10^{21} cm^{-3} in pure *a*-Si (amorphous silicon that contains no hydrogen) to 10^{15}-10^{16} cm^{-3} in *a*-Si:H, i.e. less than one dangling bond per million Si atoms. In Fig. 1b some of the defects with un-passivated dangling bonds and with hydrogen passivated dangling bonds are depicted. Device quality *a*-Si:H contains from 1 to 10 atomic percent of hydrogen. In summary, the short range order in *a*-Si:H network and the hydrogen passivation of the dangling bonds are responsible for semiconductor properties of amorphous silicon.

7.3.2 Density of energy states

The difference in the atomic structure between single crystal silicon and *a*-Si:H leads to the different distributions of density of allowed energy states as schematically illustrated in Figure 7.2. The periodic atomic structure of single crystal silicon results in the ranges of allowed energy states for electrons that are called ***energy bands*** and the excluded energy ranges, ***forbidden gaps*** or ***band gaps***. Figure 2a shows schematically the distribution of density of states for single crystal silicon, in which the valence band and the conduction band are separated by a well-defined band gap, E_g. At room temperature single crystal silicon has a band gap of 1.12 eV. In case of an ideal crystal, there are no allowed energy states in the band gap.

As Figure 7.2b demonstrates, in case of *a*-Si:H, there is a continuous distribution of density of states and no well defined band gap exists between the valence band and the conduction band. Due to the long range order disorder in the atomic structure of *a*-Si:H the energy states of the valence band and the conduction bands spread into the band gap and form regions that are called ***band tail*** states. The band tail states represent the energy states of electrons that form the strained bonds in the *a*-Si:H network. The width of the band tails is a measure for the amount of disorder in *a*-Si:H material. More disorder in *a*-Si:H means that the band tails are broader. In addition, the dangling bonds introduce allowed energy states that are located in the central region between the valence band and conduction band states.

The electron and hole wavefunctions that extend over the whole structure are characteristic for energy states, in which the charge carriers can be considered as free carriers. These states are non-localised and are called ***extended states***. The wavefunctions of the tail and defect states are localized within the structure and therefore these states are called ***localised states***. Consequently, mobility that characterises transport of carriers through the

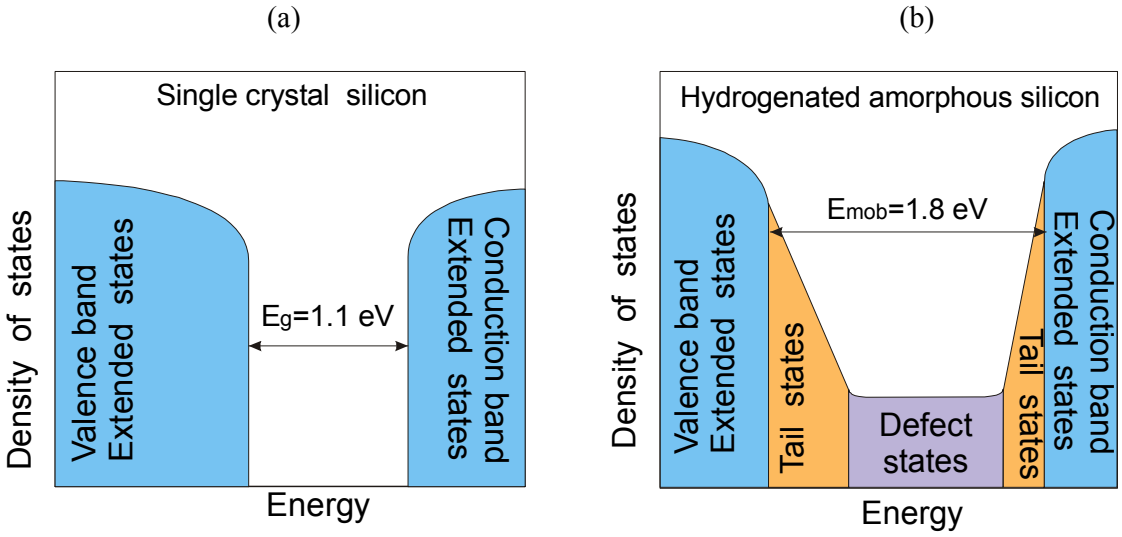

Figure 7.2. The schematic representation of the distribution of density of allowed energy states for electrons for (a) single crystal silicon (b) *a*-Si:H.

localised states is strongly reduced. This feature of a sharp drop of mobility of carriers in the localised states in *a*-Si:H is used to define its band gap. This band gap is denoted by the term ***mobility gap***, E_{mob}, because the presence of a considerable density of states in this gap conflicts the classical concept of the band gap. The energy levels that separate the extended states from the localised states in *a*-Si:H are called the valence band and the conduction band mobility edges. The mobility gap of *a*-Si:H is larger than the band gap of single crystal silicon and has a typical value of 1.8 eV. The localised tail and dangling bond states have a large effect on the electronic properties of *a*-Si:H. The tail states act as trapping centres and build up a space charge in a device, the dangling bond states act as very effective recombination centres and affect in particular the lifetime of the charge carries.

7.3.3 Optical properties

The optical properties of *a*-Si:H are usually characterised by its ***absorption coefficient*** and a value of the ***optical band gap***. Figure 7.3a shows the absorption coefficient of *a*-Si:H that is fabricated at Delft University of Technology as a function of photon energy. The absorption coefficient of c-Si is shown for reference. This figure demonstrates that *a*-Si:H absorbs almost 100 times more than c-Si in the visible part of the solar spectrum. The higher absorption is due to the disorder in the atomic structure of *a*-Si:H that behaves like a direct gap semiconductor. This means that 1 μm thick *a*-Si:H layer is sufficient to absorb 90% of usable solar light energy. In practice the thickness of *a*-Si:H solar cells is less than 0.5 μm that is about 100 times less than the thickness of a typical single crystal silicon cell. This results in important savings in both material and energy in fabrication of *a*-Si:H solar cells.

Another advantage of *a*-Si:H is that the optical absorption can be slightly changed by varying its hydrogen content, and it can be greatly changed by ***alloying*** with carbon or germanium. The absorption coefficient of hydrogenated amorphous silicon carbide (*a*-SiC:H) and hydrogenated amorphous silicon germanium (*a*-SiGe:H) that are fabricated at Delft University of Technology are also shown in Figure 7.3a. This feature of easy alloying of *a*-Si:H allows to design solar cell structures in which *a*-Si:H based materials with different absorption properties can be used as active layers.

From the absorption coefficient of *a*-Si:H based materials, the so called optical band gap is determined. The optical band gap is a useful material parameter that allows comparison of *a*-Si:H based materials regarding their light absorption properties. In general, a material with higher optical band gap absorbs less. The optical band gap, E_{opt}, is determined by extrapolating a linear part of the following function $\left[\alpha(E)\times n(E)\times E\right]^{1/(1+p+q)}$ vs the photon energy E to $\alpha(E)=0$, for $\alpha \geq 10^3$ cm^{-1}:

$$\left(\alpha(E)\times n(E)\times E\right)^{1/(1+p+q)} = B\left(E - E_{opt}\right) \qquad (7.1)$$

where $\alpha(E)$ is the absorption coefficient, $n(E)$ is the refractive index, p and q are constants that describe the shape of the density of extended states distribution for the conduction band and valence band, respectively, and B is a prefactor. When the density of states distribution near the band edges has a square-root energy dependence (p=q=1/2), as is commonly the case in crystalline semiconductors, Eq. 1 describes the so-called Tauc plot and the corresponding

(a) (b)

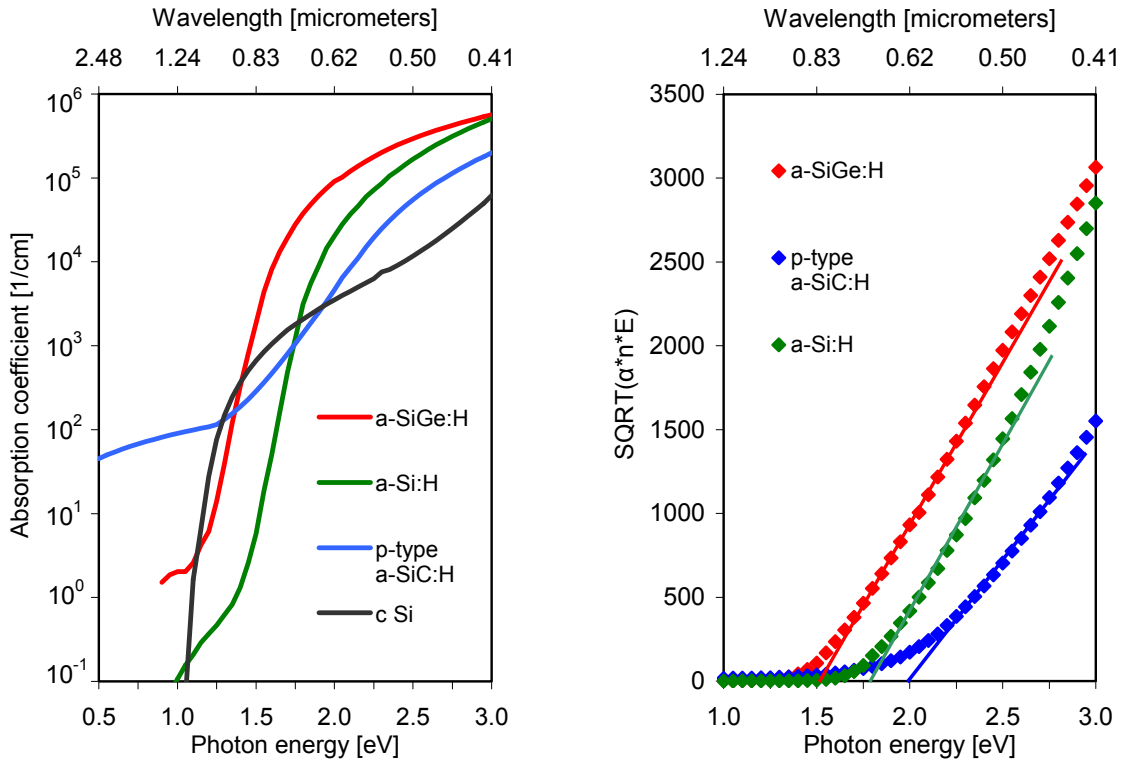

Figure 7.3. (a) Absorption coefficient as function of photon energy for *a*-Si:H, *p*-type *a*-SiC:H and *a*-SiGe:H fabricated at Delft University of Technology. The absorption coefficient of c-Si is shown for reference. (b) Tauc plot with linear extrapolation to determine the Tauc optical band gap for *a*-Si:H, *p*-type *a*-SiC:H and *a*-SiGe:H.

optical band gap is called the ***Tauc optical gap***. When the distribution near the band edges is assumed to be linear (p=q=1) E_{opt} is called the ***cubic optical gap***. The Tauc gap of device quality intrinsic *a*-Si:H is in the range of 1.70 to 1.80 eV, the cubic gap of the same material is usually 0.1 to 0.2 eV smaller than the Tauc gap. The Tauc plot with linear extrapolation to determine the Tauc optical gap for *a*-Si:H (E_{opt}=1.77 eV), *p*-type *a*-SiC:H (E_{opt}=1.95 eV), and *a*-SiGe:H (E_{opt}=1.52 eV) is shown in Figure 7.3b.

7.3.4 Electrical properties

The electrical properties of *a*-Si:H are usually characterised in terms of dark conductivity and photoconductivity. The measurement of these two properties is a standard approach to obtain information about the quality of *a*-Si:H material for application in solar cells. Also it gives information about the mobility-lifetime product and the influence of impurities in *a*-Si:H. The mobilities of the charge carriers in the extended states of *a*-Si:H are about two orders of magnitude lower than in single crystal silicon. Typically, the electron mobility is 10 cm^2/Vs, and the hole mobility is 1 cm^2/Vs in intrinsic *a*-Si:H. The low values

of electron and hole mobilities and the high mobility gap of *a*-Si:H result in a low dark conductivity, which in device quality intrinsic *a*-Si:H is less than 1×10^{-10} Ω^{-1} cm^{-1}. This material is further characterised by an excellent photoconductivity that is higher than 1×10^{-5} Ω^{-1} cm^{-1}, when measured using the AM1.5 light spectrum and the incident power of 100 mW/cm^2.

7.3.5 Doping of *a*-Si:H

The purpose of doping is to manipulate the type of electrical conductivity and its magnitude by adding a controlled amount of special impurity atoms. The principal doping elements used in *a*-Si:H are the same as in crystalline silicon: boron for *p*-type and phosphorus for *n*-type material. The doped layers have two functions in an *a*-Si:H solar cell. First, they set up an internal electric field across the active intrinsic *a*-Si:H layer. The electric field should be high enough to ensure that the photo-generated carriers in intrinsic *a*-Si:H layer are collected. The strength of the electric field depends on the level of doping in the doped layers and the thickness of the intrinsic layer. Second, they establish low-loss ohmic electrical contacts between the *a*-Si:H part of solar cell and the external electrodes.

Spear and LeComber from Dundee University reported in 1975 that amorphous silicon could be doped by addition of boron and phosphorus. They achieved the change in conductivity of *a*-Si:H by mixing the silicon source gas, silane (SiH_4), with phosphine (PH_3) or diborane (B_2H_6) during the deposition using the glow discharge method. Figure 7.4 shows the room temperature conductivity, σ_{RT}, of their *a*-Si:H as a function of fraction of doping gases in a mixture with silane[2]. The conductivity of *a*-Si:H could be varied by more than a factor 10^8. The activation energy decreases from 0.7 - 0.8 eV in intrinsic material to about 0.15 eV in phosphorus doped material and 0.3 eV in boron doped material.

The demonstration of effective doping of *a*-Si:H was an important breakthrough, because the researchers believed for a long time that the effective doping of amorphous silicon could not be achieved. They assumed that the continuous random network could easily incorporate impurity atoms, such as phosphorus and boron, with coordination that corresponded to the bonding configuration with the lowest energy. This property of the continuous random network is in contrast to the crystalline structure, in which, due to the long range order, the impurity atoms are forced to adopt the coordination of the host atoms. In the continuous random network the optimum number of covalent bonds (coordination), *Z*, for an atom with *N* valence electrons is,

$Z = 8 - N$ for $N \geq 4$
$Z = N$ for $N < 4$.

This prediction of the atom coordination in the continuous random network is known as the ***8-N rule*** and was introduced by Mott in 1969[18].

[18] N.F. Mott, *Philos. Mag.* **19** 835 (1969).

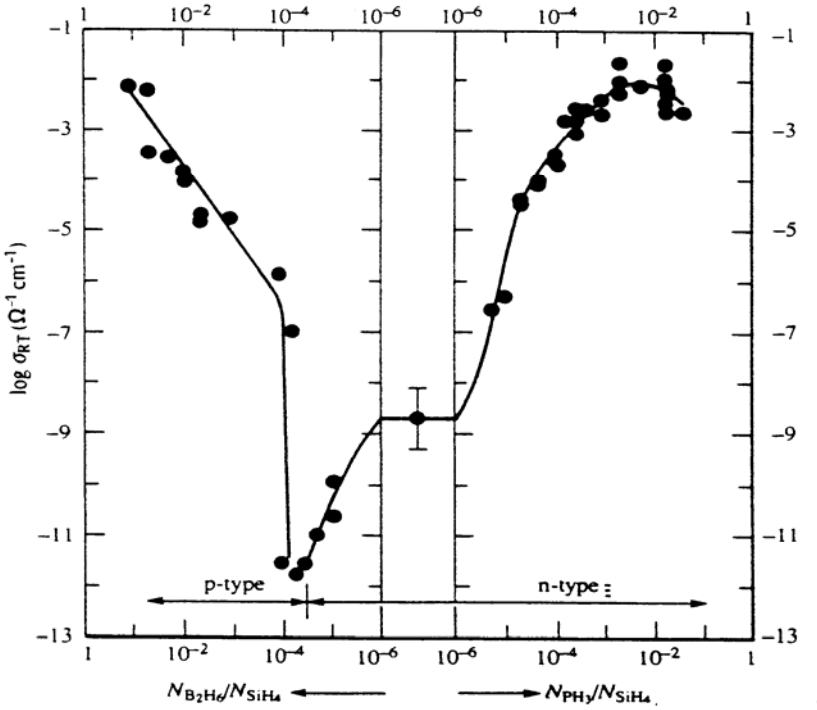

Figure 7.4. Room-temperature conductivity σ_{RT} of *n*- and *p*-type amorphous silicon, plotted as a function of the ratio between the numbers of doping gases molecules and silane molecules in the gas mixture[2].

For example, following the *8-N* rule a phosphorus atom with five valence electrons would incorporate itself in the continuous random network by forming three covalent bonds with neighbouring atoms. This situation is illustrated in Figure 7.5a. In order to describe the configuration of the atoms in the structural network notation T_z^q is used. T is the atom, z is the coordination number, and q is the charge state of the atom. P_3^0 denotes a phosphorus atom that is covalently bonded to three neighbouring atoms and is neutral. In *a*-Si:H most of the phosphorus atoms are incorporated according to the *8-N* rule. They adopt the optimal threefold coordination that represents the ***non-doping state*** and thus is electrically inactive. The doping efficiency in *a*-Si:H, which is defined as the fraction of dopant atoms with fourfold coordination, is rather low. In comparison to single crystal silicon, where the doping efficiency at room temperature is almost unity, it is in the range of 10^{-2} - 10^{-3} in *a*-Si:H. This means that relatively high concentrations of phosphorous atoms must be introduced in order to obtain material with high conductivity. A phosphorous atom can also be incorporated as the neutral donor P_4^0 in the network as it is the case in single crystal silicon (see Figure 7.5c), but this configuration is characterised by much higher energy than the optimal P_3^0 configuration and therefore is unstable in the continuous random network. Most of the phosphorous atoms, which contribute to doping, are not P_4^0 neutral donors, but charged phosphorus atoms P_4^+. The formation of the P_4^+ charged state is accompanied by formation of negatively charged dangling bond Si_3^- as it is illustrated in Fig. 5b. The P_4^+ and Si_3^- configuration is energetically more favourable than P_4^0 donor and is called the ***defect-compensated donor***.

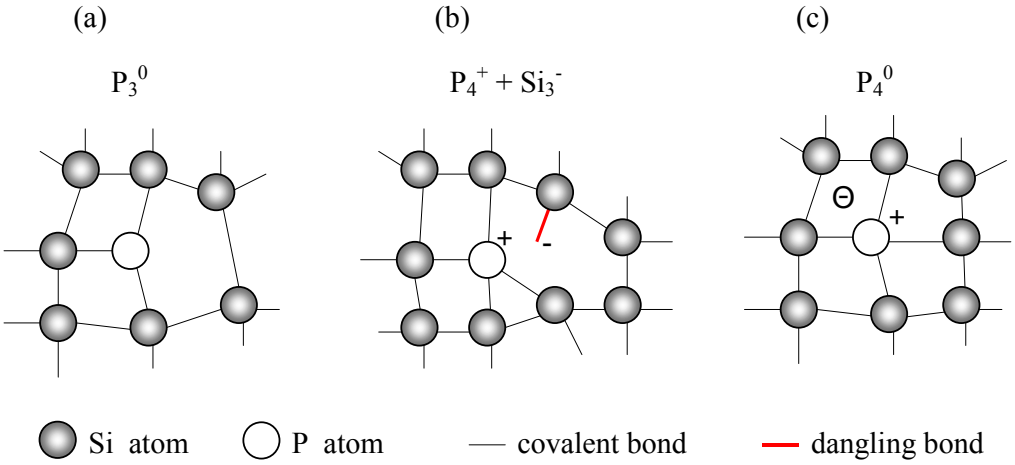

Figure 7.5. Possible configurations of a phosphorous atom in *a*-Si:H network. (a) the non-doping state P_3^0, (b) the defect-compensated donor state $P_4^+ + Si_3^-$, (c) the neutral donor P_4^0.

The formation of the defect-compensated donors in the case of phosphorus atoms and defect compensated acceptors in the case of boron atoms is the major doping mechanism in *a*-Si:H. This mechanism was explained by Street and it is known as the ***autocompensation model***[19]. The most important result of this model is that doping of *a*-Si:H inevitably leads to creation of dangling bonds. Doped *a*-Si:H has two or three orders of magnitude larger defect density in comparison to intrinsic *a*-Si:H. The diffusion length of charge carriers in doped *a*-Si:H is very small compared to single crystal silicon. For this reason *a*-Si:H solar cells cannot function successfully as a *p*-*n* junction but a relatively defect free intrinsic layer has to be inserted between the *p*-type and *n*-type layers. Because the underlying processes of the photovoltaic effect such as absorption of light and separation of photo-generated carriers take place in the intrinsic layer, this layer is called an active layer in *a*-Si:H solar cell.

An additional important difference between *a*-Si:H and single crystal silicon is that when increasing the concentration of boron and phosphorous doping atoms in a-Si:H, the Fermi level does not move closer to the valence band mobility edge than 0.30 eV and 0.15 eV to the conduction band mobility edge, respectively. The reason for this is that the shift of the Fermi level towards the band edges decreases the probability of forming the doping state configurations and favours the non-doping configurations. Further, when the Fermi level is shifted towards the band edges it is located in the band tail states, which density increases exponentially towards the mobility band edges. Therefore any further shift towards the band edges is accompanied by building up of a large space charge in the tail states that compensates the charge created by ionised doping atoms.

[19] R.A. Street, *Phys. Rev. Lett.* **49** 1187 (1982).

7.4 Hydrogenated microcrystalline silicon

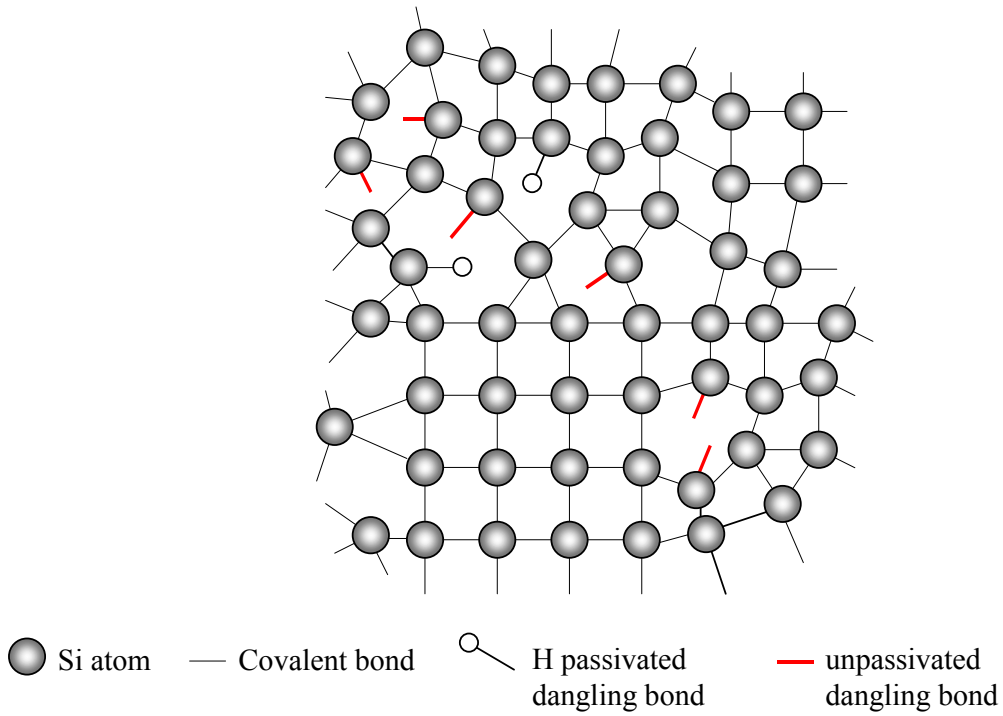

This figure shows a schematic structural representation of hydrogenated microcrystalline silicon (μc-Si:H). Small crystals of highly ordered material in the range of tenths of nanometres are imbedded in the amorphous structure.

7.5 Deposition of thin-film silicon

The methods that are used for depositing thin films of *a*-Si:H and *μc*-Si:H can be divided in two groups. The first group includes methods that form *a*-Si:H and *μc*-Si:H from a gas phase by decomposition of silicon-bearing gas, usually SiH_4. These methods are known as ***chemical vapour deposition*** (CVD) methods. The second group represents the physical deposition methods in which silicon atoms for *a*-Si:H growth are obtained by sputtering a silicon target.

7.5.1 Plasma Enhanced Chemical Vapour Deposition

The most commonly used deposition method to produce "device quality" *a*-Si:H, both on the laboratory and industrial scale, is the radio frequency (13.56 MHz) plasma decomposition of SiH_4, known as the Plasma Enhanced CVD (rf PECVD) method or the glow discharge (GD) deposition. The PECVD deposition system is schematically shovn in Figure 7.6. The role of the plasma is to provide a source of energy to dissociate the SiH_4 molecules. This is done by collisions with electrons, which originate as secondary electrons in the plasma and build up their energy by acceleration in an electric field. The growth of an *a*-Si:H film is accomplished by attachment of reactive particles of dissociated SiH_4 molecules, called radicals, to the surface of the growing film. As the thickness of the *a*-Si:H film for device applications is around half a micrometer, *a*-Si:H must be deposited on an appropriate substrate carrier. Some of the energy transferred to the SiH_4 molecules in the collisions with electrons is radiated as visible light, hence the deposition method is also called the glow discharge.

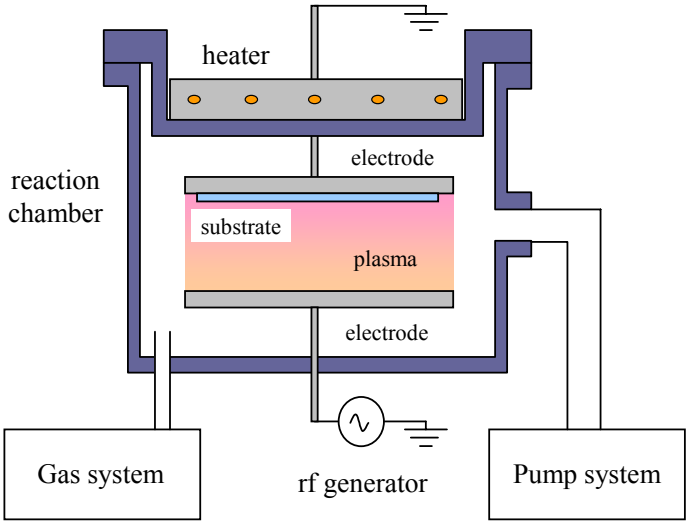

Figure 7.6. The schematic representation of a rf PECVD deposition system.

The PECVD deposition system is relatively simple and consists of five main parts (see Figure 7.6):

- reaction chamber with the capacitatively coupled parallel electrodes
- vacuum pump system
- gas handling system
- dc or rf power source
- substrate heating assembly

The deposition temperature of device quality *a*-Si:H is usually between 200°C and 250°C. This temperature range allows using a wide range of low cost substrates (glass, stainless steel, flexible plastic foils, or ceramic). The deposition process can be scaled up to large area substrates (more than 1 m^2). However, scaling requires a careful design of reactor geometry in order to produce uniform and homogeneous films. Doping and alloying of *a*-Si:H is simply accomplished by adding appropriate gases to the source gas mixture. For instance, in order to make *p*-type material B_2H_6 is added to the gas mixture and boron is incorporated in the material, for *n*-type material PH_3 is used in the gas mixture. Adding germane (GeH_4) or methane (CH_4) to the gas mixture results in *a*-SiGe:H material with a lower optical band gap or *a*-SiC:H material with higher optical band gap, respectively.

The advantages of fr PECVD deposition technology are briefly summarised:

- large area deposition (more than 1 m^2)
- low deposition temperature (100°C < T_s < 400°C)
- use of any cheap and arbitrarily shaped substrates
- effective *p*- and *n*-type doping and alloying
- deposition of composition-graded layers
- deposition of multi-layer structures by control of gas mixtures in a continuous process
- easy patterning and integration technology
- low cost
- good mass-producibility

7.5.2 High deposition rate techniques

At present *a*-Si:H solar cells are mainly produced by the rf PECVD process. This process has also been successfully applied for the mass production of large area solar cells. A drawback of the rf PECVD technique is a relatively low deposition rate. The device quality material that is required for high-efficiency solar cells is obtained at a typical deposition rate of 2-5 Å/s. However, for high volume production it is somewhat low and therefore considerable research effort is devoted to high-rate deposition methods of *a*-Si:H layers. Several novel deposition methods are investigated, e.g., hot filament assisted CVD, known also as hot wire CVD (HW-CVD) technique at Utrecht University and the expanding thermal plasma CVD (ETP-CVD) technique developed at Eindhoven University of Technology.

HW CVD is based on the dissociation of a gas by catalytic action of a hot filament. Similar deposition systems can be used as in case of rf PECVD in Fig. 7.6; only the reaction chamber is modified. Instead of two parallel electrodes, filaments are introduced into the chamber and placed in the vicinity of the substrate holder. The filaments are made of tungsten or tantalum. The decomposition of SiH_4 into single silicon and hydrogen radicals is efficient

for filament temperatures above 1600°C. The a-Si:H layers are typically deposited at 250°C to 350°C with a deposition rate of 10 Å/s.

The ETP deposition set-up is shown in Figure 7.7a. The set-up consists of a dc thermal-arc plasma source and a low-pressure deposition chamber. The plasma generation and film deposition are separated and this system is therefore regarded as a remote-plasma system. The plasma is generated in a gas mixture of argon and hydrogen by a dc discharge (typically 50 A, 100 V). The pressure in the plasma source is ~200 mbar, from which the plasma expands supersonically into the deposition chamber, where the pressure is typically 0.2 mbar. Pure SiH_4 is injected into the plasma jet just behind the expansion nozzle. The deposition rate is dependent on a number of factors, such as the pressure in the deposition chamber and SiH_4 flow, and can reach 1000 Å/s. In order to employ the ETP deposition method for *a*-Si:H solar cells, at Delft University of Technology a system has been built, called CASCADE, in which a complete solar cell can be fabricated. The system consists of three chambers: an rf PECVD chamber for the deposition of the doped layers, an ETP chamber for the high-rate deposition of the intrinsic layer, and a load-lock. The ETP deposition chamber is shown in Figure 7.7b. The doped layers are produced using PECVD, because an accurate control of the thickness of these layers is essential and thus a fairly low deposition rate is desired.

(a) (b)

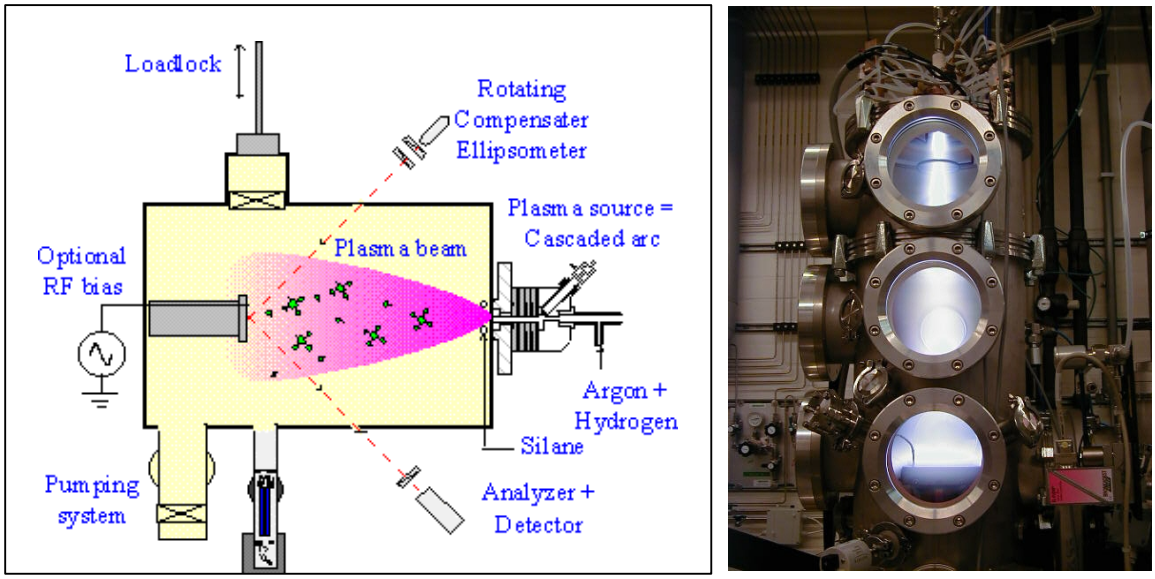

Figure 7.7. (a) A schematic representation of the ETP deposition system. (b) A photograph of the ETP chamber of the CASCADE deposition system at Delft University of Technology during operation.

7.6 Thin-film silicon solar cells

7.6.1 Comparison of c-Si and *a*-Si:H solar cells

There is a fundamental difference between c-Si and *a*-Si:H solar cells. A typical c-Si solar cell, shown in Figure 7.8a, consists of a *p*-type wafer, which is 300 to 500 μm thick, with a thin *n*-type layer on the top of the wafer, which forms a *p*-*n* junction. The width of the depletion region of the *p*-*n* junction is less than 0.5 μm. The depletion region, where an internal electric field is created, represents only a tiny part of the wafer. Most electron-hole pairs are generated in the bulk of the electrically neutral *p*-type region. Electrons, which are the minority carriers in the *p*-type region, diffuse towards the *p*-*n* junction and in the depletion region of the junction the electrons drift to the *n*-type layer under the influence of the internal electric field. This solar cell is called a ***diffusion device*** because the dominant transport mechanism of the photo-generated carriers is diffusion. Therefore, the diffusion length of minority carriers (i.e. electrons in *p*-type material) is an important material parameter that determines design and performance of c-Si solar cells. Typical values of the diffusion length of electrons in the *p*-type float zone single crystal silicon wafers are in the range of 250 μm to 700 μm. These values correspond to wafers with a resistivity in the range of 0.25 to 1.0 Ω cm, respectively.

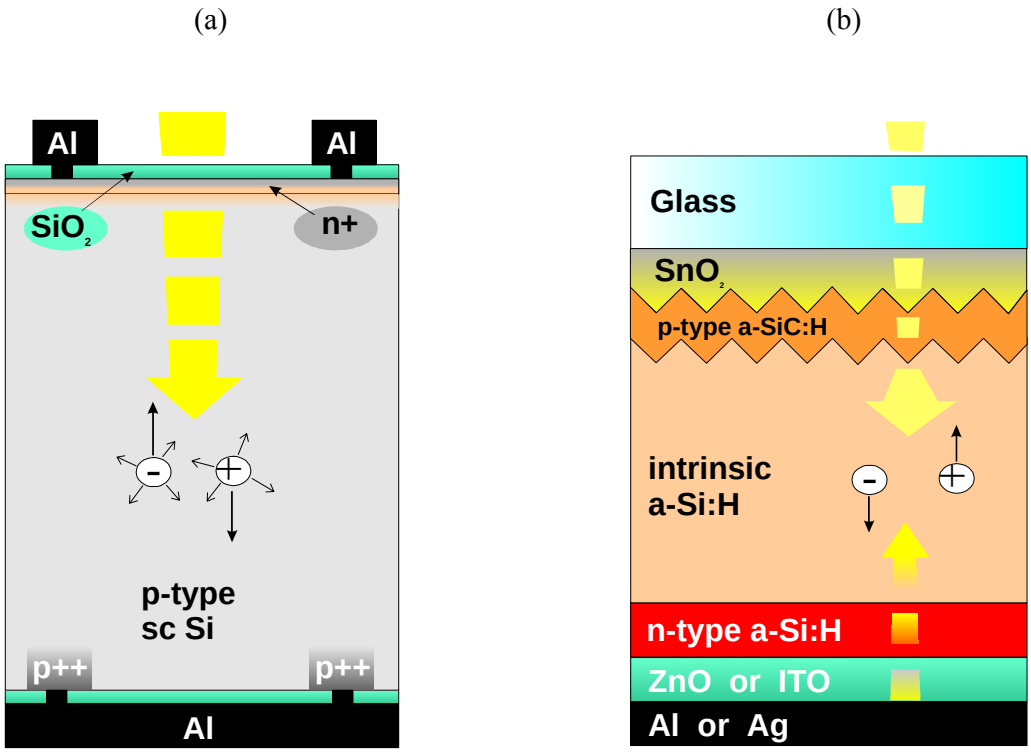

Figure 7.8. A typical structure of (a) c-Si solar cell and (b) *a*-Si:H solar cell.

In *a*-Si:H the diffusion length of the charge carriers is much shorter than in single crystal silicon. In device quality intrinsic *a*-Si:H the ambipolar diffusion length ranges from 0.1 to 0.3 μm. In doped *a*-Si:H layers, in which the defect density due to the doping is two or three orders of magnitude higher than in the intrinsic *a*-Si:H, the diffusion length of the minority carriers is much lower. A solar cell structure based on the diffusion of the minority carriers in the electrically neutral regions of the doped layers as in the case of c-Si does not work in the case of *a*-Si:H. The photo-generated carriers would all recombine in the doped layers before reaching the depletion region of the *p*-*n* junction due to the very short diffusion length. Therefore, an *a*-Si:H solar cell is designed differently. A schematic lay-out of an *a*-Si:H solar cell is shown in Figure 7.8b. The active device consists of three layers: a *p*-type *a*-SiC:H layer, an intrinsic *a*-Si:H layer, and an *n*-type *a*-Si:H layer. The doped layers are usually very thin, a *p*-type *a*-SiC:H layer is ~10 nm thick and an *n*-type *a*-Si:H is ~20 nm thick. The active layer in the *a*-Si:H solar cell is the intrinsic layer which is typically 300 to 500 nm thick. This intrinsic layer is sandwiched in between the doped layers so that an internal electric field is present across the intrinsic layer. The electron-hole pairs that are generated in the intrinsic *a*-Si:H layer immediately experience the internal electric field that separates electrons and holes from each other. The separated carriers drift under the influence of the internal electric field towards the doped layers (electrons towards the *n*-type layer and holes towards the *p*-type layer) and are collected by the electrodes. The dominant transport mechanism of the photo-generated carriers is drift in the internal electric field and therefore an *a*-Si:H solar cell is called a ***drift device***. A stack, which consists of *p*-type *a*-SiC:H, intrinsic *a*-Si:H and *n*-type *a*-Si:H layers, forms the *p*-*i*-*n* junction. This structure of *a*-Si:H solar cell is presented in Figure 7.8b and it is generally called a ***single junction*** *a*-Si:H solar cell. The band diagrams of c-Si and single junction *a*-Si:H solar cells are presented in Figure 7.9a and 7.9b, respectively, which also demonstrate the difference between the diffusion type and the drift type solar cell.

The thickness of the *a*-Si:H solar cell is comparable to the thickness of the depletion region in the crystalline silicon solar cell, i.e. about 0.5 μm. As mentioned earlier, this small thickness is sufficient for absorption of the visible part of solar radiation. The small thickness implies a large reduction in material and energy consumption during production when compared to crystalline silicon solar cells. Furthermore, when deposited on a light substrate such as a flexible foil the weight of *a*-Si:H solar modules is strongly decreased. This is desired specifically in space applications. The thicknesses of individual layers in c-Si and *a*-Si:H solar cells are compared in Table 7.1.

Table 7.1. Comparison of the thicknesses of individual layers in c-Si and *a*-Si:H solar cells.

Crystalline silicon solar cell		***a*-Si:H solar cell**	
Al contact	0.5 to 1.0 μm	top glass	2 to 4 mm
SiO_2 or Si_3N_4 layer	~0.1 μm	transparent electrode	0.5 to 0.9 μm
n^+-type emitter	0.3 to 0.5 μm	*p*-type *a*-SiC:H	0.01 μm
***p*-type base**	300 to 500 μm	**intrinsic *a*-Si:H**	0.3 to 0.5 μm
p^{++}-type region	1.0 μm	*n*-type *a*-Si:H	0.02 μm
SiO_2 layer	0.05 to 0.1 μm	ZnO or ITO layer	~0.1 μm
Al contact	0.5 to 1.0 μm	Al or Ag contact	0.5 to 1.0 μm

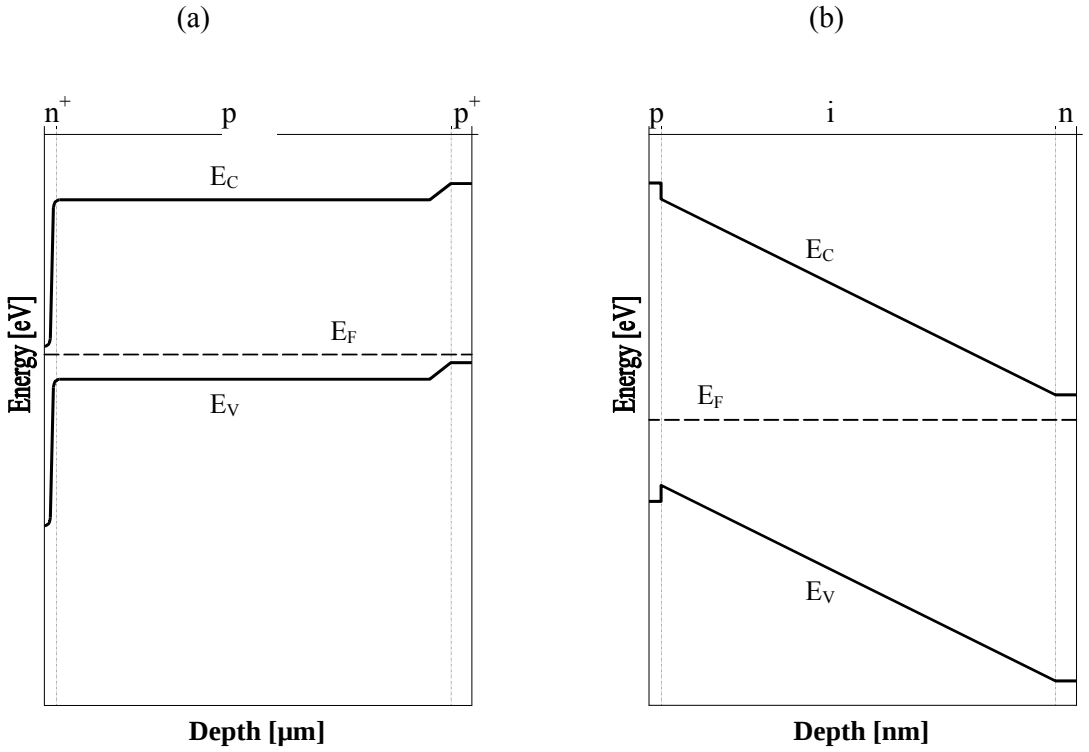

Figure 7.9. Band diagram of (a) c-Si solar cell and (b) single junction *a*-Si:H solar cell.

Figure 7.10 shows both the dark and illuminated *J-V* characteristics of the crystalline Si and a-Si:H solar cells. The difference between a diffusion type device and a drift type device is reflected in the behaviour of the dark and illuminated *J-V* curves as illustrated in Figure 7.10. In crystalline Si solar cells, the carriers, which are generated outside the depletion region of the solar cell, determine the photocurrent. These are carriers that are generated in the bulk of a wafer, which is electrically neutral. Therefore, the photocurrent is almost independent on the applied voltage. In forward bias, the total current of the solar cell under illumination, which is a sum of the photocurrent and the dark current, is smaller than the dark current. Therefore, the dark and illuminated curves do not cross. In the case of *a*-Si:H solar cells, the photocurrent is determined by the carriers generated in the intrinsic layer of the cell, which is part of the depletion region of the solar cell. The photocurrent, that is mostly the drift current, depends on the electric field in the depletion region and therefore also on the applied voltage. At a certain forward bias voltage, V_T, the photocurrent is zero. For voltages higher than V_T the electric field in the depletion region is reversed, as a result of which the photocurrent is added to the dark current. The resulting total current of the solar cell is higher than the dark current and the dark and illuminated curves cross.

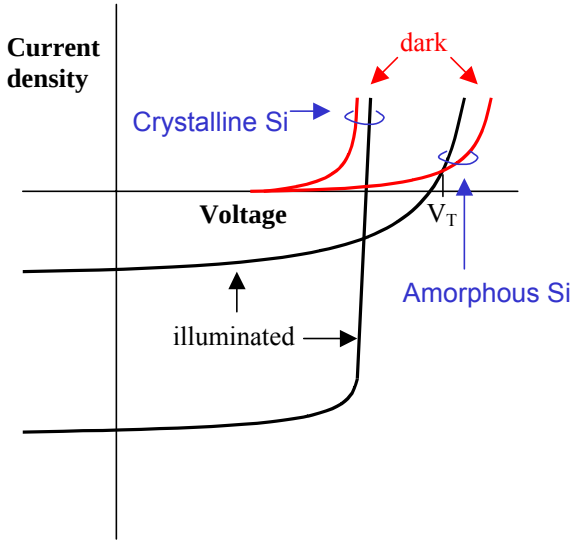

Figure 7.10. The dark and illuminated *J-V* characteristics of the c-Si and *a*-Si:H solar cells.

Figure 7. 11 shows the difference in the J-V characteristics of a crystalline Si solar cell and an *a*-Si:H solar cell measured under standard AM1.5 illumination conditions. Both J-V curves represent the best results in the field of crystalline Si and *a*-Si:H solar cells at present and are achieved by the University of New South Wales (UNSW) in Australia and United Solar Systems Corporation (USSC) from the United States of America, respectively. The external parameters of the cells are reported in Table 2. It should be noted that the crystalline Si solar cell generates a very high short circuit current in comparison to *a*-Si:H solar cell and also the fill factor is higher. On the other hand due to a higher band gap the *a*-Si:H solar cell achieves a higher open circuit voltage.

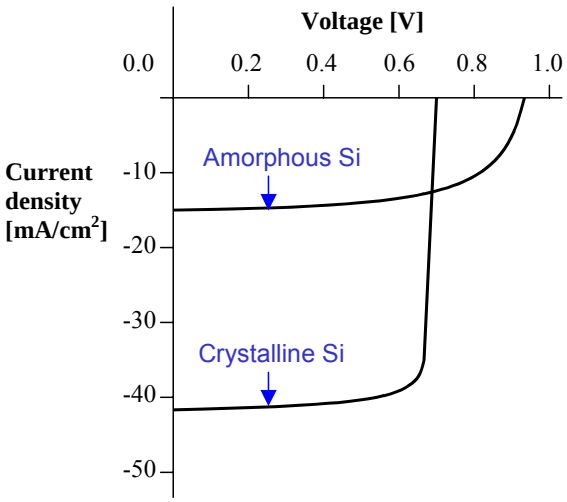

Figure 7. 11. The J-V characteristics of the c-Si and the single junction a-Si:H solar cells. The external parameters of the solar cells are in Table 2.

Table 2. The external parameters of the best laboratory crystalline Si and a-Si:H solar cells.

	J_{sc} [mA/cm^2]	V_{oc} [V]	Fill factor	Efficiency [%]
UNSW mono c-Si PERL structure	42.2	0.706	0.828	24.7
USSC *a*-Si:H p-i-n structure	14.3	0.965	0.672	9.3

7.6.2 Single junction *a*-Si:H solar cell

A typical a-Si:H solar cell is represented by a single junction solar cell. There are two configurations of the single junction a-Si:H solar cell, namely the ***p-i-n superstrate*** configuration and the ***n-i-p substrate*** configuration. The type of configuration reflects the deposition sequence of the *a*-Si:H based layers. In the *p-i-n* configuration the *p*-type layer is deposited first, then the intrinsic layer and the *n*-type layer is deposited as the last one. In the *n-i-p* configuration the sequence of the deposition is vice versa. When glass or another transparent material is used as a substrate, the *p-i-n* configuration is used. In case of a stainless steel or another non-transparent material, the *n-i-p* deposition sequence is applied. The reason for these two approaches is that the light enters the bulk of a solar cell through the *p*-type layer. This will be explained below.

A single junction *p-i-n a*-Si:H solar cell is deposited on glass substrate coated with a TCO. The TCO forms the top electrode and aluminium or silver is used as the bottom electrode. Since only the a-Si:H intrinsic layer contributes to the current generation, the optimal optical design of the cell structure maximises absorption in the intrinsic layer and minimises absorption in all the other layers. A standard *a*-Si:H *p-i-n* cell that has been fabricated at Delft University of Technology and at Utrecht University is designed to have a thin (0.01 μm) *p*-type layer; a thicker (0.45 μm) intrinsic layer; and a thin (0.02 μm) *n*-type layer.

There are some important practical design approaches for making high efficient *a*-Si:H solar cells schematically depicted in Figure 7.8b. These approaches lead to an enhancement of light absorption in the intrinsic layer of a-Si:H and are commonly described by the term ***light trapping***.

(i) The substrate that is used for deposition of *a*-Si:H layers is practically always textured. In Fig. 8b glass with textured SnO_2:F as the TCO represents the substrate. The texture introduces rough interfaces into a solar cell. When light enters the solar cell and reaches a rough interface, a part of it will be scattered in various directions instead of propagating in the specular direction. In this way the average light path in a layer is increased and the light absorption is enhanced.

(ii) In most practical *a*-Si:H solar cells the light enters the solar cell through the *p*-type layer. The reason for this has to do with the lower mobility of holes in comparison to electrons in *a*-Si:H. Since most of the photo-generated carriers are generated in the front part of the solar cell, holes have to travel on average shorter distance than the electrons to the respective electrodes. Remember that the photo-generated holes travel towards the *p*-type layer. In this way the collection efficiency of the holes is enhanced.

(iii) Because the light enters the solar cell through the *p*-type layer there is a substantial absorption in this layer. The photo-generated carriers in the p-type layer do not contribute to the photocurrent because the electrons, which are the minority carriers in the *p*-type layer, quickly recombine in this layer. It is therefore desired to minimize the absorption in the *p*-type layer which is realized by alloying the *a*-Si:H with carbon. The *p*-type *a*-SiC:H layer has high optical band gap and is referred to as a ***window layer***.

(iv) In order to accommodate a band offset between the *p*-type *a*-SiC:H and the intrinsic *a*-Si:H layer and to prevent a back diffusion of the photo-generated electrons into the p-type layer, thin layers are introduced at the *p-i* interface. These layers are called the ***buffer layers***.

(v) The cell is completed by the back electrode that often consists of a ZnO layer followed by a back metal, usually Ag, on top of the n-type *a*-Si:H layer. It has been demonstrated that this combination results in a highly reflective back contact that enhances the absorption of light in the long wavelength region (wavelengths above 600 nm).

7.6.3 Degradation of *a*-Si:H solar cells

Inherent to *a*-Si:H is that it exhibits changes in material properties when subjected to some external excitation such as illumination. The changes can be subsequently removed by annealing the material for a few minutes at 150°C to 200°C. Staebler and Wronski reported in 1977 the first measurements in which they found a decrease in the photoconductivity during illumination and a decrease in the dark conductivity after illumination[20]. This effect is since then called the ***Staebler-Wronski effect***. When solar cells are exposed to illumination a slow degradation of their performance is observed that is related to the Staebler-Wronski effect. The Staebler-Wronski effect is an example of the metastable creation of additional defects in the material under illumination. In solar cells these additionally created defects will act as extra trapping and recombination centres. As a result of the trapping a space charge distribution in the intrinsic *a*-Si:H layer is changed in such a way that the internal electric field is distorted. This leads to lower drift and thus to a lower collection efficiency. Much effort has been spent to find a solution for avoiding the Staebler-Wronski effect in solar cells. There is a continuous search for *a*-Si:H material with stable properties. New deposition techniques are investigated, such as HW CVD, that are expected to deliver more stable *a*-Si:H material.

The performance of *a*-Si:H solar cells decreases during the initial stage of operation due to light-induced degradation. After the initial degradation the performance of the solar cells stabilises. The stabilised performance of high quality solar cells is 70 - 90% of their initial performance. The degradation can be recovered by annealing. Therefore attention has to be paid, whether the reported efficiency of *a*-Si:H solar cells is the ***initial efficiency*** (as made) or the ***stabilised efficiency*** (after a degradation test). In different countries different conditions are defined for carrying out the degradation test. In Japan, "temporarily defined stabilised efficiency" is the value after 310-hour-exposure under following conditions: light intensity 1.25 sun, temperature 48°C, and open circuit condition. In the USA the stabilised efficiency is defined as the efficiency after 600 hours of continuous exposure to 1 sun at 50°C at open circuit conditions.

[20] D. L. Staebler and C. R. Wronski, *Appl. Phys. Lett.* **31**, 292 (1977).

The best reported initial efficiency for a laboratory single junction *a*-Si:H solar cell is 13.2% and it was achieved by a Japanese company Mitsui Toatsu. The highest stabilised efficiency is reported by USSC to be 9.3%. An example of illuminated J-V characteristics for the initial and the degraded states of a standard a-Si:H solar cell fabricated at TUD is shown in Figure 7.12. The external parameters of the cell are also reported in Figure 7.12.

7.6.4 Multi-junction *a*-Si:H solar cells

The degradation problem of *a*-Si:H solar cells can be partly solved by using thinner intrinsic layers in which case the internal electric field is higher and therefore less sensitive to any distortion. However, using a thinner layer results in a decreased absorption in the solar cell. A solution to obtain cells with a better stability and at least similar absorption as in the case of the conventional single junction solar cells is to stack two or more single junction solar cells with thin intrinsic layers on top of each other. This approach is called a ***multi-junction*** concept. In case of two junctions stacked on top of each other we talk about a ***tandem*** or ***double-junction*** solar cell, a stack of three junctions is named a ***triple-junction*** solar cell. The total thickness of the multi-junction solar cell is similar to a conventional single junction solar cell, but each component cell is thinner and therefore less sensitive to light-induced defects. An additional advantage of a multi-junction cell structure is that each component cell can be tailored to a specific part of the solar spectrum, thereby extending a usable part of the spectrum and increasing the solar cell conversion efficiency. At present the tailoring is realised by implementing *a*-SiGe:H. This effect is illustrated in Figure 7.13. Intrinsic a-Si:H has an optical band gap of ~1.70 eV and absorbs only photons with energies above 1.70 eV efficiently. The photons with the lower energies are not absorbed and thus lost for the energy conversion. A part of the photons with energies lower than 1.70 eV can be absorbed by *a*-SiGe:H layer that has an optical band gap of 1.45 eV. Tuning of the response to the solar spectrum is achieved by varying the concentration of germanium in *a*-SiGe:H, thereby lowering the optical band gap of the material. We call the implementation of materials with different optical band gaps for the active layers in multi-junction solar cells a ***multi-band gap*** approach. Most of current high efficient solar cells are based on the multi-junction and multi-band gap approach.

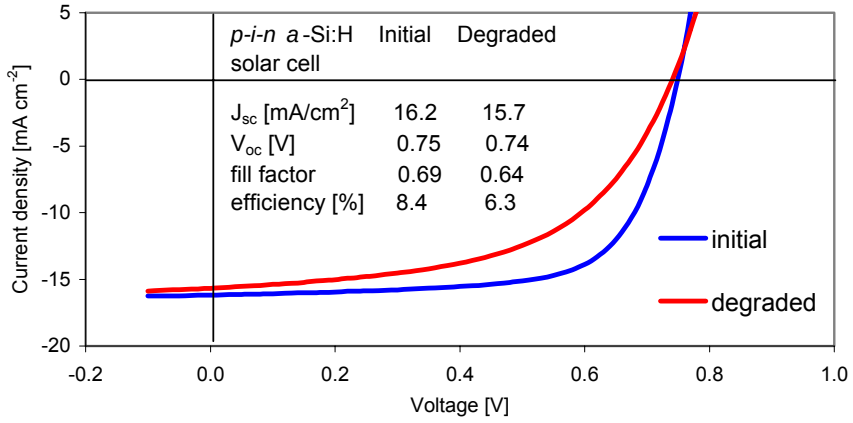

Figure 7.12. The initial and degraded illuminated *J-V* characteristic of a single junction *p-i-n* *a*-Si:H cell fabricated at Delft University of Technology.

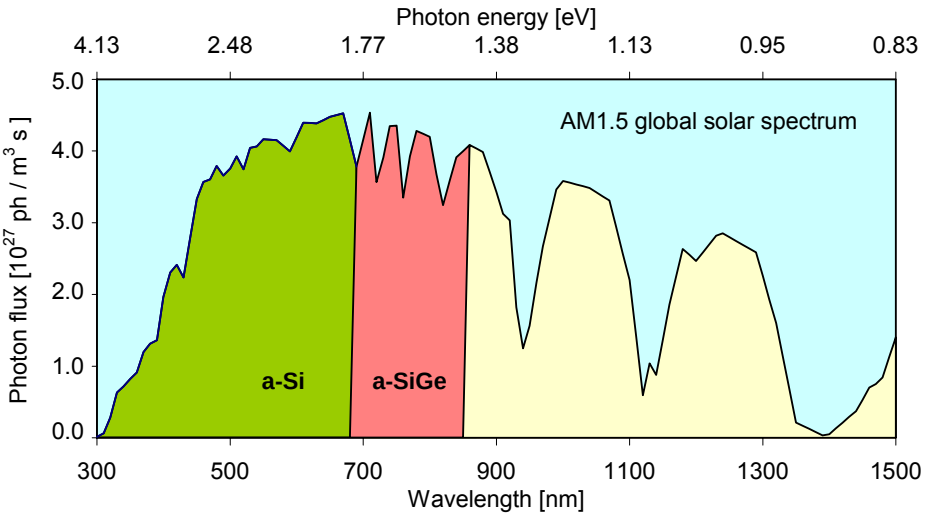

Figure 7.13. The AM1.5 global solar spectrum and the photons of the spectrum that are utilised by *a*-Si:H and by *a*-SiGe:H.

The multi-junction solar cell structure is far more complex than a conventional single junction solar cell. There are two crucial requirements for successful operation of the multi-junction solar cell: (i) the current generated at the maximum power point has to be equal in each component cell and (ii) a ***tunnel-recombination junction*** (TRJ) between the component cells has to feature low electrical and optical losses.

The first requirement reflects the fact that the component cells function as current sources that are connected in series. Therefore it is needed that each component cell generates the same current. The generated current depends mainly on the thickness of the intrinsic layer. In order to generate the same current, the thickness of the intrinsic layer of each component cell needs to be carefully adjusted, thereby taking the profile of photogenerated carriers, so called generation profile, in the cell into account. The second requirement concerns the interface between the component cells. This interface is in fact an *n*-*p* diode, which is connected in reverse, when the component cells operate in forward conditions. An ohmic contact between the component cells instead of a rectifying contact is required for proper operation of the solar cell. The problem can be resolved by fabricating a so-called tunnel-recombination junction. This junction ensures that the electrons that arrive at the *n*-type layer of the top cell and the holes that arrive at the *p*-type layer of the bottom cell fully recombine at this junction. The recombination of the photo-generated carriers at this interface keeps the current flowing through the solar cell. A very high electric field in this reverse biased *p*-*n* junction facilitates tunnelling of the carriers towards the defect states in the centre of the junction. The effective recombination of the carriers takes place through these states. A tunnel-recombination junction is usually realised by using microcrystalline silicon for at least one of the doped layers and/or to increase the defect density by incorporating a thin oxide layer at the interface between the two component cells.

An example of an *a*-Si:H/*a*-SiGe:H tandem cell is shown in Figure 7.14. The illuminated *J*-*V* characteristic and the external parameters of a *a*-Si:H/*a*-SiGe:H tandem cell

fabricated at Delft University of Technology are presented in Figure 7.15. The *a*-Si:H component cell absorbs photons with energies above 1.70 eV, photons with lower energies, which pass through the *a*-Si:H top cell, get a chance to be absorbed in the bottom cell by a-SiGe:H.

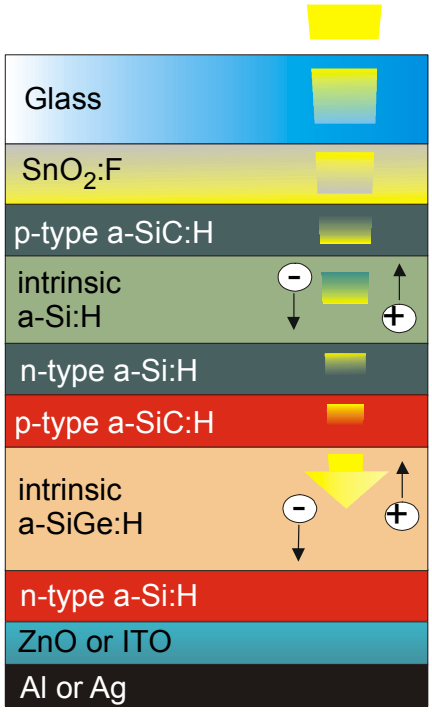

Figure 7.14. Typical structure of an *a*-Si:H/*a*-SiGe:H tandem cell.

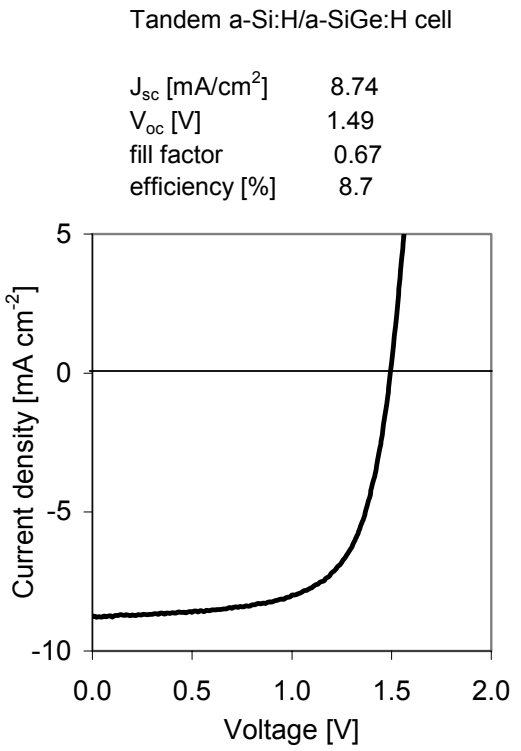

Figure 7.15. The illuminated *J*-*V* characteristic of a tandem *a*-Si:H/*a*-SiGe:H cell fabricated at Delft University of Technology.

In order to achieve current matching, the thickness of the intrinsic *a*-Si:H layer in the top cell is ~100 nm and the thickness of the intrinsic *a*-SiGe:H layer in the bottom component cell is ~150 nm. It means that the total thickness of a tandem cell is less than that of a single junction *a*-Si:H solar cell, in which the thickness of the intrinsic layer varies between 300 to 450 nm. As explained above, the use of *a*-SiGe:H for the intrinsic layer of the bottom cell in a tandem structure enhances the response of the cell in the long wavelength region. On the other hand, the use of *a*-SiGe:H introduces large band offsets near the *p*-*i* and *i*-*n* interfaces. For example, the band offset of 0.5 eV exists between a *p*-type a-SiC:H layer with a typical optical band gap of 1.95 eV and an *a*-SiGe:H layer with an optical band gap of 1.45 eV. These band offsets are believed to obstruct an effective collection of photo-generated carriers. In order to overcome this, profiling of the germanium concentration is carried out in a region near the interfaces. The term ***graded layer*** is used to denote the profiled region.

The highest stabilised efficiency for *a*-Si:H based solar cells to date has been demonstrated by USSC with a triple junction structure. This solar cell structure is shown in

Figure 7.16. In order to illustrate the complexity of the solar cell structure, which accommodates the graded layers and different materials for the active layers, a corresponding band diagram of the cell has also been included in Figure 7.16. USSC reported the stabilised efficiency of a small area cell (0.25 cm^2) to be 13.0 %. The initial efficiency of this cell was 14.6 %. Recently, an initial efficiency of 15.2 % was reported by this group, which indicates that further improvement in stabilised efficiency is feasible.

Comparing the external parameters of the single junction (see Figure 7.12) and tandem (see Figure 7.15) solar cells we notice that the J_{sc} is lower while the V_{oc} is higher in case of a tandem cell. This observation is even more pronounced for triple-junction cells. For practical applications, the external parameters of multi-junction solar cells are advantageous in comparison to single junction cells, because the lower current means less loss in the electrodes, especially in the TCO, and the higher output voltage allows more flexible design of a module with required voltage.

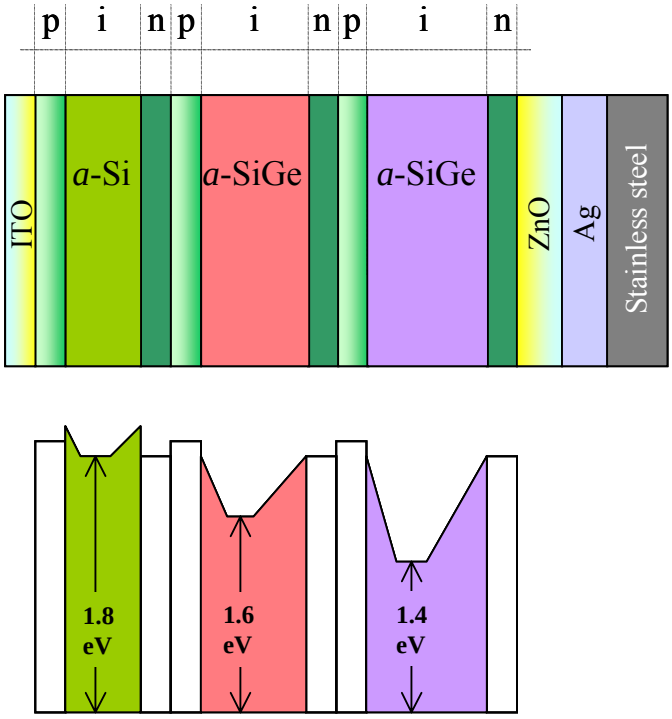

Figure 7.16. A triple-junction solar cell with a corresponding schematic band diagram.

7.7 Fabrication of thin-film silicon PV modules

7.7.1 Thin-film silicon PV modules

Power that is delivered from a small area laboratory cell is not enough in practical applications. Therefore, solar cells are connected with each other in series and/or parallel to form a module that delivers a required power or voltage. The solar cell performance that is first optimised on a laboratory scale with a cell area ranging from 1 to 100 cm^2 is difficult to obtain on a module, which has an area 1.000 cm^2 and more. Several requirements need to be fulfilled on a module level. The uniformity and homogeneity over the deposited area must be good. The area loss due to encapsulation, patterning, and current carrying grid lines and the electrical loss due to TCO and grid lines resistance should be minimal. Concerning conversion efficiency, one has to be careful to distinguish among the reported values, because there is misleading discrepancy between:

- laboratory record mini-cells (size below $1cm^2$, no patterning)
- R&D modules, not encapsulated and not produced in large quantities (size of 1 square-foot)
- standard commercial modules

Furthermore, attention has to be paid whether the efficiency value is the *initial* efficiency of the cell (as made) or the *stabilised* efficiency (after a degradation test).

A key step to practical industrial production of *a*-Si:H solar cells was the development of the monolithically integrated type of *a*-Si:H solar cell[6], in which several subcells, deposited on one substrate, are connected in series, as shown in Figure 7.17. The integration of the subcells can be obtained by using conventional masking techniques or laser scribing. Using the monolithic integration of *a*-Si:H solar cells, a desired output voltage from a single substrate can be easily achieved. The process steps for the integration of the subcells can be easily implemented in the whole fabrication process of a module. This gives *a*-Si:H technology a great advantage in comparison with single crystal silicon module technology, where the subcells are mechanically connected with each other.

The first commercial *a*-Si:H solar cells were put on the market in 1980 by the Japanese companies Sanyo and Fuji Electric. Their size was typically a few square centimetres and these cells were applied in consumer electronics such as calculators. Since then the manufacturing technology of *a*-Si:H solar modules has experienced a rapid advance in increasing the module size and the efficiency. In 1999 the total production of *a*-Si:H modules was 25 MWp that represented 12.3% of the world total PV module production. There are several facilities in the world that manufacture large area *a*-Si:H modules. In 2001 several mass-production lines were in operation such as by Kaneka in Japan (20 MWp/year), BP Solarex (10 MWp/year) and USSC (5 MWp/year) in the USA. Several companies work on the basis of a pilot line such as Phototronics in Europe, Fuji Electric and Sanyo in Japan.

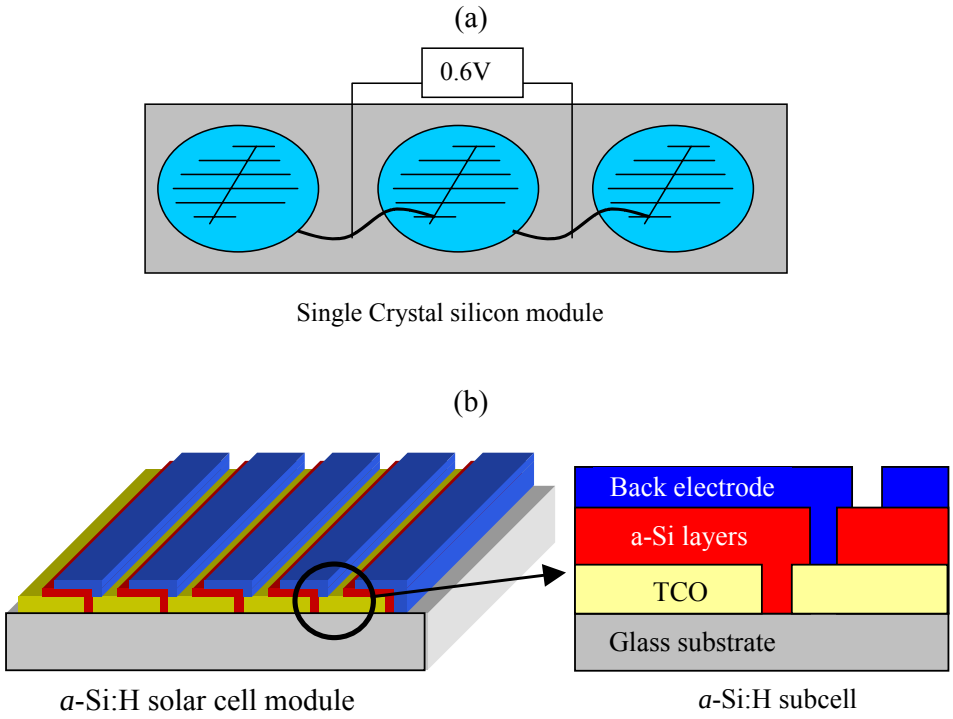

Figure 7.17. Schematic representation of a series interconnection. (a) Mechanically interconnected single crystal silicon cells and (b) Monolithically integrated a-Si:H subcells.

At present, glass-plates or stainless steel sheets are used as the substrates in production. The choice of the substrate material influences the production technology, though the principal steps of the production process remain the same for both. In case of glass substrates the *p-i-n* deposition sequence is used, in case of stainless steel the *n-i-p* sequence process takes place. The different sequence has influence on some of the technological steps. The main steps in fabricating the solar cells are:

- substrate preparation
- TCO front electrode deposition
- deposition of a-Si:H layers
- back electrode deposition
- final assembly (encapsulation, framing, and testing)

One of the important requirements for a company to stay competitive in the solar cell business is to be technologically independent. This is a driving force for the companies to have all necessary technologies available. Central to each of the production lines is the PECVD reactor, whose design determines throughput, flexibility to cell design variations, quality and uniformity of the layers and defect density levels. Most producers who use TCO coated glass substrates strive to have their own TCO deposition in order to be independent of the suppliers. Having an own TCO deposition machine enables them to control the quality of the TCO that is crucial for overall performance of solar cells. The commercial a-Si:H modules consist of monolithically integrated cells. The series interconnection on the substrate is achieved during the construction of the cell structure by including two or more laser scribing steps between depositions of the respective layers. The laser cutting selectively removes

narrow lines (width 50 to 150 μm) of material in order to limit the area losses. The laser scribing is also a speed limiting step in the production line. Usually, pulsed Nd:YAG lasers are used for scribing the films. The final product must be well protected against the atmospheric influence to prolong its lifetime. Several encapsulation methods are used for the purpose of protection. Most common method is to use a polymeric film ethylene/vinyl acetate (EVA) as the cover of the module on top of which a glass sheet is placed. An increasing attention is paid to framing of the modules as *a*-Si:H solar modules are becoming an attractive element for building applications.

7.7.2 PECVD deposition systems

Since the *a*-Si:H and/or *μc*-Si:H layers form the heart of the solar cell, the way these layers are produced at industrial level is described in more detail. The standard industrial deposition technique of *a*-Si:H and *μc*-Si:H is the PECVD method. There are several configurations of the PECVD reactors that are used for production.

(A) Single chamber system

The deposition of all a-Si:H layers is carried out in a single reaction-chamber. This system has the advantage that there is no transport of substrates under vacuum conditions. If a load lock chamber is used, a simple form of linear transport is sufficient. The substrates can have a very large size, and can be handled as mounted in a plasma box. The capital investment is low compared to the other configurations. A disadvantage is that production may take a long time since several purge and pump-down steps are needed to obtain well defined consecutive depositions of differently doped and undoped layers. There are limited possibilities to apply buffer layers or graded layers at the interfaces. The geometry of the electrodes and the deposition temperature usually cannot be varied for the various layers. This leads to a trade off between the optimum deposition parameters for the individual layers. Therefore, in a single chamber system the solar cell structure will be less than optimal.

(B) Multi-chamber system

This system has the advantage of complete control of the level of dopants and other impurities. In this type of system it is possible to produce controlled compositional profiles, with increasing or decreasing concentrations of constituents, without affecting the impurity level of subsequent layers. The deposition temperatures, the internal geometry, and even the discharge frequency can be optimised for each layer individually. The transfer of the manufacturing process from the laboratory to production requires only small adaptations. A disadvantage is that the size of the panels may be limited. Nevertheless, the panels with a size of 40 cm × 120 cm and 60 cm × 100 cm have been produced with multi-chamber configuration. Another disadvantage is that the investment is quite large.

Two types of multi-chamber systems are in operation:

(B1) in-line configuration

This configuration offers the feasibility to deposit on moving substrates. This leads to extremely good uniformity of the layers over very large areas, an important feature for tandem solar cell structures. As the deposition plasma does not need to be extinguished, an important source of dust and microparticles is eliminated. The throughput of these machines can be very high. However, the equipment cost is very high, because special isolation chambers and vacuum valves are needed to separate the deposition chambers. Furthermore, in-line machines usually take up quite some space. The layer sequence is determined by the

physical configuration of the system and cannot be adapted easily. This reduces flexibility in a multi-layer structure.

(B2) cluster configuration

This configuration is known from the laboratory, but may be the best choice also for (pilot) production. A cluster system has all the advantages of a multi-chamber system. The transition from laboratory experience to production is as small as possible. Modifications in the layer sequence or changes in the number of the layers of the solar cell structure (e.g. from a single junction to a tandem or triple junction) can be made as desired. Apart from this the capital cost is low, because transport and isolation chambers can be shared by many deposition chambers. If a sufficient number of chambers are connected to the transport chamber, production can be continuous even if one of the deposition reactors is down for maintenance. This is in contrast to *in-line* systems, which must be shut down completely if one of the chambers needs maintenance. The area requirement of a cluster system is very modest. The flow of reactive gases is only needed when there is a substrate in the deposition chamber, thus cutting down the base materials usage. Profiled and graded layers are much more easily made than in the case of *in-line* systems.

All of the above production facilities can be used in a ***single panel*** mode or in a ***batch*** mode. In the latter mode a number of substrates is loaded at the same time, a principle often applied in a single chamber system to bring the throughput to the required level. Due to the long processing time single chamber systems can only be cost-effective when they are batch-type systems. In multi-chamber systems one usually uses a single panel mode. The panels can be transported in a holder or without support. The latter possibility reduces cross contamination, which may result from the holder. As the number of vacuum chambers is larger and as purging steps can be omitted, the throughput can be approximately equal to that of a single chamber system. Multi-chamber processes can also use batch type mode. Several substrates have to be then transported simultaneously in vacuum. This can be done even without a holder, which however may lead to very complicated transport mechanisms.

(C) Roll-to-roll system

The roll-to-roll process is neither the single chamber nor the multi-chamber method. At present, this process is used by USSC and its affiliates for depositing tandem and triple-junction solar cells. An example of the flexible and framed modules produced by USSC is shown in Figure 7.18. It is potentially a cheap method, but there are some disadvantages. For instance, if the substrate is made of stainless steel, then the series interconnections cannot be done monolithically. A solution is to use the stainless steel merely as a carrier for an insulating plastic substrate. The central part of the line, the machine for the a-Si alloy deposition, consists of a stainless steel web roll-off chamber, six (nine) PECVD chambers for six (nine) layers of the double (triple) junction cell and a roll-up chamber. Stainless steel web, coated with Ag/ZnO, moves continuously through the chambers where the various layers are sequentially deposited. There is an increased risk that cross contamination occurs, since all deposition zones by definition are connected to each other. Since no purging steps can be used as in the single chamber systems, so-called gas gates are used to isolate the adjacent chambers and minimise the adverse effects.


Figure 7.18. Example of USSC flexible and framed *a*-Si:H solar cell products.

In 1997 a project was started in the Netherlands with the purpose to develop a roll-to-roll production method for *a*-Si:H thin film solar cells, called the Helianthos project. The production method is based on a novel ***temporary-superstrate*** concept. This means that a *p-i-n a*-Si:H structure is deposited on a temporary carrier, which is coated with SnO_2:F TCO. The aluminium foil serves as a temporary carrier of the solar cell. After deposition of the complete solar cell, including the back contact, the cell is laminated on a permanent carrier. By removing the aluminium foil, light can enter the cell through the top TCO layer. A wide variety of transparent encapsulants can be used to finalize the product that can be flexible or rigid. The Helianthos project is carried out by Utrecht University, Delft and Eindhoven Universities of Technology, the Netherlands Organization of Applied Scientific research, and the multinational corporation Akzo Nobel. The feasibility of the new temporary-superstrate concept has been demonstrated by depositing a solar cell with 6% initial efficiency. A roll-to-roll pilot plant is expected to be in operation in 2002.

For those readers who are interested to learn all aspects of *a*-Si:H and *μc*-Si:H solar cell technology in detail a book on "Amorphous and Microcrystalline Silicon Solar Cells" written recently by Schropp and Zeman[17] is recommended.

Chapter 8.

ORGANIC SOLAR CELLS

Tom J. Savenije

DelftChemTech, Faculty of Applied Sciences
Delft University of Technology

Prof. Dr. Rene Janssen from the Departments of Chemical Engineering & Chemistry and Applied Physics, Eindhoven University of Technology is acknowledged for his contribution. This chapter contains limited parts of papers by B.A. Gregg and co-workers, NREL, Golden, Colorado, USA.

8.1 Introduction to organic solar cells

Conventional solar cells were invented in the 1950s and first commercialized in the 1960s for use in space programs. Since then there have been rapid advances in the efficiency and reliability of these cells, along with a substantial decrease in their fabrication costs. As a result the photovoltaic industry has been growing rapidly. Nevertheless the price of solar electricity is still greater than the price of electricity from the electrical grid in industrialized countries. For this reason there is an increasing amount of research devoted to potentially less expensive types of solar cells such as those based on organic dyes and polymers. These cells have been studied since the late 1950s albeit at a fairly low level until recently. One of the great promises of organic electronics is that synthetic chemists can produce compounds matching the opto-electronic properties desired.

A fundamental difference between solar cells based on organic materials and conventional inorganic photovoltaic (IPV) cells is that light absorption results in the formation of excitons in molecular materials, rather than in free electrons and holes. An exciton in an organic semiconductor can be considered as a tightly coulombicly bound electron hole pair. Due to its electrical neutrality and the strong binding energy between the hole and the electron it can be regarded as a mobile excited state. Due this fundamental difference the processes involved in the conversion of photons into electrical energy are not

the same as those occurring in IPV cells. In this chapter, solar cells in which excitons are generated due to light absorption, hereafter denoted as organic solar cells will be discussed. First some more relevant properties of organic materials based on dye molecules or on polymers (often referred to as molecular materials) are given in 8.2. Paragraph 8.3 deals with the topic of excited states in molecular materials. Section 8.4 describes the processes in organic solar cells relevant for the conversion of incident photons into electric energy. In section 8.5 more details about the most successful approaches towards organic solar cells *i.e.* dye sensitized solar cells, organic bilayer cells and bulk heterojunction cells are discussed. Future prospects regarding lifetimes and efficiencies for organic solar cells are the topic of the last section 8.6 of this chapter.

8.2. Molecular materials

Organic molecules and polymers have the immense advantage of facile, chemical tailoring to alter their properties, such as the optical band gap. For example conjugated polymers (see Figure 1) combine the electronic properties known from the traditional semiconductors with the ease of processing and mechanical flexibility of plastics. The research on these kinds of organic materials was initiated by Heeger, MacDiarmid and Shirakawa, who discovered that the conductivity of polyacetylene (PA) could be increased by seven orders of magnitude. Since then, this new class of materials has attracted considerable attention owing to its potential of providing environmentally safe, flexible, lightweight, and inexpensive electronics.

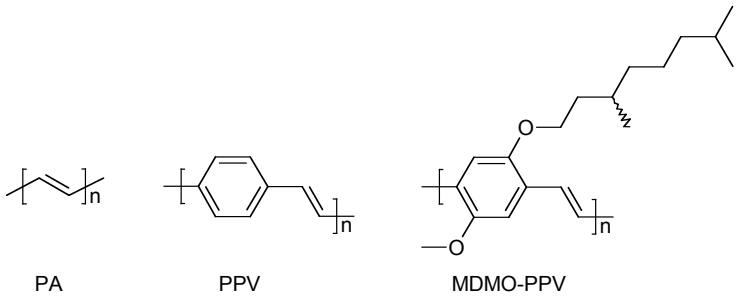

Figure 8.1. Molecular structures of the conjugated polymers trans-polyacetylene (PA), poly(p-phenylene vinylene) (PPV), and a substituted PPV (MDMO-PPV).

The cost reduction mainly results from the ease of processing from solution. However, solution processing requires soluble polymers. Poly[p-phenylene vinylene] (PPV, Figure 1) is hardly soluble. Attachment of side-groups to the conjugated backbone, as in poly[2-methoxy-5-(3′,7′-dimethyloctyloxy)-1,4-phenylene vinylene] (MDMO-PPV, Figure 1), enhances the solubility of the polymer enormously.

Recent developments in ink-jet printing, micro-contact printing, and other soft lithography techniques have further improved the potential of conjugated polymers for low-cost fabrication of large-area integrated devices on both rigid and flexible substrates. A good example of the use of this kind of polymers in commercial products are the light emitting diodes. Architectures to overcome possible electronic scale-up problems related to thin film organics are being developed. In contrast to conjugated polymers, conjugated molecules are mainly thermally evaporated under high vacuum. Despite the fact that gradual improvement

of the efficiency has been achieved of solar cells based on this deposition technique, this method is more expensive than solution processing and, therefore, less attractive.

The energy levels in molecular materials can be related to the energy levels of inorganic semiconductors (see Figure 8.2). As already discussed in previous chapters the energy needed to release an electron from the valence band of an inorganic semiconductor to the vacuum level is denoted as the ionisation potential, while the electron affinity denotes the energy gained when an electron is transferred from the vacuum level to the conduction band edge. In molecular materials also electrons can be liberated from the so-called highest occupied molecular orbital (HOMO) to the vacuum. The energy involved can roughly be estimated on basis of the electrochemical oxidation potential (*vs.* NHE) of the molecules using the relation: $E_{HOMO} \approx E_{NHE} - V_{ox}$, with $E_{NHE} = -4.5$ V *vs.* vac. In a similar way the electron affinity can be estimated from the reduction potential of the molecules using: $E_{LUMO} \approx E_{NHE} - V_{red.}$ The difference between both energy levels corresponds to the optical bandgap of the molecules. Alternative methods to determine the energy levels in molecular layers include: Ultraviolet photoelectron spectroscopy (UPS) and Kelvin probe measurements. The concentration of mobile charge carriers within intrinsic molecular layers in the dark at room temperature is usually small. The resulting conductivity of these layers is therefore relatively small. Intentional doping to form n- or p-type layers is not straightforward, since this causes often degradation of the organic material.

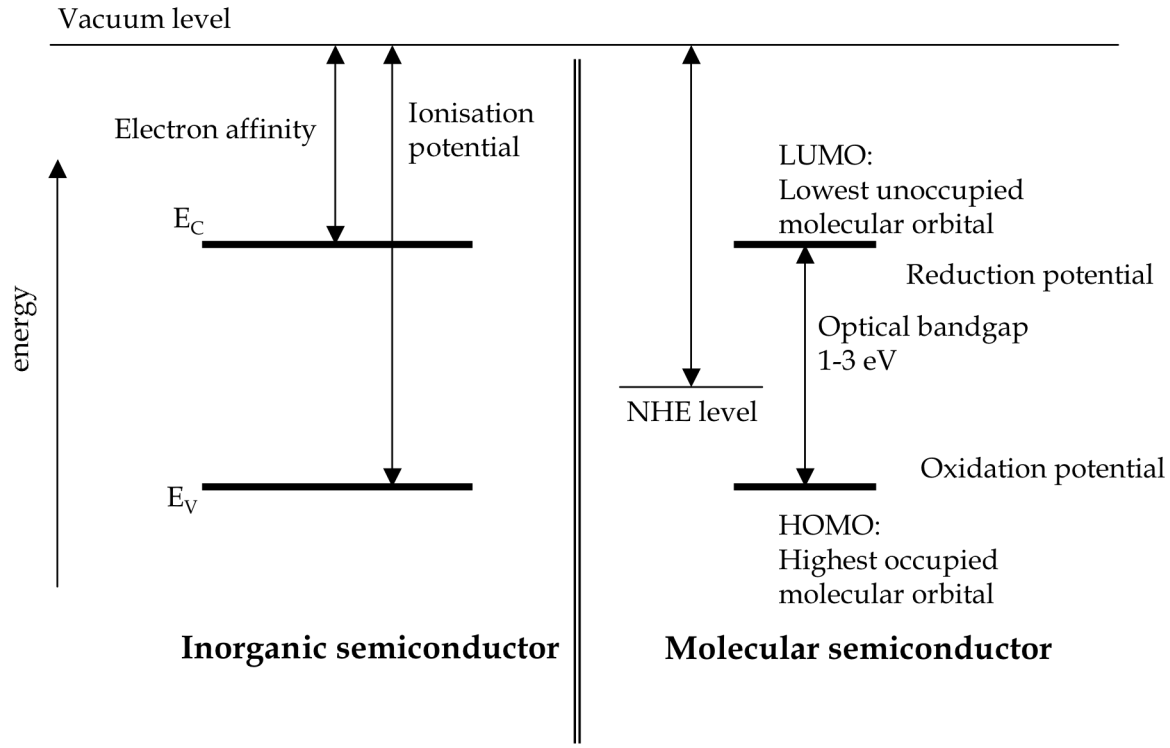

Figure 8.2. Overview of energy levels in inorganic semiconductors (left) and molecular semiconductors (right).

Molecular materials that have a low ionisation potential and thus can easily donate an electron are denoted as electron donors. Materials that have a high electron affinity and thus can easily take up an electron are denoted as electron

acceptors. If a molecule is an electron donor or an electron acceptor is an intrinsic property of the compound.

8.3 Excited states in molecular materials

A key difference between organic solar cells and IPVs is the relative importance of interfacial processes. This difference is related to the charge carrier generation mechanism. Light absorption in IPV cells results directly in the formation of free charge carriers. This means that charges are created throughout the bulk of the semiconductor. In contrast, light absorption in organic materials almost always results in the production of a mobile excited state rather than in free charge carriers. This is due to two reasons: First the dielectric constant of the organic material is usually low as compared to inorganic semiconductors. This creates an attractive Coulomb potential well around charges. Secondly in molecular materials the non-covalent electronic interactions between the molecules are weak as compared to the strong interatomic electronic interactions of covalently bound inorganic semiconductors like in silicon. For these two reasons the wavefunction of the electron is spatially restricted to the potential well induced by its positive counterpart. Therefore the usual product of light absorption in molecular materials is a tightly bound, neutral electron/hole pair or exciton.

To envisage the effect of a potential well in more detail the binding energy, E_B, between two opposite charges in a molecular material is calculated using:

$$E_B = \frac{q^2}{4\pi\varepsilon_r\varepsilon_0 r_c} \tag{8.1}$$

with r_c the critical distance between both charged carriers, ε_r is the relative dielectric constant and ε_0 is the permittivity of free space. A charge carrier becomes free from the Coulomb attraction of an opposite charge when $E_B \leq k_B T$, which amounts to 25 meV at room temperature. This yields together with 8.1

$$r_c \geq \frac{q^2}{4\pi\varepsilon_r\varepsilon_0 k_B T} \tag{8.2}$$

Figure 8.3 shows the effect of the temperature and the dielectric constant on the critical distance. For molecular excitons r_c is typically in the order of 1 nanometer which corresponds to a binding energy exceeding 0.25 eV. However, to obtain a photovoltaic effect in an organic solar cell the exciton must be dissociated. To overcome this problem, organic solar cells commonly utilize two different materials that differ in electron donating and accepting properties. Dissociation of the exciton is accomplished by electron transfer between the two compounds. The energy gained by this process should then exceed the exciton binding energy. In this way the photogeneration of free charge carriers is much more efficient as compared to the individual, pure materials, in which the formation of bound electron-hole pairs, or excitons is generally favoured.

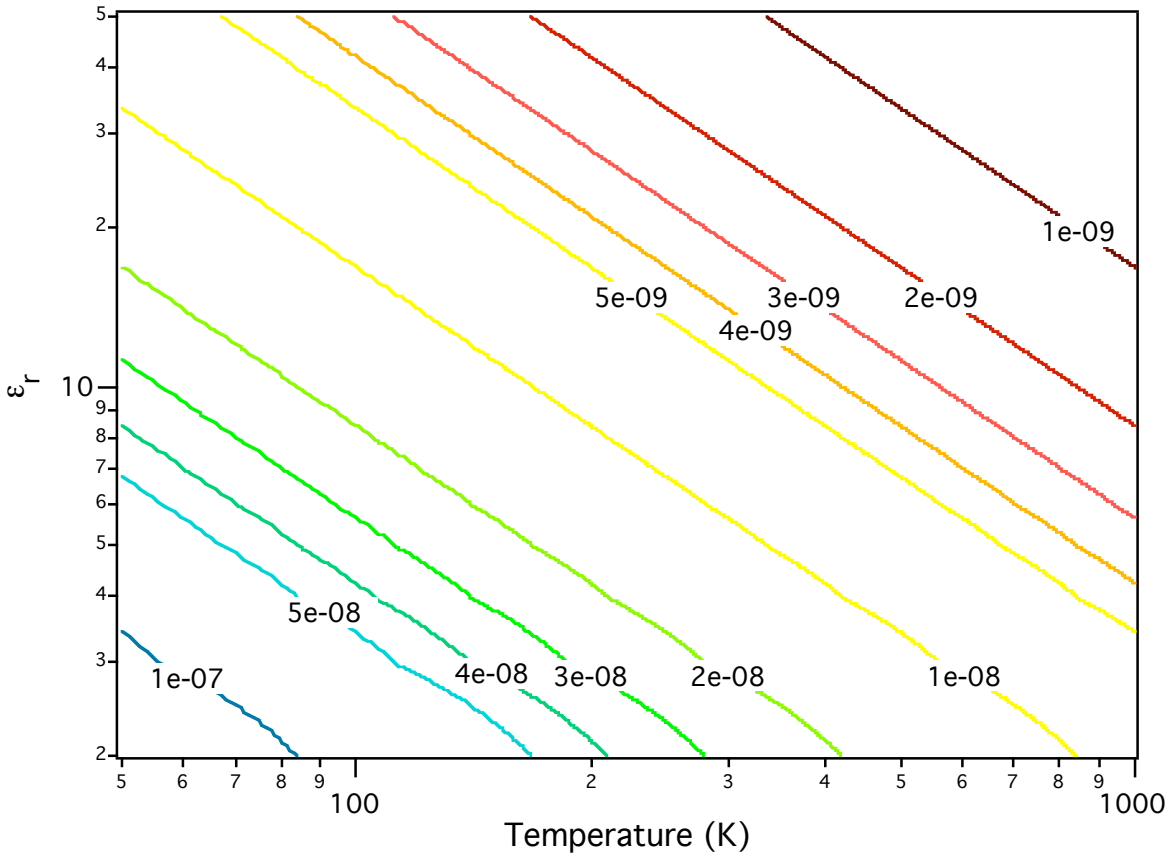

Figure 8.3. Illustration of the critical distance between a positive hole and an electron as function of the temperature and the dielectric constant. At room temperature in molecular materials with an ε_r of 3.5 r_c is approximately 20 nm while at the same temperature for Si with an ε_r of 11.7 this value is close 6 nm.

8.4 Basic processes in organic solar cells

In general, for a successful organic photovoltaic cell five important processes have to be optimized to obtain a high conversion efficiency of solar energy into electrical energy:

1. Absorption of light and generation of excitons
2. Diffusion of excitons to an active interface
3. Charge separation
4. Charge transport
5. Charge collection

To create a working photovoltaic cell, the two photoactive materials are sandwiched between two (metallic) electrodes (of which one is transparent), to collect the photogenerated charges (see Figure 8.4). After the charge separation process, the charge carriers have to be transported to these electrodes without recombination. Finally, it is important that the charges can enter the external circuit at the electrodes without interface problems.

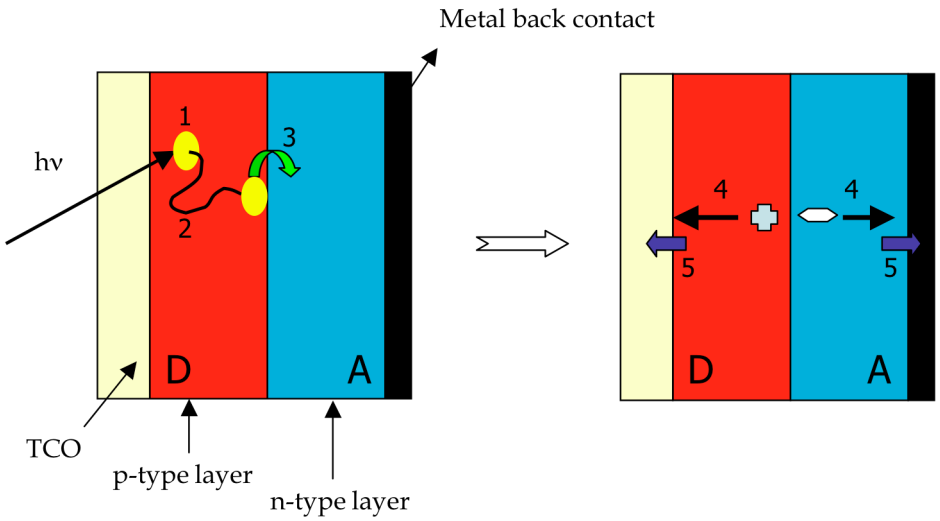

Figure 8.4. Schematic drawing of the working principle of an organic photovoltaic cell. Illumination of a donor material (in red) through a transparent electrode (ITO) results in the formation of an exciton (1). Subsequently, the exciton is transported by diffusion (2) to the interface between the donor material and an acceptor material (in blue). Electron is transferred to the acceptor material ($A^{\bullet -}$), leaving a hole at the donor material ($D^{\bullet +}$) (3). The photogenerated charged carriers are then transported (4) to and collected at opposite electrodes (5). A similar charge generation process can occur, when the acceptor is photoexcited instead of the donor.

8.4.1. Light absorption

For an efficient collection of photons (process 1), the absorption spectrum of the photoactive organic layer should match the solar emission spectrum and the layer should be sufficiently thick to absorb most of the incident light. Generally the optical absorption coefficient (α) of organic materials is much higher than that of crystalline or multicrystalline silicon as shown in Figure 8.5. For the conjugated polymers MDMO-PPV and P3HT and for the molecular dye, zinc phthalocyanine (ZnPc) α exceeds $1\times10^{5}cm^{-1}$ in the major part of the visible spectrum. Using Equation 3.38 this implies that a 100 nm thick organic layer is sufficient to reduce the light intensity to 1/e times its original value. For comparison, to obtain a similar decrease of the light intensity the crystalline silicon layer should be two orders magnitude thicker.

The absorption coefficient spectra of MDMO-PPV and P3HT shown in Figure 8.5 lack absorption in the red and NIR part of the spectrum. As discussed previously for a photovoltaic cell based on a single light absorbing medium a band-gap of approximately 1.1 eV is optimal. By lowering the band gap of the organic material it is possible to harvest more sunlight and therefore an increase in the photocurrent can be expected. For this reason much research effort is presently devoted to obtain organic polymers with an optical band in the NIR, so called small band-gap polymers. Though increasing the layer thickness is often advantageous for light absorption, charge transport might be hampered. This results in a lower the fill factor.

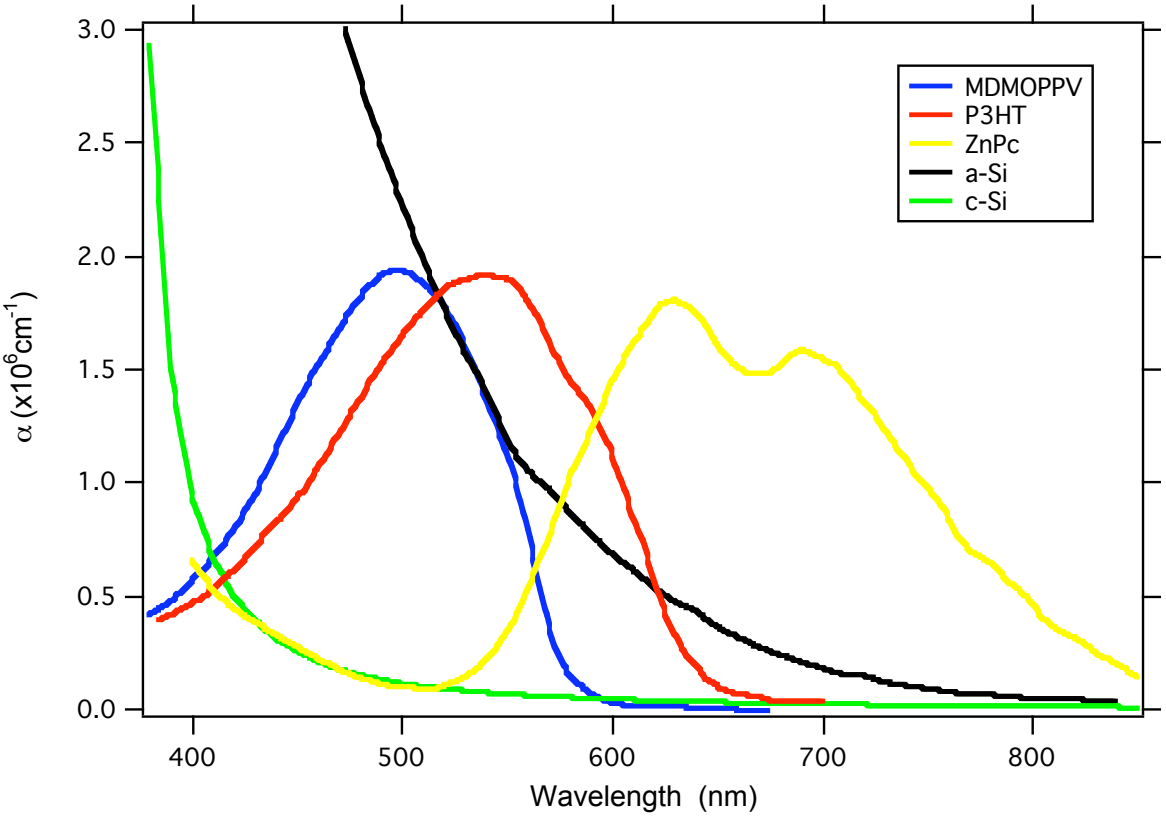

Figure 8.5. Absorption coefficients of various solar energy materials.

8.4.2. Exciton transport

For realisation of an efficient organic solar cell all excitons formed due to light absorption should lead to the formation of free charge carriers. However exciton transport is in competition with other decay processes such as luminescence or radiative recombination to the ground state. The exponential lifetime of an exciton (τ_{EXC}) is determined by the reciprocal value of all radiative and non radiative decay rates together. For an efficient solar cell all excitons have to reach the photo-active interface within τ_{EXC}. Transport of the excitons occurs by diffusion and the distance an exciton is able to cross, L_{EXC}, is given by:

$$L_{EXC} = \sqrt{D_{EXC}\tau_{EXC}} \qquad (8.3)$$

in which D_{EXC} is the diffusion coefficient of the excitons. Since for molecular materials τ_{EXC} is often only several nanoseconds at most, L_{EXC} is generally limited to 10 nm. In practice this implies that only those excitons formed within a distance of L_{EXC} from the interface will contribute to charge separation. To avoid this problem, research has been devoted to increase the diffusion coefficient of excitons or to the make the interfacial area much larger, so that each generated exciton is always close to an interface. Each of these approaches has led to completely different cell designs as will be shown in section 8.5.

8.4.3. Charge separation

Creation of charges is one of the key steps in the conversion of solar light into electrical energy. In most organic solar cells, charges are created by photoinduced electron transfer. In

this process an electron is transferred from an electron donor (D) material to an electron acceptor (A) material with the aid of the additional input energy of an absorbed photon with energy hν. An electron donor is characterized by a molecular material with a small electron affinity. Vice versa an electron acceptor is a material with a high electron affinity. The difference between both electron affinity levels is the driving force required for the exciton dissociation. In the photoinduced electron transfer process an exciton at the D/A interface decays by creation of the charge-separated state consisting of the radical cation of the donor ($D^{\bullet+}$) and the radical anion of the acceptor ($A^{\bullet-}$).

$$D + A + h\nu \rightarrow \quad D^* + A \quad (\text{or } D + A^*) \rightarrow \quad D^{\bullet+} + A^{\bullet-}$$

For an efficient charge generation, it is essential that the charge-separated state is the thermodynamically and kinetically most favourite pathway for the exciton. Therefore, it is important that the energy of the absorbed photon is used for generation of the charge-separated state and is not lost via competitive processes like fluorescence or non-radiative decay. In addition, the charge-separated state should be stabilized, so that the photogenerated charges can migrate to one of the electrodes. Therefore, the back electron transfer or recombination should be slowed down as much as possible.

In a homojunction between a p-type and an n-type silicon semiconductor under illumination electrons flow from the p-type to the n-type semiconductor. In a heterojunction based on an electron donor layer D and an electron accepting layer A, under illumination electrons flow from the D to the A layer as illustrated in Figure 8.4. Therefore the D layer is also denoted as the p-type layer and the A layer as the n-type layer in analogy with a silicon pn junction. Therefore molecular materials with a low ionisation potential are commonly p-type and materials with a high electron affinity n-type.

8.4.4. Charge transport

The charge transport mechanisms operating in IPV cells and organic solar cells to drive charge carriers towards the electrodes are again very different. Light absorption in IPV cells leads directly to the production of electrons and holes in the same material. Since the two carrier types have the same spatial distribution, the concentration gradient, which is the driving force for the transport by diffusion is identical (See Figure 8.6). Therefore both charge carriers are driven in the same direction. Since this is a small driving force in IPV cells, the electrical potential gradient present at the interface of a p-n junction (the band bending) is able to separate the photo-induced electrons from the holes effectively. In contrast to IPV cells in organic solar cells after the charge transfer the electrons and holes are in close proximity. Therefore there is a large chemical potential gradient that drives the charge carriers away from the exciton dissociating interface.

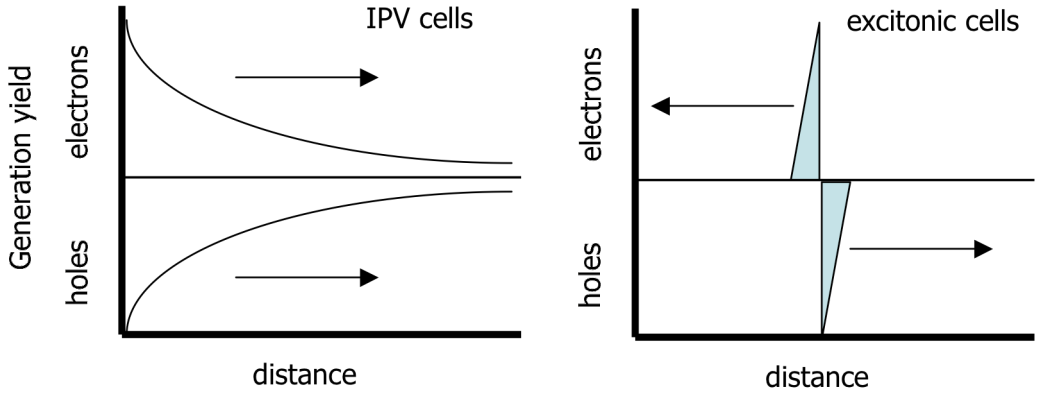

Figure 8.6. Schematic description showing the effect on the charge carrier distributions induced by the different charge carrier generation mechanisms in IPV cells (left) and organic solar cells (right).

Though for IPV cells the electric field is the main driving force for charge transport, it is not yet clear to what extent the internal electrical field contributes to the charge transport in organic solar cells. This is due to the differences in mobilities in molecular materials and inorganic semiconductors. The velocity charge carriers acquire under the influence of an electric field (ξ) is given by the relation:

$$v_{di} = \mu_i \xi \qquad (8.4)$$

in which μ_I is the mobility. The mobility in molecular materials is relatively small (< 0.1 cm^2/Vs) as compared to inorganic semiconductors (100 - 10000 cm^2/Vs). In addition it is not yet clear if and how an electrostatic potential in an organic bilayer is formed. This is due to the fact that molecular materials contain only low densities of mobile charge carriers. In view of the above the rate kinetics for the various charge carrier recombination processes are important parameters in particular for organic solar cells. These processes should be sufficiently slow to allow the charge carriers to reach the electrodes.

8.4.5. Charge collection

The collection of charge carriers at the electrodes is regularly accomplished by a transparent conductive oxide (TCO) such as ITO or SnO_2:F on one side and a metal contact on the other side. Care has to be taken that an Ohmic contact between the electrodes and the molecular layers is formed. In practice special contact layers have been developed to obtain better performance of the solar cell. Examples of contact layers are a PEDOT:PSS layer, which is a charged conducting polymer layer at the TCO side and LiF layers at the metal contact. The exact reason how these layers improve the cells is unclear.

For IPV cells the V_{OC} is limited by the electrostatic potential at the junction (see Chapter 4). For organic solar cells reasonable open circuit voltages have been measured for cells build up by using a single photoactive molecular material and identical electrodes. From this observation it is evident that the V_{OC} is determined by other factors than for an IPV cell. For an organic solar cell based on two molecular materials as depicted in Figure 8.4 optical excitation leads to the formation of an exciton in one of the layers. For the charge separation process part of the original energy of the photon is lost, yielding an electron in the n-type material and a positive charge carrier in the p-type material. In case there is no potential loss at the electrodes the maximum observed potential can be obtained by as shown schematically in Figure 8.7:

V_{OC} = Ionisation potential of the p-type material – electron affinity of the n-type layer
In practice a potential loss at the electrodes in the order of 0.2 V is often observed.

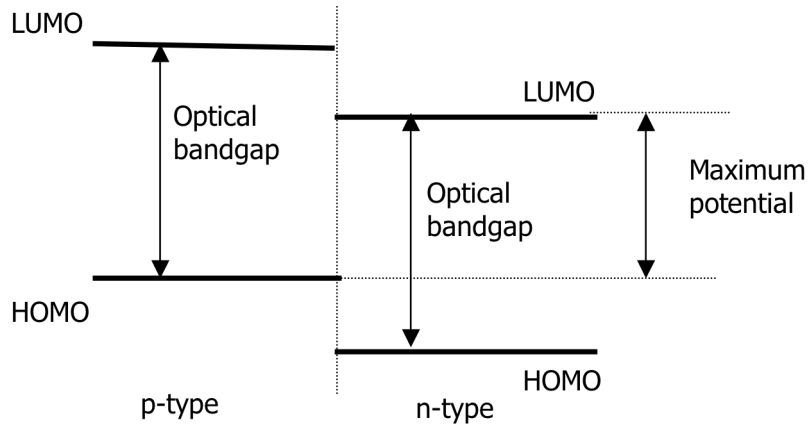

Figure 8.7. Energy levels involved in determining the maximum potential generated by an exciton solar cell. The offset in the energy levels corresponding to LUMO forms the driving force for the dissociation of the exciton.

8.5. Organic solar cells

In this paragraph a short overview is given of the most successful approaches towards organic solar cells to date. First, cells will be described in which organic molecules are only used for absorption of light, followed by cells in which an organic or polymeric material is used for absorption of light and for charge transport.

8.5.1 Dye-sensitized solar cells

In a dye-sensitized solar cell, an organic dye adsorbed at the surface of an inorganic wide-band gap semiconductor is used for absorption of light and injection of the photoexcited electron into the conduction band of the semiconductor. The research on dye-sensitized solar cells gained considerable impulse, when Grätzel and co-workers greatly improved the interfacial area between the organic donor and inorganic acceptor by using nanoporous titanium dioxide (TiO_2). To date, ruthenium dye-sensitized nanocrystalline TiO_2 (nc-TiO_2) solar cells reach an energy conversion efficiency of about 10%. In the Grätzel cell (Figure 8.9), the ruthenium dye takes care of light absorption and electron injection into the TiO_2 conduction band. An I^-/I_3^- redox couple, contained in an organic solvent, is used to regenerate (i.e. reduce) the photooxidized dye molecules. In the cells, the positive charge is transported by the liquid electrolyte to a metal electrode, where I_3^- takes up an electron from the external circuit (counter electrode), while the negative charges injected in nc-TiO_2 are collected at the TCO electrode.

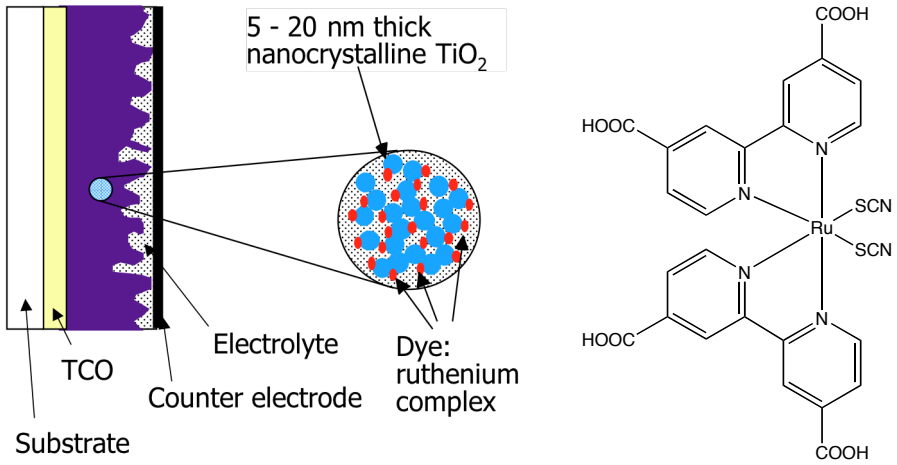

Figure 8.8. The dye-sensitized solar cell. After absorption of light by the ruthenium dye, a photogenerated electron in the dye is transferred to the conduction band of the TiO_2 nanoparticles. The dye is then reduced by a redox electrolyte, I^-/I_3^-, which in turn, is reduced at the metal counter electrode. As a result, a positive charge is transported from the dye to the metal electrode via the electrolyte. The electron in the nanocrystalline TiO_2 is transported to the TCO electrode.

The nanoporous TiO_2 ensures a dramatic enlargement of the contact area between the dye and semiconductor, compared to a flat interface. High quantum efficiencies for charge separation are achieved, because the dye molecules are adsorbed directly on the n-type semiconductor. The positive charges are transported efficiently by the liquid electrolyte and,

as a consequence the thickness of the photovoltaic device can be extended to the μm range, resulting in optically dense cells. From a technology point of view, however, the liquid electrolyte represents a drawback. Hence, much research has focused on replacing the liquid electrolyte by a solid hole transporting material. The most promising replacement is a solid, wide-band gap hole transporting material resulting in power conversion efficiencies of 3%.

Another new concept for a solid-state Grätzel cell consists of a polymer or organic semiconductor that combines the functions of light-absorption and charge (hole) transport in a single material and, therefore, is able to replace both the dye and the hole transporting material. The photoinduced charge separation at the interface of an organic and inorganic semiconductor has been studied in relation to photovoltaic devices. When an organic or polymeric semiconductor is excited across the optical band gap, the excitation energies and valence band offsets of this molecular semiconductor may allow electron transfer to the conduction band of an inorganic semiconductor, similar to the ruthenium dye. The dimensions of the nanopores in TiO_2 are even more important here, because excitations are no longer created at the interface only, but throughout the whole organic material. Because essentially all excitons must be able to reach the interface with the TiO_2 for efficient charge separation and energy conversion, the distance between the site of excitation and the interface must be within the exciton diffusion length. As discussed previously, in most organic materials, the exciton diffusion length is limited to 5-10 nm by the fast intrinsic decay processes of the photoexcited molecules. Creating nanoporous TiO_2 of such dimensions, and filling it completely with an organic semiconductor, is currently one of the challenges in this area.

8.5.2 Double layer cells

The first attempts to create all-organic solar cells were made by sandwiching a single layer of an organic material between two dissimilar electrodes. In these cells, the photovoltaic properties strongly depend on the nature of the electrodes. Heavily doped conjugated materials resulted in low power conversion efficiencies up to 0.3%.

In 1986, a major breakthrough was realized by Tang, who introduced a double-layer structure of a p- and n-type organic semiconductors (see Figure 8.4). A 70 nm thick two-layer device was made using copper phthalocyanine as the electron donor, and a perylene tetracarboxylic derivative as the electron acceptor (Figure 8.9). The photoactive material was placed between two dissimilar electrodes, indium tin oxide (ITO) for collection of the positive charges and silver (Ag) to collect the negative charges. A power conversion efficiency of about 1% was achieved under simulated AM2 illumination (691 W/m^2).

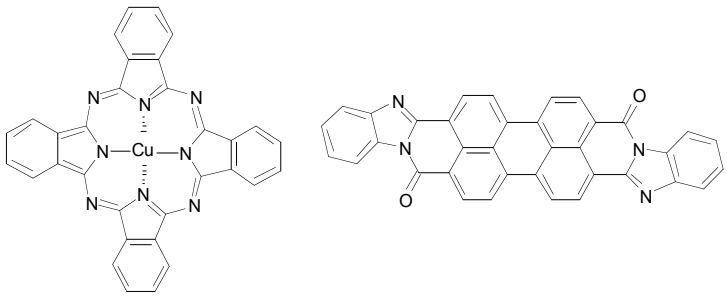

CuPc PTC

Figure 8.9. Molecular structures of copper phthalocyanine (CuPc) and a perylene diimide derivative.

In the double-layer configuration the photogenerated excitons in the photoactive material have to reach the p-n interface (Figure 8.4, centre) where charge transfer can occur, before the excitation energy of the exciton is lost via intrinsic radiative and non-radiative decay processes to the ground state. Because the exciton diffusion length of the organic material is in general limited to 5-10 nm, only absorption of light within a very thin region around the interface contributes to the photovoltaic effect. This limits the performance of double-layer devices, because such thin layers cannot absorb all the incident light. A strategy to improve the efficiency of the double-layer cell is related to structural organization of the organic material to extend the exciton diffusion length and, therefore, create a thicker photoactive interfacial area.

8.5.3 Bulk heterojunction cells

In combining electron donating and electron accepting materials in the active layer of a solar cell, care must be taken that excitons created in either material can diffuse to the interface and undergo charge separation. Due to their short lifetime and low mobility, the diffusion length of excitons in organic semiconductors is limited to about ~10 nm only. This imposes an important condition to efficient charge generation. Anywhere in the active layer,

the distance to the interface should be on the order of the exciton diffusion length. Despite their high absorption coefficients, exceeding 10^5 cm^{-1}, a 20 nm double layer of donor and acceptor materials would not be optical dense, allowing most photons to pass freely. The solution to this dilemma is elegantly simple. By mixing the *p* and *n*-type materials, junctions throughout the bulk of the material are created that ensure each photogenerated exciton leads to charge transfer, irrespective of the thickness of the layer.

Mixtures, or in other word blends, based on substituted fullerenes (with acronym PCBM) and DMOM-PPV (See Figure 8.10) were among the first materials to utilize this bulk-heterojunction principle. Nevertheless, this attractive solution poses a new challenge. Photogenerated charges must be able to migrate to the collecting electrodes through this composite material. Because holes are transported by the *p*-type semiconductor and electrons by the *n*-type material, these materials should be preferably mixed into a bicontinuous, interpenetrating network. In Figure 8.10 a bulk heterojunction solar cell is schematically depicted. The bulk heterojunction is presently the most widely used photoactive layer for realisation of organic solar cells. The name bulk-heterojunction solar cell has been chosen, because the interface between two different components (heterojunction) is all over the bulk, in contrast to the classical (bi-layer) junction. Control of morphology is not only required for a large charge-generating interface and suppression of exciton loss, but also to ensure percolation pathways for both electron and hole transport to the collecting electrodes.

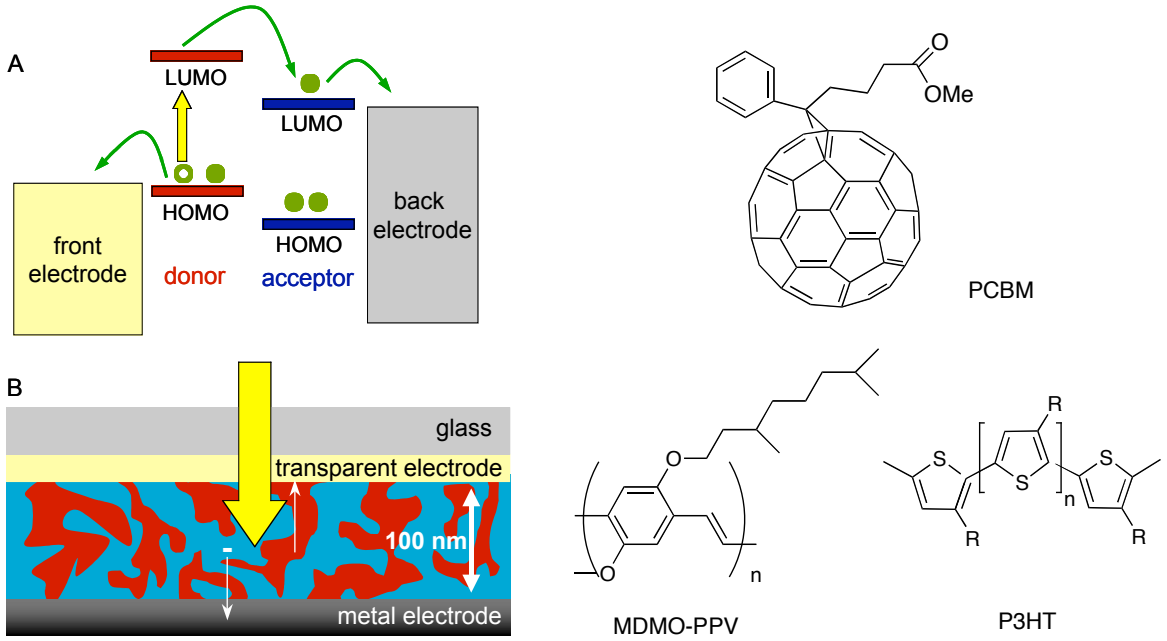

Figure 8.10. (left) The bulk-heterojunction concept. After absorption of light by the polymer, fast charge transfer occurs due to the nanoscopic mixing of the donor and acceptor materials. Subsequently, the photogenerated charges are transported and collected at the electrodes. (right) Donor and acceptor materials used in polymer-fullerene bulk-heterojunction solar cells. Acceptors: PCBM: 3´-phenyl-3´H-cyclopropa[1,9][5,6]fullerene-C_{60}-I_h-3´-butanoic acid methyl ester. Donors: MDMO-PPV = poly[2-methoxy-5-(3´,7´-dimethyloctyloxy)-p-phenylene vinylene]; P3HT= poly(3-hexylthiophene);

A breakthrough to truly appealing power conversion efficiencies exceeding 2.5% under simulated AM1.5 illumination was realized for bulk-heterojunction solar cells based on MDMO-PPV as a donor and PCBM as an acceptor. In PCBM, the fullerene cage carries a

substituent that prevents extensive crystallization upon mixing with the conjugated polymer and enhances the miscibility.

The electrical current densities are mainly limited by incomplete utilization of the incident light due to a poor match of the absorption spectrum of the active layer with the solar spectrum, and low charge carrier mobilities of the organic or polymer semiconductors. In this respect, the use of P3HT (Figure 8.10), which is known to have a high charge-carrier mobility and reduced bandgap compared to MDMO-PPV, has been considered for use in solar cells in combination with PCBM. P3HT/PCBM blends indeed exhibit an increased performance compared to MDMO-PPV. These higher efficiencies were obtained through the use of post-production treatment. After spin coating of the active layer and deposition of the aluminium top electrode, treating P3HT/PCBM solar cells by applying a voltage higher than the open circuit voltage and a temperature higher than the glass transition temperature of approximately 120 ºC led to an improved overall efficiency. This post-production treatment enhances the crystallinity of the P3HT and improves the charge carrier mobility. Photovoltaic devices of P3HT/PCBM have reached power conversion efficiencies of close to 5%.

8.6. Future developments regarding lifetimes and efficiencies

Of course any practical application of bulk-heterojunction polymer-fullerene solar cells requires that the cells are stable during the operation. Similar to the polymer light-emitting diodes, the present-day organic, polymer-based solar cells must be protected from ambient air to prevent degradation of the active layer and electrode materials by the effects of water and oxygen. Even with proper protection there are several degradation processes that need to be eliminated to ensure stability. Apart from device integrity, the materials must be photochemically stable and the nanoscale uniformity of donor-acceptor blend in the active layer should be preserved.

New combinations of materials that are being developed in various laboratories focus on improving the three parameters that determine the energy conversion efficiency of a solar cell, *i.e.* the open-circuit voltage (V_{oc}), the short-circuit current (J_{sc}), and the fill factor (FF) that represents the curvature of the current density-voltage characteristic. For ohmic contacts the open-circuit voltage of bulk-heterojunction polymer photovoltaic cells is governed by the energy levels of the highest occupied molecular orbital (HOMO) and the lowest unoccupied molecular orbital (LUMO) of donor and acceptor, respectively. In most polymer/fullerene solar cells, the positioning of these band levels of donor and acceptor is such that up to 0.4 to 0.8 eV is lost in the electron-transfer reaction. By more careful positioning of these levels, it is possible to raise the open-circuit voltage well above 1 V. The trade-off of increasing the donor-HOMO to acceptor-LUMO energy is that eventually a situation will be reached in which the photoinduced electron transfer is held back by a loss of energy gain.

One of the crucial parameters for increasing the photocurrent is the absorption of more photons. This may be achieved by increasing the layer thickness and by shifting the absorption spectrum of the active layer to longer wavelengths. Although the first improvement may seem trivial at first sight, an increase of the layer thickness is presently limited by the charge carrier mobility and lifetime. When the mobility is too low or the layer too thick, the transit time of photogenerated charges in the device becomes longer than the lifetime, resulting in charge recombination. The use of polymers such as P3HT that are known

to have high charge carrier mobilities allows an increase in film thickness from the usual ~100 nm to well above 500 nm, without a loss of current.

The absorption of the active layer in state-of-the-art devices currently spans the wavelength range from the UV up to about ~ 650 nm. In this wavelength range the monochromatic external quantum efficiency can be as high as 70% under short-circuit conditions, implying that the vast majority of absorbed photons contribute to the current. The intensity of the solar spectrum, however, maximizes at ~700 nm and extends into the near infrared. Hence, a gain in efficiency can be expected when using low-band gap polymers. The preparation of low-band gap, high mobility and soluble low-band gap polymers is not trivial and requires judicious design in order to maintain the open-circuit voltage or efficiency of charge separation. Because the open-circuit voltage of bulk-heterojunction solar cells is governed by the HOMO of the donor and the LUMO levels of the acceptor, the most promising strategy seems to lower the band gap by adjusting the other two levels, *i.e.* decrease the LUMO of the donor, or increase the HOMO of the acceptor, or both.

Literature used:

1. Halls, J.J. and R.H. Friend, *Organic Photovoltaic devices*, in *Clean electricity from photovoltaics*, M.D. Archer and R. Hill, Editors. 2001, Imperial College Press: London.
2. Simon, J. and J.J. Andre, *Molecular semiconductors*. 1985, Berlin-Heidelberg: Springer-Verlag. 142.
3. Hoppe, H. and N.S. Sariciftci, *Organic solar cells: An overview.* Journal Of Materials Research, 2004. **19**(7): p. 1924-1945.
4. Gregg, B.A., *Excitonic solar cells.* Journal of Physical Chemistry B, 2003. **107**(20): p. 4688-4698.
5. Gregg, B.A., *The photoconversion mechanism of excitonic solar cells.* Mrs Bulletin, 2005. **30**(1): p. 20-22.

Appendix A

PHYSICAL CONSTANTS

q	electronic charge	1.602×10^{-19} coulomb
m_0	electronic rest mass	9.108×10^{-31} kg
c	velocity of light in vacuum	2.998×10^{8} m/s
ε_0	permittivity of free space	8.854×10^{-12} farad/m
h	Planck's constant	6.625×10^{-34} joule × s
k	Boltzmann's constant	1.380×10^{-23} joule/K
kT/q	thermal voltage	0.02586 V (at 300 K)
λ_0	wavelength in vacuum associated with photon of 1 eV energy	1.239×10^{-6} m

SELECTED PROPERTIE OF SILICON (at 300 K)

E_g	energy band gap	1.08 eV
N_C	effective density of states in conduction band	3.0×10^{25} m^{-3}
N_V	effective density of states in valence band	1.0×10^{25} m^{-3}
n_i	intrinsic concentration of carriers	1.5×10^{16} m^{-3}.
ε_r	relative permittivity	11.7
n	refractive index	3.5 (at 1.1×10^{-6} m wavelength)
μ_e	electron mobility	1350×10^{-4} m^2/Vs
μ_h	hole mobility	480×10^{-4} m^2/Vs
D_e	electron diffusion coefficient	$0.02586 \times \mu_e$
D_h	hole diffusion coefficient	$0.02586 \times \mu_h$

Appendix B

Chapter 2: SOLAR RADIATION

$$\nu = c/\lambda \tag{2.1}$$

$$h\nu = \frac{1}{q}\frac{hc}{\lambda} \tag{2.2}$$

$$\Phi(\lambda) = P(\lambda)\frac{\lambda}{hc} \tag{2.3}$$

$$Air\ mass = (\cos\theta)^{-1} \tag{2.4}$$

Chapter 3: SEMICONDUCTOR MATERIALS FOR SOLAR CELLS

$$E_G = E_C - E_V \tag{3.1}$$

$$g_C(E) = \left(\frac{4\sqrt{2}\,\pi m_n^*}{h^3}\right)^{3/2}(E - E_C)^{1/2} \tag{3.2a}$$

$$g_V(E) = \left(\frac{4\sqrt{2}\,\pi m_p^*}{h^3}\right)^{3/2}(E - E_V)^{1/2} \tag{3.2b}$$

$$f(E) = \frac{1}{1+\exp\left[(E-E_F)/kT\right]} \tag{3.3}$$

$$n = \int_{E_C}^{E_{top}} g_C(E) f(E) dE \tag{3.4a}$$

$$p = \int_{E_{bottom}}^{E_V} g_V(E)\left[1 - f(E)\right] dE \tag{3.4b}$$

$$n = N_C \exp\left[(E_F - E_C)/kT\right] \qquad \text{for } E_C - E_F \geq 3kT \tag{3.5a}$$

$$p = N_V \exp\left[(E_V - E_F)/kT\right] \qquad \text{for } E_F - E_V \geq 3kT \tag{3.5b}$$

$$np = n_i^{\,2} = N_C N_V \exp\left[(E_V - E_C)/kT\right] = N_C N_V \exp\left[-E_g/kT\right], \tag{3.6}$$

$$n_i = N_C \exp\left[(E_i - E_C)/kT\right] = N_V \exp\left[(E_V - E_i)/kT\right] \tag{3.7}$$

$$E_i = \frac{E_C + E_V}{2} + \frac{kT}{2}\ln\left(\frac{N_V}{N_C}\right) = E_C - \frac{E_g}{2} + \frac{kT}{2}\ln\left(\frac{N_V}{N_C}\right) \tag{3.8}$$

$$\rho = q\left(p + N_D^+ - n - N_A^-\right) \tag{3.9}$$

$$p + N_D^+ - n - N_A^- = 0 \tag{3.10}$$

$$p + N_D - n - N_A = 0 \tag{3.11}$$

$$p + N_D - n = 0\,. \tag{3.12}$$

$$N_D \approx N_D^+ \approx n \tag{3.13}$$

$$p = \frac{n_i^2}{n} = \frac{n_i^2}{N_D} << n \tag{3.14}$$

$$p - n - N_A = 0\,. \tag{3.15}$$

$$N_A \approx N_A^- \approx p \tag{3.16}$$

$$n = \frac{n_i^2}{p} = \frac{n_i^2}{N_A} << p \tag{3.17}$$

$$E_C - E_F = kT \ln\left(N_C / N_D\right) \qquad \text{for } n\text{-type} \tag{3.18a}$$

$$E_F - E_V = kT \ln\left(N_V / N_A\right) \qquad \text{for } p\text{-type} \tag{3.18b}$$

$$\mathbf{v}_{dn} = -\mu_n \boldsymbol{\xi} \tag{3.19a}$$

$$\mathbf{v}_{dp} = \mu_p \boldsymbol{\xi} \tag{3.19b}$$

$$\mathbf{J}_{N|drift} = -q\, n\, \mathbf{v}_{dn} = q\, n\, \mu_n \boldsymbol{\xi} \tag{3.20a}$$

$$\mathbf{J}_{P|drift} = q\, p\, \mathbf{v}_{dp} = q\, p\, \mu_p \boldsymbol{\xi} \tag{3.20b}$$

$$\mathbf{J}_{drift} = q\,(p\,\mu_p + n\,\mu_n)\boldsymbol{\xi} \tag{3.21}$$

$$\mathbf{J}_{N|diff} = q\, D_N \nabla n \tag{3.22a}$$

$$\mathbf{J}_{P|diff} = -q\, D_P \nabla p \tag{3.22b}$$

$$\mathbf{J}_{diff} = q\left(D_N \nabla n - D_P \nabla p\right) \tag{3.23}$$

$$\mathbf{J} = \mathbf{J}_{drift} + \mathbf{J}_{diff} = q\,(p\,\mu_p + n\,\mu_n)\boldsymbol{\xi} + q\left(D_N \nabla n - D_P \nabla p\right) \tag{3.24}$$

$$\frac{D_N}{\mu_n} = \frac{kT}{q} \tag{3.25a}$$

$$\frac{D_P}{\mu_p} = \frac{kT}{q} \tag{3.25b}$$

$$\left.\frac{\partial n}{\partial t}\right|_{\text{light}} = \left.\frac{\partial p}{\partial t}\right|_{\text{light}} = G_L \tag{3.26}$$

$\Delta n << p_0$, $\quad p \cong p_0$ in a p-type material

$\Delta p << n_0$, $\quad n \cong n_0$ in an n-type material

$$\left.\frac{\partial n}{\partial t}\right|_{\substack{\text{thermal}\\ \text{R-G}}} = -c_n\, N_T\, \Delta n \qquad \text{for electrons in a } p\text{-type material} \tag{3.27a}$$

$$\left.\frac{\partial p}{\partial t}\right|_{\substack{\text{thermal}\\ \text{R-G}}} = -c_p\, N_T\, \Delta p \qquad \text{for holes in an } n\text{-type material} \tag{3.27b}$$

$$\tau_n = \frac{1}{c_n N_T} \tag{3.28a}$$

$$\tau_p = \frac{1}{c_p N_T} \tag{3.28b}$$

$$\left.\frac{\partial n}{\partial t}\right|_{\substack{\text{thermal}\\ \text{R-G}}} = -\frac{\Delta n}{\tau_n} \qquad \text{for electrons in a } p\text{-type material} \tag{3.29a}$$

$$\left.\frac{dp}{dt}\right|_{\substack{\text{thermal}\\ \text{R-G}}} = -\frac{\Delta p}{\tau_p} \qquad \text{for holes in an } n\text{-type material} \tag{3.29b}$$

$$L_N = \sqrt{D_N \tau_n} \qquad \text{for electrons in a } p\text{-type material} \tag{3.30a}$$

$$L_P = \sqrt{D_P \tau_p} \qquad \text{for holes in an } n\text{-type material} \tag{3.30b}$$

$L_N = \sqrt{D_N \tau_n}$ (for electrons in a *p*-type material)

$L_P = \sqrt{D_P \tau_p}$ (for holes in an *n*-type material)

$$E_{ph} = hc/\lambda \tag{3.31}$$

$$k = \frac{\alpha \lambda}{4\pi} \tag{3.32}$$

$$h\nu = \frac{h}{q}\frac{c}{\lambda} \tag{3.33}$$

$$\tilde{r} = \frac{\tilde{n}_0 - \tilde{n}_1}{\tilde{n}_0 + \tilde{n}_1} \tag{3.34}$$

$$\tilde{t} = \frac{2\tilde{n}_0}{\tilde{n}_0 + \tilde{n}_1} \tag{3.35}$$

$$R = |\tilde{r}|^2 = \left|\frac{\tilde{n}_0 - \tilde{n}_1}{\tilde{n}_0 + \tilde{n}_1}\right|^2 \tag{3.36}$$

$$T = \left|\frac{\tilde{n}_1}{\tilde{n}_0}\right| \; |\tilde{t}|^2 = \frac{4\,|\tilde{n}_0\,\tilde{n}_1|}{|\tilde{n}_0 + \tilde{n}_1|^2} \tag{3.37}$$

$$\Phi(x,\lambda) = \Phi^0(\lambda)\exp(-\alpha(\lambda)x), \tag{3.38}$$

$$\Phi^0(\lambda) = P(\lambda)\frac{\lambda}{hc} \tag{3.39}$$

$$g_{sp}(x,\lambda) = \eta_g \Phi^0(\lambda)\,\alpha(\lambda)\,e^{-\alpha(\lambda)x} \tag{3.40}$$

$$G_L(x) = \int_{\lambda_1}^{\lambda_2} g_{sp}(x,\lambda)\,d\lambda \tag{3.41}$$

$$G_L(x) = \eta_g\, A(x) \tag{3.42}$$

$$A(x) = \int_{\lambda_1}^{\lambda_2} \Phi^0(\lambda)\,\alpha(\lambda)\,e^{-\alpha(\lambda)x}\,d\lambda \tag{3.43}$$

$$n = N_C \exp\left[\left(E_{FC} - E_C\right)/kT\right] \tag{3.44a}$$
$$p = N_V \exp\left[\left(E_V - E_{FP}\right)/kT\right] \tag{3.44b}$$

$$n\,p = N_C\,N_V \exp\left[\frac{E_V - E_C}{kT}\right]\exp\left[\frac{E_{FC} - E_{FP}}{kT}\right] = n_i^2 \exp\left[\frac{E_{FC} - E_{FP}}{kT}\right] \tag{3.45}$$

$$\mathbf{J_N} = n\,\mu_n \nabla E_{FC} \tag{3.46a}$$
$$\mathbf{J_P} = p\,\mu_p \nabla E_{FV} \tag{3.46b}$$

$$\frac{\partial n}{\partial t} = \left.\frac{\partial n}{\partial t}\right|_{\text{drift}} + \left.\frac{\partial n}{\partial t}\right|_{\text{diff}} + \left.\frac{\partial n}{\partial t}\right|_{\substack{\text{thermal}\\ \text{R-G}}} + \left.\frac{\partial n}{\partial t}\right|_{\substack{\text{other processes}\\ \text{(photogeneration)}}} \tag{3.47a}$$

$$\frac{\partial p}{\partial t} = \left.\frac{\partial p}{\partial t}\right|_{\text{drift}} + \left.\frac{\partial p}{\partial t}\right|_{\text{diff}} + \left.\frac{\partial p}{\partial t}\right|_{\substack{\text{thermal}\\ \text{R-G}}} + \left.\frac{\partial p}{\partial t}\right|_{\substack{\text{other processes}\\ \text{(photogeneration)}}} \tag{3.47b}$$

$$\left.\frac{\partial n}{\partial t}\right|_{\substack{\text{thermal}\\ \text{R-G}}} = -R_N; \qquad \left.\frac{dp}{dt}\right|_{\substack{\text{thermal}\\ \text{R-G}}} = -R_P \tag{3.48a,b}$$

$$\left.\frac{\partial n}{\partial t}\right|_{\text{other processes}} = G_N; \qquad \left.\frac{\partial p}{\partial t}\right|_{\text{other processes}} = G_P \tag{3.49a,b}$$

$$\left.\frac{\partial n}{\partial t}\right|_{\text{drift}} + \left.\frac{\partial n}{\partial t}\right|_{\text{diff}} = \frac{1}{q}\nabla \cdot \mathbf{J}_{\mathrm{N}} \tag{3.50a}$$

$$\left.\frac{\partial p}{\partial t}\right|_{\text{drift}} + \left.\frac{\partial p}{\partial t}\right|_{\text{diff}} = -\frac{1}{q}\nabla \cdot \mathbf{J}_{\mathrm{P}} \tag{3.50b}$$

$$\frac{\partial n}{\partial t} = \frac{1}{q}\nabla \cdot \mathbf{J_N} - R_N + G_N \tag{3.51a}$$

$$\frac{\partial p}{\partial t} = -\frac{1}{q}\nabla \cdot \mathbf{J_P} - R_P + G_P \tag{3.51b}$$

$$\mathbf{J}_{\mathrm{N}} = q\,n\,\mu_n\,\xi + q\,D_N \nabla n \tag{3.52a}$$

$$\mathbf{J}_{\mathrm{P}} = q\,p\,\mu_p\,\xi - q\,D_p \nabla p \tag{3.52b}$$

$$\nabla \cdot \xi = \frac{\rho}{\varepsilon_r \varepsilon_0} \tag{3.53}$$

Chapter 4: SEMICONDUCTOR MATERIALS FOR SOLAR CELLS

$$n = n_{n0} \approx N_D \tag{4.1a}$$
$$p = p_{n0} \approx n_i^2 / N_D\,. \tag{4.1b}$$
$$p = p_{p0} \approx N_A \tag{4.2a}$$
$$n = n_{p0} \approx n_i^2 / N_A\,. \tag{4.2b}$$

$$\rho(x) = q\,N_D \qquad \text{for } -l_n \le x \le 0 \tag{4.3a}$$
$$\rho(x) = -q\,N_A \qquad \text{for } 0 \le x \le l_p \tag{4.3b}$$

$$\frac{d^2\psi}{dx^2} = -\frac{d\,\xi}{dx} = -\frac{\rho}{\varepsilon_r \varepsilon_0}. \tag{4.4}$$

$$\xi = \frac{1}{\varepsilon_r \varepsilon_0}\int \rho\, dx \tag{4.5}$$

$$\xi(-l_n) = \xi(l_p) = 0, \tag{4.6}$$

$$\xi(x) = \frac{q}{\varepsilon_r \varepsilon_0} N_D (l_n + x) \qquad \text{for } -l_n \le x \le 0 \tag{4.7a}$$

$$\xi(x) = \frac{q}{\varepsilon_r \varepsilon_0} N_A (l_p - x) \qquad \text{for } 0 \le x \le l_p \tag{4.7b}$$

$$N_A\, l_p = N_D\, l_n \tag{4.8}$$

$$\psi = -\int \xi\, dx \tag{4.9}$$

$$\psi(l_p) = 0. \tag{4.10}$$

$$\psi(x) = -\frac{q}{2\varepsilon_r \varepsilon_0} N_D\, (x + l_n)^2 + \frac{q}{2\varepsilon_r \varepsilon_0}\left(N_D l_n^2 + N_A l_p^2\right) \qquad \text{for } -l_n \le x \le 0 \tag{4.11a}$$

$$\psi(x) = \frac{q}{2\varepsilon_r \varepsilon_0} N_A (x - l_p)^2 \qquad \text{for } 0 \le x \le l_p \tag{4.11b}$$

$$\psi_0 = \psi(-l_n) - \psi(-l_p) = \psi(-l_n) \tag{4.12}$$

$$\psi_0 = \frac{q}{2\varepsilon_r \varepsilon_0}\left(N_D l_n^2 + N_A l_p^2\right). \tag{4.13}$$

$$q\psi_0 = E_G - E_1 - E_2 \tag{4.14}$$

$$q\psi_0 = E_G - kT \ln\left(\frac{N_V}{N_A}\right) - kT \ln\left(\frac{N_C}{N_D}\right) = E_G - kT \ln\left(\frac{N_V\, N_C}{N_A\, N_D}\right) \tag{4.15}$$

$$\psi_0 = \frac{kT}{q} \ln\left(\frac{N_A\, N_D}{n_i^2}\right). \tag{4.16}$$

$$l_n = \sqrt{\frac{2\varepsilon_r \varepsilon_0}{q}\psi_0\, \frac{N_A}{N_D}\left(\frac{1}{N_A + N_D}\right)} \tag{4.17a}$$

$$l_p = \sqrt{\frac{2\varepsilon_r \varepsilon_0}{q}\psi_0\, \frac{N_D}{N_A}\left(\frac{1}{N_A + N_D}\right)} \tag{4.17b}$$

$$W = l_n + l_p = \sqrt{\frac{2\varepsilon_r \varepsilon_0}{q}\psi_0 \left(\frac{1}{N_A} + \frac{1}{N_D}\right)} \tag{4.18}$$

$$\xi_{\max} = \sqrt{\frac{2q}{\varepsilon_r \varepsilon_0}\psi_0 \left(\frac{N_A\, N_D}{N_A + N_D}\right)} \tag{4.19}$$

$$J = J_{rec} - J_{gen} = 0 \qquad \text{for } V_a = 0 \text{ V} \tag{4.20}$$

$$J_{rec}(V_a) = J_{rec}(V_a = 0) \exp\left(\frac{qV_a}{kT}\right) \tag{4.21}$$

$$J_{gen}(V_a) \approx J_{gen}(V_a = 0) \tag{4.22}$$

$$J(V_a) = J_{rec}(V_a) - J_{gen}(V_a) = J_0\left[\exp\left(\frac{qV_a}{kT}\right) - 1\right], \tag{4.23}$$

$$J_0 = J_{gen}(V_a = 0) \tag{4.24}$$

$$J_0 = q\, n_i^2\left(\frac{D_N}{L_N\, N_A} + \frac{D_P}{L_P\, N_D}\right). \tag{4.25}$$

$$J(V_a) = -J_0\,, \tag{4.26}$$

$$J(V_a) = J_{rec}(V_a) - J_{gen}(V_a) - J_{ph} = J_0\left[\exp\left(\frac{qV_a}{kT}\right) - 1\right] - J_{ph} \tag{4.27}$$

$$J_{ph} = q\, G(L_N + W + L_P), \tag{4.28}$$

$$V_{oc} = \frac{kT}{q}\ln\left(\frac{J_{ph}}{J_0} + 1\right) \tag{4.29}$$

$$FF = \frac{J_{mp}\, V_{mp}}{J_{sc}\, V_{oc}} \tag{4.30}$$

$$FF = \frac{v_{oc} - \ln(v_{oc} + 0.72)}{v_{oc} + 1} \qquad v_{oc} = V_{oc}/(kT/q) \tag{4.31}$$

$$\eta = \frac{P_{\max}}{P_{in}} = \frac{J_{mp}\, V_{mp}}{P_{in}} = \frac{J_{sc}\, V_{oc}\, FF}{P_{in}} \tag{4.32}$$

Chapter 5: SOLAR CELL CONVERSION-EFFICIENCY LIMITS

$$P_{in} = \int_0^\infty P(\lambda)\, d\lambda \tag{5.1}$$

$$P_{in} = \int_0^\infty \Phi(\lambda)\frac{hc}{\lambda}\, d\lambda \tag{5.2}$$

$$p_{abs} = \frac{\int_0^{\lambda_G} \Phi(\lambda)\frac{hc}{\lambda}\, d\lambda}{\int_0^\infty \Phi(\lambda)\frac{hc}{\lambda}\, d\lambda} \tag{5.3}$$

$$p_{use} = \frac{E_G \int_0^{\lambda_G} \Phi(\lambda)\, d\lambda}{\int_0^{\lambda_G} \Phi(\lambda)\frac{hc}{\lambda}\, d\lambda} \tag{5.4}$$

$$\eta = p_{abs}\, p_{use} = \frac{\int_0^{\lambda_G} \Phi(\lambda)\frac{hc}{\lambda}\, d\lambda}{\int_0^\infty \Phi(\lambda)\frac{hc}{\lambda}\, d\lambda}\,\frac{E_G \int_0^{\lambda_G} \Phi(\lambda)\, d\lambda}{\int_0^{\lambda_G} \Phi(\lambda)\frac{hc}{\lambda}\, d\lambda} \tag{5.5}$$

$$QE(\lambda) = (1 - R^*)\, QE_{op}(\lambda)\, \eta_g(\lambda)\, QE_{el}(\lambda), \tag{5.6}$$

$$J_{\max} = q \int_0^{\lambda_G} \Phi(\lambda)\, d\lambda \tag{5.7}$$

$$J_{sc} = J_{\max} \left(1 - R^*\right) QE_{opt}\, \eta_G\, QE_{el}\, \frac{A_f}{A_{tot}} \tag{5.8}$$

$$J_{sc} = q \left(1 - R^*\right) QE_{opt}\, \eta_G\, QE_{el}\, \frac{A_f}{A_{tot}} \int_0^{\lambda_G} \Phi(\lambda)\, d\lambda \tag{5.9}$$

$$\eta = \frac{q \int_0^{\lambda_G} \Phi^0(\lambda)\, d\lambda}{\int_0^{\infty} \Phi^0(\lambda) \frac{hc}{\lambda} d\lambda} \left(1 - R^*\right) QE_{opt}\, \eta_G\, QE_{el}\, \frac{A_f}{A_{tot}} V_{oc}\, FF \tag{5.10}$$

$$V_{oc} = \frac{qV_{oc}}{E_G} \frac{E_G}{q} \tag{5.11}$$

$$\eta = \frac{q \int_0^{\lambda_G} \Phi^0(\lambda)\, d\lambda}{\int_0^{\infty} \Phi^0(\lambda) \frac{hc}{\lambda} d\lambda} \left(1 - R^*\right) QE_{opt}\, \eta_G\, QE_{el}\, \frac{A_f}{A_{tot}} \frac{qV_{oc}}{E_G} \frac{E_G}{q} FF \tag{5.12}$$

$$\eta = \frac{\int_0^{\lambda_G} \Phi^0(\lambda) \frac{hc}{\lambda} d\lambda}{\int_0^{\infty} \Phi^0(\lambda) \frac{hc}{\lambda} d\lambda} \quad \frac{E_G \int_0^{\lambda_G} \Phi^0(\lambda) d\lambda}{\int_0^{\lambda_G} \Phi^0(\lambda) \frac{hc}{\lambda} d\lambda} \quad \left(1 - R^*\right) \quad QE_{opt}^*\, \eta_G^*\, QE_{el}^*\, \frac{A_f}{A_{tot}} \frac{qV_{oc}}{E_G}\, FF \tag{5.13}$$

$$J = J_0 \left[\exp\left(\frac{q\left(V - AJR_s\right)}{kT} \right) - 1 \right] + \frac{V - AJR_s}{R_p} - J_{ph} \tag{5.14}$$

$$J = J_{01} \left[\exp\left(\frac{q\left(V - AJR_s\right)}{n_1 kT} \right) - 1 \right] + J_{02} \left[\exp\left(\frac{q\left(V - AJR_s\right)}{n_2 kT} \right) - 1 \right] + \frac{V - AJR_s}{R_p} - J_{ph} \tag{5.15}$$